A Combined Density Functional Theory and Monte Carlo Study of Manganites for Magnetic Refrigeration

Romi Kaur Korotana

Department of Chemistry

Imperial College London

A thesis submitted for the degree of

Doctor of Philosophy

Nov 2014

Declaration of Originality

I hereby declare that this thesis is a presentation of my original research work and has not been submitted previously for a degree qualification or any other academic qualification at this University or any other institution of higher education. Wherever contributions of others are involved, every effort is made to indicate this, with due reference to literature and acknowledgements of collaborative research and discussions. The research work presented in this thesis was conducted under the guidance of Professor Nicholas M. Harrison at Imperial College London, London.

Romi Kaur Korotana
July 2014

Declaration of Copyright

The copyright of this thesis rests with the author and is made available under a Creative Commons Attribution Non-Commercial No Derivatives licence. Researchers are free to copy, distribute or transmit the thesis on the condition that they attribute it, that they do not use it for commercial purposes and that they do not alter, transform or build upon it. For any reuse or redistribution, researchers must make clear to others the licence terms of this work.

Abstract

Perovskite oxides such as manganites are considered to be strong candidates for applications in magnetic refrigeration technology, due to their remarkable magnetocaloric properties, in addition to low processing costs. Manganites with the general formula $R_{1-x}A_xMnO_3$, particularly for A=Ca and $0.2 < x < 0.5$, undergo a field driven transition from a paramagnetic to ferromagnetic state, which is accompanied by changes in the lattice and electronic structure. Therefore, one may anticipate a large entropy change across the phase transition due to the first order nature. Despite many experimental efforts to enhance the isothermal entropy change in manganites, the maximum obtained value merely reaches a modest value in the field of a permanent magnet. The present work aims to achieve an understanding of the relevant structural, magnetic, and electronic energy contributions to the stability of the doped compound $La_{0.75}Ca_{0.25}MnO_3$. A combination of thermodynamics and first principles theory is applied to determine individual contributions to the total entropy change of the system by treating the electronic, lattice and magnetic components independently. For this purpose, hybrid-exchange density functional (B3LYP) calculations are performed for $LaMnO_3$, $CaMnO_3$ and $La_{0.75}Ca_{0.25}MnO_3$. The most stable phases for the end-point compounds are described correctly. Computed results for the doped compound predict an anti-Jahn-Teller polaron in the localised hole state, which is influenced by long-range cooperative Jahn-Teller distortions. The analysis of the energy scales related to the magnetocaloric effect suggests that the charge, orbital, spin and lattice degrees of freedom are strongly coupled, since they are of a similar magnitude. Through the analysis of individual entropy contributions, it is identified that the electronic and lattice entropy changes oppose the magnetic entropy change. Therefore, the electronic and vibrational terms have a deleterious effect on the total entropy change. The results highlighted in the present work may provide a useful framework for the interpretation of experimental observations as well as valuable guidelines for tuning the magnetocaloric properties of oxides, such as manganites.

Acknowledgements

This thesis would not be complete without acknowledging all the people who made it possible with their contributions. Foremost, I would like to express my deepest thanks to my supervisor, Professor Nicholas Harrison for giving me this opportunity and placing confidence in me. Nic's guidance, encouragement, and extensive knowledge were key motivations throughout my PhD; for both, my personal and academic development.

I wish to thank members of the Computational Material Sciences research group. Giuseppe has supported me at many critical stages of my research, he has been a valuable mentor throughout the PhD and I am grateful for all the help that was offered. Ruth and Ehsan, in particular, always made time and supported me through difficult periods. I'm also thankful to Leandro for his unwavering guidance during the initial stages of the PhD. A special acknowledgment goes to Monica and Leo, with whom I shared my office and an indefinate number of lunch and coffee breaks. Neither of them failed to make me smile. I would like to thank Frederico for being a wonderful desk buddy since the beginning of my PhD. In no particular order, I'd also like to acknowledge other colleagues: Ross, Jing, Bruno, Basma, Maryam, Hsiang-Han, Jassel, Joshua, Ariadna, Fatemeh, Vincent and David for memorable times.

I owe a great debt of gratitude to Lesley Cohen, Karl Sandeman, Zsolt Gercsi, João Amaral, Jeremy Turcaud and João Horta who have always inspired me with their deep insights for magnetocalorics. In particular, Zsolt and João Amaral always found the time to provide constructive feedback and guidance.

My heartfelt appreciation and endless gratitude goes to my friends outside of academia, particularly Mithila, Chahat and Neelam. A special mention for members of the IC women's cricket team: Taniya, Priya and Himani; who encouraged me to wind down at training sessions and provided invaluable support throughout my time at Imperial. I would also like to thank my ex-flatmates, Michael and Anita, with whom I shared some unforgettably fun times.

My sincere thanks go to my siblings for their unreserved love. I am deeply grateful

to Ravi for his financial support, and Komal for believing that this journey would come to an end. Finally, I express my utmost gratitude to my mother and father, they raised me, supported me, taught me, and loved me unconditionally; this thesis would not have been possible without their guidance.

The EPSRC is greatly acknowledged for funding the PhD. I would also like to mention that this work made use of the high performance computing facilities of Imperial College London and - via membership of the UKs HPC Materials Chemistry Consortium funded by EPSRC (EP/F067496) - of HECToR, the UKs national high-performance computing service, which is provided by UoE HPCx Ltd at the University of Edinburgh, Cray Inc and NAG Ltd, and funded by the Office of Science and Technology through EPSRC's High End Computing Programme.

List of Publications

- R. Korotana, G. Mallia, Z. Gercsi, and N. M. Harrison, A hybrid density functional study of Ca-doped $LaMnO_3$, *J. Appl. Phys.* **113** 17A910 2013.
- R. Korotana, G. Mallia, Z. Gercsi, L. Liborio and N. M. Harrison, A hybrid density functional study of structural, bonding, and electronic properties of the manganite series: $La_{1-x}Ca_xMnO_3$ (at x=0, 1/4 and 1), *Phys. Rev. B* **89** 205110 2014.
- R. Korotana, G. Mallia, and N. M. Harrison, A theoretical study of the electronic, vibrational and magnetic contributions to the entropy change in $La_{0.75}Ca_{0.25}MnO_3$ *In preparation*

List of Presentations

- Delft Days on Magnetocalorics, Delft, Holland, Oct 2013. (Poster)
- *Ab initio* Modelling in Solid State Chemistry Workshop, Imperial College London, UK, Sept 2013. (Poster)
- Chemistry Postgraduate Symposium, Imperial College London, UK, Jun 2013. (Talk)
- 12^{th} Joint MMM/Intermag Conference, Chicago, USA, Jan 2013. (Talk)
- 5^{th} IIR/IIF International Conference on Magnetic Refrigeration: THERMAG V, Grenoble, France, Sept 2012. (Poster)
- Chemistry Postgraduate Symposium, Imperial College London, UK, Jun 2012. (Poster)
- UK's HPC Materials Chemistry Consortium, University College London, UK, Mar 2012. (Talk)
- *Ab initio* Modelling in Solid State Chemistry Workshop, Imperial College London, UK, Sept 2011. (Poster)

For my parents

Contents

1 Introduction **19**

2 Magnetism and Phase Transitions **23**

2.1 Macroscopic Magnetic Order 23

2.2 Magnetic Interactions 25

2.3 Models of Phase Transitions 28

2.3.1 Landau Theory of Ferromagnetism 28

2.3.2 The Bean-Rodbell Model 29

2.3.3 Heisenberg Model 30

2.3.4 Ising Model 31

2.3.5 Hubbard Model 31

3 The Magnetocaloric Effect **33**

3.1 Thermodynamics 33

3.2 Measuring the Magnetocaloric Effect 35

3.3 Materials Research 37

3.4 Manganites as Magnetocaloric Materials 40

3.4.1 Structure and Properties 40

3.4.2 Doped Perovskite Manganites 42

3.5 Modelling of the Magnetocaloric Effect 44

4 Theoretical Concepts and Techniques **47**

4.1 Electronic Structure Methods 47

4.1.1 The Schrödinger Equation 48

4.1.2 Density Functional Theory (DFT) 50

4.1.3 Exchange-Correlation Functionals 52

4.2 The Basis Set Approximation 54

4.2.1 Atomic Orbital (Gaussian) Basis Sets 55
4.2.2 Plane-Wave (PW) Basis Sets 56
4.3 Periodic Model 56
4.4 The CRYSTAL Code 57
4.4.1 Geometry Optimisation 58
4.5 Monte Carlo Methods 59
4.5.1 Metropolis Algorithm 59
4.5.2 Outline of Monte Carlo Code 60

5 The End-point Stoichiometric Compounds: $LaMnO_3$ and $CaMnO_3$ 63
5.1 Orthorhombic $LaMnO_3$ 64
5.1.1 Experimental Structure 64
5.1.2 Optimized Structure 65
5.1.3 Electronic Structure 68
5.1.4 Magnetic Ordering and Phases 70
5.2 Orthorhombic $CaMnO_3$ 73
5.2.1 Optimized Structure 73
5.2.2 Electronic Structure 74
5.2.3 Magnetic Ordering and Phases 77
5.3 Summary 78

6 The Effects of Doping in $La_{1-x}Ca_xMnO_3$, where x=1/4 79
6.1 Optimized Structure of $La_{0.75}Ca_{0.25}MnO_3$ 81
6.2 Where does the hole go? 82
6.3 Formation of an Anti-JT Polaron 84
6.4 Magnetic Ordering 86
6.5 Energetics 87
6.5.1 Hopping Barrier 87
6.5.2 Doping Site Dependence 88
6.5.3 Disordered Ca Distribution 88
6.5.4 Magnetic Stability 89
6.5.5 Magnetic Coupling Constants 90
6.6 Summary 92

7 Entropy Contributions to the MCE 93
7.1 Electronic Entropy 95
7.2 Vibrational Entropy 97

7.3 Elastic Entropy 98
7.4 Magnetic Entropy 99
7.4.1 2D Ising Model 99
7.4.2 3D Ising Model 104
7.5 Summary 105

8 Final Conclusions **109**

A Basis Sets **113**
A.1 Oxygen 114
A.2 Manganese 115
A.3 Calcium 116
A.4 Lanthanum 117

B The Fluctuation Dissipation Theorem **119**

C The Exchange Coupling Constants **121**

D Electronic entropy of a 1D chain of hydrogen atoms **125**

E Validation of Monte Carlo Code: Limiting Case **127**

F Permissions **129**

Bibliography **145**

1

Introduction

The *Magnetocaloric Effect* (MCE) is defined as the change in temperature of a magnetic material, upon the application and removal of an external magnetic field under adiabatic conditions. The effect was first discovered, in iron, by Emil Warburg in 1881 [1]. In the past two decades, there has been a surge of interest in magnetocaloric materials which could potentially be used in cooling devices, such as heat pumps and magnetic refrigerators. Currently, the focus of this research field is on the possibility of employing the MCE for magnetic refrigeration close to room-temperature (RT).

Although the MCE was discovered in 1881, the first major advance occurred in the late 1920s, when Giauque [2] and Debye [3] independently proposed cooling via adiabatic demagnetisation. This process was then demonstrated by Giauque *et al.* in the late 1930s, where the paramagnetic salt $Gd_2(SO_4)_3.8H_2O$ was used to reach temperatures below 1K [4]. Giauque was later awarded the Nobel Prize in Chemistry for this work. In 1976, Brown constructed the first RT magnetic refrigeration system using gadolinium as a magnetic refrigerant [5]. However, in 1997, Pecharsky and Gschneidner discovered the so-called *Giant Magnetocaloric Effect* (GMCE) [6]. At the time, the discovery of materials exhibiting an MCE of up to three times higher than the most promising magnetic refrigerants gave a tremendous boost to magnetocalorics research.

Room temperature magnetic refrigeration provides numerous benefits and is therefore, a promising alternative to conventional refrigeration. Generally, refrigeration occurs due to the *Elastocaloric Effect* (ECE), which is defined as the compression and decompression of a fluid working in a thermodynamic cycle. Although, *Conventional Gas Compression* (CGC) refrigeration, which utilises the ECE, is a reliable and low-cost technology, possible improvements are limited. Moreover, it has detrimental effects on the environment due to the use of chlorofluorocarbons (CFCs) and hydrochloroflu-

orocarbons (HCFCs) as working fluids. In contrast, refrigerant gases are not required for magnetic cooling technology and therefore, concerns related to ozone depletion or the greenhouse effect are eliminated. Moreover, magnetic refrigeration technology employs a solid refrigerant (usually in the form of spheres or thin sheets) instead of gases. Hence, solid refrigerants are advantageous since they allow refrigerators to be built more compactly.

It has been predicted that around 15% of the worldwide energy usage is for some form of cooling, and in the USA, this figure could increase up to 50% during summer [7]. In recent years, due to increasing energy demands, scientists and engineers have begun to explore new technologies for cooling. The key objective in the research field of magnetic refrigeration is therefore, to reduce energy consumption using magnetocaloric materials, through improvements of the cooling efficiency. With current magnetocaloric materials, considerable efficiency is only possible with high magnetic field, which are inaccessible in devices based on permanent magnets. Therefore, further research for magnetocaloric materials exhibiting a large MCE in modest fields of permanent magnets is of significant interest for magnetic refrigeration technology. Furthermore, many of the materials investigated contain either very expensive or toxic elements, or are difficult to synthesise. The search for high performance magnetic refrigerants has resulted in a number of prototypes and generally, Gd or Gd based alloys have been employed as regenerator materials. However, since the focus of this work is specifically on material properties, rather than actual refrigeration devices, technical details and thorough reviews of prototypes can be found in references [8–10].

More recently, an economically viable class of materials, namely manganites, have attracted much attention due to their remarkable structural and electronic properties, which are strongly dependent on the doping concentration x as well as external variables, such as temperature, pressure, and electric or magnetic fields. Manganites are perovskites, which have the general formula $R_{1-x}A_xMnO_3$, where R is a trivalent rare earth metal and A is a divalent alkaline earth element. Such perovskites exhibit a rich variety of crytallographic, magnetic and electronic phases, which are attributed to a strong interplay between spin, charge, orbital and lattice degrees of freedom [11–13]. As a consequence of the effects of strong electron correlation, a complete microscopic understanding of the physics underlying the properties of manganites has not yet been achieved.

Since the discovery of the *Collosal Magnetoresistance* (CMR) in manganites [14–16], experimental studies on manganites doped with divalent alkaline earth elements, such as Ca, Ba and Sr, have been the subject of intense study. In particular, the

$La_{1-x}Ca_xMnO_3$ series of interest undergoes a phase transition from a low temperature (low T) ferromagnetic metallic (FM-M) to a high temperature (high T) paramagnetic insulating (PM-I) phase for $0.2 < x < 0.5$ [17]. The $x = 1/3$ composition has received considerable attention, because for this material the Curie temperature T_c is maximised and also because the observed MCE is the largest for the Ca-doped manganites [18,19]. The optimisation of the MCE in manganites has benefited from this experience and the vast amount of literature documenting their properties, but has not been guided by a predictive theory. The development of such a theory has been inhibited by the complexity of the full many body problem and therefore, theoretical studies have been confined to simplified models and approximations.

This thesis reports on the development of a first principles understanding of the MCE in the low hole density region of the $La_{1-x}Ca_xMnO_3$ phase diagram. The investigation focuses on the $La_{0.75}Ca_{0.25}MnO_3$ composition, which undergoes a phase transition from a ferromagnetic-metal (FM-M) at low T, to a paramagnetic-insulator (PM-I) at high T. In particular, a theoretical effort is made to quantify the electronic, lattice and magnetic entropy contributions to the MCE at this phase boundary. The resulting insights are intended as the basis for the optimisation of the MCE in manganites. Hybrid-exchange density functional theory (DFT) calculations are carried out to determine the effects of A-site doping on the electronic and magnetic properties. The first principles energetics are used to parameterise the Ising Hamiltonian, which allows finite temperature calculations of the FM-PM phase transition, where the Hamiltonian is solved within the Monte Carlo approach through the implementation of the Metropolis algorithm.

Materials physics underpins much of the work required to design better magnetocaloric materials with improved performance. Therefore, a fundamental understanding of the underlying physics associated with the magnetocaloric properties of materials is a necessary starting point, from a theoretical perspective. In particular, first principles calculations based on DFT currently play a significant role in determining the electronic structure of magnetocaloric materials. A theoretical description of the competing magnetic and structural phases can also be obtained. Subsequently, the exchange coupling energies and magnetic moments obtained from the DFT calculations can be used in conjunction with the Monte Carlo approach, to explore the phase diagram of magnetocaloric materials and determine their magnetocaloric properties at finite temperature. In comparison to other first principle electronic structure methods, the DFT approach can yield results of comparable accuracy at relatively low computational costs. Moreover, due to the combination of semi-local and non-local terms in

the exchange functional, and the inclusion of an effective self interaction correction, the hybrid B3LYP [20–22] approach provides an accurate description of optical band gaps, magnetic moments and coupling constants and M-I transitions [23–27] in strongly correlated systems such as manganites. The CRYSTAL code, used in this work, provides a general purpose, all-electron implementation of DFT approximations in periodic boundary conditions and is therefore, ideally suited to studying the electronic structure of the compositions of interest.

The general outline of this thesis is as follows. In Chapter 2, a brief theoretical background of magnetism and phase transitions is presented, this serves as an introduction to the physical effects that are important to develop an understanding of the MCE. Following this, in Chapter 3, thermodynamic aspects of the MCE are described and a review of magnetocaloric materials, particularly manganites, is given. Chapter 4 outlines the theoretical framework of the computations. Calculations on the end-point compounds, $LaMnO_3$ and $CaMnO_3$, are performed in Chapter 5, where the reliability of hybrid-DFT in describing manganite systems is investigated. In Chapter 6, the structural and electronic properties of $La_{1-x}Ca_xMnO_3$ at $x = 0.25$ are studied. The competing interactions are disentangled to determine their implications on the MCE for this composition. The electronic, vibrational and magnetic entropy contributions to the entropy change across the FM-M to PM-I phase transition in $La_{0.75}Ca_{0.25}MnO_3$ are quantified in Chapter 7. Finally, Chapter 8 summaries the main outcome of this work and its impact in the research fields of perovskite manganites and magnetocalorics.

A Note on Units

In atomic units, a.u.: $e = \hbar = m_e = 1$.

Energy: Hartee (a.u.) = 27.2138 eV.

Mulliken spin populations: 1 $\mu_B = e\hbar/2m_e = 1|e|$ in atomic units.

2

Magnetism and Phase Transitions

In this chapter, a brief overview of the theory of magnetism will be given. Since the MCE occurs at a magnetic phase transition, this chapter will provide the necessary background required to understand such phase transitions and the MCE in general. One interesting aspect of some magnetocaloric materials is the observation of a magnetic phase transition that coincides with a structural transition. Thus producing large discontinuities in the spin, charge and lattice related properties, which are characteristics of a first order phase transition. Consequently, a theoretical understanding of the order and nature of a transition is of paramount importance when considering the magnetocaloric properties of a material. Therefore, a brief description of the relevant theoretical models developed to study phase transitions is also provided. The macroscopic phenomenology of magnetism is discussed before introducing microscopic models of the underlying interactions, such as the Heisenberg, Ising and Hubbard model.

2.1 Macroscopic Magnetic Order

If all the magnetic moments of a material lie along a single unique direction in the absence of a magnetic field, the material is magnetised spontaneously. This form of magnetic ordering in a material is referred to as $ferromagnetism$. Magnetic materials can generally be characterised by their response to an external magnetic field, $\mathbf{H}$. A net magnetisation, $\mathbf{M}$ is induced in the solid, which is proportional to the applied field,

$$\mathbf{M} = \chi \mathbf{H} \tag{2.1}$$

where χ, the proportionality constant, is referred to as the *magnetic susceptibilty* and is defined as the change of the magnetisation with respect to the applied field $\frac{d\mathbf{M}}{d\mathbf{H}}$. The magnetic moments may also align antiparallel to each other, in which case there is no net magnetic moment and the ordering is $antiferromagnetic$. If the magnetic moments are not equal in magnitude but the alignment is antiparallel, the material is known as a $ferrimagnet$, which possesses a net magnetic moment. However, if the interactions between the unpaired electrons are weak relative to thermal fluctuations, the magnetic moments will be orientated in random directions. Thus, when the magnetic field is removed, the material is described as *paramagnetic*. The different types of magnetic ordering described here are depicted in Figure. 2.1.

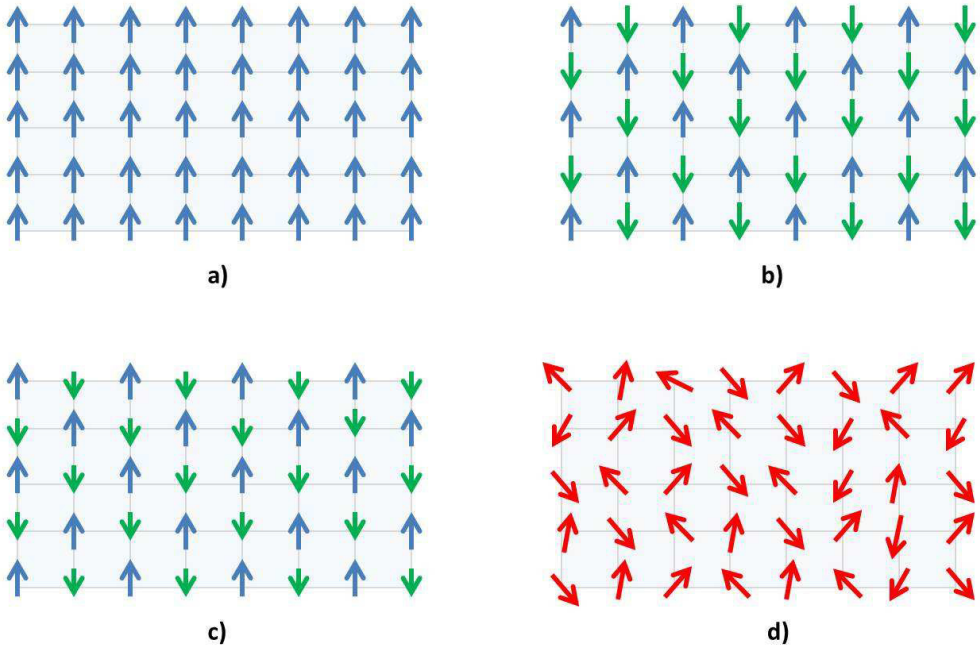


Figure 2.1: The orientation of the magnetic moments in a: a) ferromagnetic (FM), b) antiferromagnetic (AFM), c) ferrimagnetic and d) paramagnetic (PM) solid, in the absence of a magnetic field. The direction and length of the arrows indicate the direction and magnitude of the moments, respectively.

If we consider the typical response of a paramagnet to an external field, the $\mathbf{M}$ increases with $\mathbf{H}$. The spin moments align with the external field, resisting thermal disorder, until the saturation point where the magnetic moments are all aligned. The corresponding magnetisation is referred to as the *saturation magnetisation*, $\mathbf{M}_s$. Since there is strong magnetic coupling in the ferromagnetic state, the rate of change in $\mathbf{M}$

with **H** is higher than that of the paramagnetic state. However, **M** also converges to a saturation point. In the antiferromagnetic case, the magnetisation also increases linearly with **H** but at a decreased rate when compared to the ferromagnet. This is due to the antiferromagnetic coupling, which resists parallel alignment of the magnetic moments. The strength of the magnetic interactions is characterised by the Curie temperature, T_C for a ferromagnet and the Néel temperature, T_N for an antiferromagnet. T_C and T_N are critical temperatures (points), above which, their corresponding magnetic ordering disappears.

2.2 Magnetic Interactions

Long range magnetic ordering, as discussed in the previous section, is commonly referred to as *cooperative phenomena*, since it results from the interactions between magnetic dipole moments at the microscopic scale. Such interactions determine the relative alignment of the localised and/or itinerant moments. The *magnetic dipolar interaction* is expected to have a role in long range magnetic order. Two magnetic dipoles μ_1 and μ_2 separated by $\mathbf{r}$ have an energy equal to

$$E = \frac{\mu_0}{4\pi r^3}\left[\mu_1 \cdot \mu_2 - \frac{3}{r^2}(\mu_1 \cdot \mathbf{r})(\mu_2 \cdot \mathbf{r})\right] \tag{2.2}$$

which evidently depends on their separation and degree of mutual alignment [28]. If we consider two moments $\mu \approx 1\mu_B$, which are separated by $r \approx 1$Å then the order of magnitude of the energy is approximately $\mu^2/4\pi r^3 \sim 10^{-23}$J. This is around 1K in temperature and therefore, the magnetic dipolar interaction is too weak to account for ordering in most magnetic materials at higher temperatures. It can, however, be significant in materials that order at milli-Kelvin temperatures. *Exchange interactions*, on the other hand, are vital to the understanding of long range magnetic order. The exchange interaction is a type of magnetic interaction arising due to the balance between potential and kinetic energies. In this section we discuss different types of exchange interactions which occur, particularly in manganites.

Unpaired electrons localised on neighbouring atoms interact via the *direct exchange* mechanism. This particular exchange interaction proceeds directly without the need for an intermediary. It produces a short-range coupling and the strength is dependent on the overlap between the magnetic orbitals, which decays rapidly with increasing interatomic distance. If there is insufficient overlap between neigbouring magnetic orbitals *i.e.* for systems with strongly localised electrons, the magnetic atoms may not interact

via the direct exchange interaction. Therefore, a correct description of the exchange interaction needs to take into account the localised and band character of electrons. Direct exchange in orthogonal orbitals favours the parallel (positive exchange) alignment of spins and in the non-orthogonal scenario, either parallel and antiparallel (negative exchange) alignment of spins may be favoured depending on the interatomic distance.

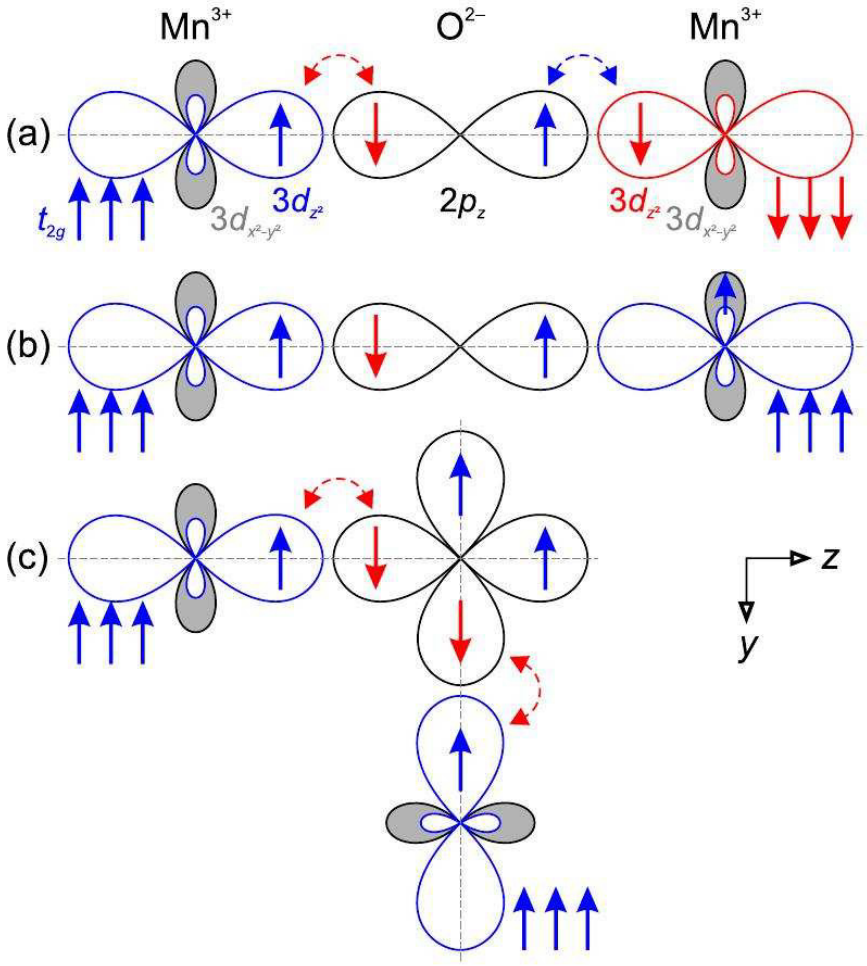


Figure 2.2: Schematic illustration of the Goodenough-Kanamori-Anderson (GKA) rules and the indirect superexchange interaction in $LaMnO_3$. The $3d_{x^2-y^2}$ orbital of Mn^{3+} is shaded in grey. The core spin S=3/2 of three t_{2g} orbitals of the Mn^{3+} is represented by the three arrows. The resulting interaction, which is dependent on the orbital occupation, could either be AFM (a) or FM (b) or (c). Taken from Ref. [29]. © IOP Publishing. Reproduced by permission of IOP Publishing. All rights reserved

There also exists an *indirect* exchange interaction, which may be responsible for the magnetic behaviour in a number of ionic solids, particularly transition metal oxides.

The *superexchange interaction* can be defined as an indirect exchange interaction between magnetic ions, mediated by a non-magnetic ion. The most prominent example for this particular exchange mechanism is of transition-metal (TM) ions, which are separated by O^{-2} in between. Here, the strength of the interaction is influenced through the overlap between the TM-3d and O-2p orbitals. Further, the sign of the interaction is determined via the degeneracy and occupancy of the TM-3d orbitals. A prediction of the spin alignment due to superexchange can be made through the implementation of a set of rules defined by Goodenough, Kanamori and Anderson (GKA) [30–32]. An example of the GKA rules is illustrated for $LaMnO_3$, along the z-direction, in Fig. 2.2. The magnetic exchange interaction between the $3d_{z^2}$ orbital of two Mn^{3+} ions via the $2p_z$ of the O^{2-} ion is depicted. Virtual hopping of the O-2p electrons to the overlapping Mn-3d orbitals reduces the overall energy of the system, depending on the direction of the core Mn spins, leading to virtual excited states.

In some oxides, particularly manganites, it is also possible to have a ferromagnetic exchange interaction which occurs due to a mixed valency (*i.e.* exist in more than one oxidation state) of the magnetic ions in the system. The ferromagnetic alignment of spins can be explained by Zener's model of *double exchange* [33, 34]. If we consider a mixed valence system consisting of Mn^{3+} and Mn^{4+} ions where the configurations are d^4 and d^3, respectively, the electron occupying the e_g orbital for Mn^{3+} can hop to a neighbouring site only if there is a vacancy of the same spin. Therefore, if the neighboring ion is Mn^{4+}, this is a possible scenario. The exchange interaction between the e_g and t_{2g} electrons keeps the spin moments aligned. It is, however, not possible for the e_g from the Mn^{3+} to hop onto a neighbouring ion in which the t_{2g} spins are antiparallel to that of the e_g electron. The hopping of the electron provides a kinetic energy saving, thus reducing the overall energy and becoming metallic.

Generally, superexchange occurs in insulators, while the $Ruderman-Kittel-Kasuya-Yosida$ (RKKY) exchange mechanism is dominant in metals; where the interaction between the magnetic ions is mediated by the conduction electrons. A localised spin moment polarises the conduction electrons and this polarisation, in turn, couples to a neighbouring localised spin moment a distance r away, fluctuating in sign (FM/AFM) on a length scale of $1/k_F$, where k_F is the Fermi wave vector. In contrast to the direct exchange interaction, this type of exchange mechanism is considered to be $long-range$. The RKKY interaction is not described in detail herein, since the work in this thesis is concerned primarily with oxide materials.

The exchange mechanisms described in this section are models that are able to account for the magnetic behaviour in many magnetic materials and define the electronic

properties, as well as the degree of localisation of the magnetic moments. Some of the exchange mechanisms can coexist in a system and therefore, the macroscopic behaviour can be attributed to more than one magnetic interaction.

2.3 Models of Phase Transitions

In statistical mechanics, a connection is made between the macroscopic phase of a system and its microscopic properties. A phase transition is associated with broken symmetry in a system and in order to understand some of the consequences of symmetry breaking and phenomena, such as the MCE, it is important to consider simplified *models* of magnetism. Such models are briefly discussed in this section.

2.3.1 Landau Theory of Ferromagnetism

A basic thermodynamic discussion of phase transitions can be presented on the basis of the Landau theory, which is also a mean-field model. In such models, it is assumed that a magnetic moment senses an *average* internal field, which is produced by neighbouring magnetic moments. The Landau theory, in particular, describes the free energy at the ferromagnetic to paramagnetic critical point and highlights the importance of symmetry when considering a phase transition. The macroscopic free energy expansion for a ferromagnet, with magnetisation $\mathbf{M}$ can be written as a power series in $\mathbf{M}$ [28]; where the polynomial only contains even powers to maintain global symmetry of the spin Hamiltonian. Subsequently, the free energy, $F(\mathbf{M})$ can be written as,

$$F(\mathbf{M}) = F_0 + a(T)\mathbf{M}^2 + b\mathbf{M}^4 \tag{2.3}$$

where F_0 and b are constants (it is assumed that b $>$ 0) and the coefficient a is dependent on temperature. If the free energy is minimised to find the ground state by looking for solutions of $\partial F/\partial \mathbf{M}$=0, we find

$$2\mathbf{M}[a_0(T - T_C) + 2b\mathbf{M}^2] = 0. \tag{2.4}$$

Since the left side of the equation is a product of two terms, either of them could be zero and therefore, $\mathbf{M}$=0 or,

$$\mathbf{M} = \pm \left[\frac{a_0(T_C - T)}{2b}\right]^{1/2} \tag{2.5}$$

where a_0 is a positive constant and this expression is valid when T $<$ T_C. Free

energy terms up to the sixth order of the magnetisation are required to describe a first order phase transition, where it follows that $\delta\mathbf{M}/\delta H$ can only be maximised if b $<$ 0 [35, 36]. However, it must be noted that the Landau theory and mean-field theories in general, fail to describe the critical region correctly.

2.3.2 The Bean-Rodbell Model

The FM-PM transition is a second-order phase transition, which as an initial approximation can be described by the rigid lattice, Ising (or Heisenberg) model (see sections 2.3.3 and 2.3.4). Since the lattice is fixed, it is implicitly assumed that the exchange interaction and lattice spacing are independent parameters. However, in physical systems, the lattice can distort at the phase transition and the associated entropy change may enhance or reduce the MCE. Despite the complexity of the magneto-elastic coupling between the magnetic and lattice degrees of freedom, first order phase transitions can be described in terms of the phenomenological macroscopic Bean-Rodbell model [37], which is an extension to the Weiss classical molecular mean-field model [1]. The intricacy of magneto-elastic coupling is simplified by focusing merely on the volume variation across the phase transition. This model was used by Blois and Rodbell in 1963, to describe the first order phase transition in MnAs [38].

The basic assumption of this model is that the Curie temperature T_C is strongly dependent upon the interatomic spacing. Thus, T_C depends on a volumetric lattice deformation and is given by:

$$T_C = T_o \left[1 + \beta \left(\frac{V - V_o}{V_o}\right)\right] \tag{2.6}$$

where T_o is the Curie temperature corresponding to an incompressible lattice, V_o is the initial volume *i.e.* the volume prior to the application of an external magnetic field and β is a coefficient, which corresponds to the dependence of the ordering temperature on the volume and could either be positive or negative. If the volume remains constant *i.e.* an increase in one lattice parameter is compensated by a decrease in the other; then T_C can be written in terms of lattice parameter changes.

The behaviour of a system is analysed on the basis of the Gibbs free energy, which consists of the following contributions:

$$G = G_{exchange} + G_{Zeeman} + G_{elastic} + G_{entropy} + G_{pressure} \tag{2.7}$$

[1] An effective internal molecular field is defined in the Weiss mean-field model, which is proportional to the magnetisation of a magnetic material.

where $G_{exchange}$, G_{Zeeman}, $G_{elastic}$, $G_{entropy}$, and $G_{pressure}$ correspond to the exchange interaction energy, Zeeman energy, elastic energy, entropy and pressure terms, respectively. The exchange interaction is expressed in terms of the mean-field approximation and the Gibbs free energy has the form [39]:

$$G = -\frac{3}{2}\left(\frac{J}{J+1}\right) N k_B \left(T_o\left[1+\beta\left(\frac{V-V_o}{V_o}\right)\right]\right)\sigma^2 - g\mu_B HJN\sigma + \frac{1}{2K}\omega^2 + P\omega - T(S_{mag}+S_{lat}) \tag{2.8}$$

where N is the number of magnetic ions per unit volume, k_B is the Boltzmann constant and σ is the normalized magnetization. In the Zeeman energy term, g is the Lande factor and **H** is the external magnetic field. In the elastic energy term K is the volume compressibility. The fourth term is a correction due to applied pressure, where ω is the volume change. The final term is a correction due to the magnetic and lattice entropies of the system.

2.3.3 Heisenberg Model

In this subsection and subsequent subsections, microscopic models are considered to understand phase transitions in solids. In the Heisenberg model, the magnetic moment at a magnetic site (ith atom or a group of atoms), μ_i has a spin angular momentum, S_i and is defined through the relation,

$$\mu_i = g\mu_B S_i \tag{2.9}$$

where g is the Landé factor and μ_B is the Bohr magneton. The value of S_i is determined by the electronic configuration of the magnetic site. The fundamental physics of a magnetic system is often attributed to the quantum mechanical interactions between spin angular momenta. However, the theoretical aspect of such interactions in a three dimensional solid is a non-trivial problem, which requires many approximations. In the *Heisenberg model*, the spin Hamiltonian has been approximated by considering only two-body nearest-neighbor interactions. This approximation relies on the assumption that the magnetic interactions decay rapidly with increasing distance between the spin moments. The Heisenberg Hamiltonian has the form:

$$\hat{H}^{Heisenberg} = -\frac{1}{2}\sum_{\langle i,j\rangle} J_{ij}\mathbf{S}_i\mathbf{S}_j \tag{2.10}$$

where J_{ij} is the magnetic coupling constant between the i^{th} and j^{th} magnetic sites and $\mathbf{S}$ is the spin state. The sign and magnitude of the J_{ij} constant define the nature (ferromagnetic for $J_{ij}>0$ and antiferromagnetic for $J_{ij}<0$) and strength of the interaction between the magnetic moments. Solving the Heisenberg model is a complex process and there is no analytical solution for three-dimensional periodic systems.

2.3.4 Ising Model

The Ising model is a lattice model, which was developed in the 1920s to study phase transitions in ferromagnetic materials, in particular. It is one of the simplest and best studied models in statistical mechanics and can be solved analytically for a few simplified cases, such as in one-dimension (with and without an external magnetic field) and in two-dimensions (without an external magnetic field). We consider a simple cubic lattice with periodic boundary conditions and propose that interactions occur only between nearest neighbouring spin states. The dimensionality of the moment is one and therefore, only the z component of the spin variable is considered. Consequently, the spin is only allowed to point along the $\pm z$ direction. The Ising Hamiltonian, H_{mag} is defined as:

$$\hat{H}^{Ising} = -\frac{1}{2}\sum_{\langle i,j\rangle} J_{ij}S_i{}^z S_j{}^z - \sum_i H_{ext}S_i{}^z \tag{2.11}$$

where H_{ext} is an external magnetic field, J_{ij} is the exchange parameter and S is the spin state, which can only take on the value -1 (spin *down*) or 1 (spin *up*). A spin degree of freedom is placed on each site of the lattice, where it is subject to simple interaction energies. Exact solutions for finite systems can be determined by summing over all possible spin configurations. However, since the number of configurations is 2^n, this approach becomes infeasible.

2.3.5 Hubbard Model

The *Hubbard Model* is a highly simplified model of electron correlation, which describes both metallic and localised behaviour, thus describing the transition between conducting and insulating systems. The model was initially introduced in the early 1960's and applied to understand the behaviour of strongly correlated transition metal oxides,

which were antiferromagnetic insulators. Metallic behaviour in solids is attributed to the kinetic energy of electrons, which leads to delocalisation. The kinetic energy is parameterised by the transfer integrals in the tight-binding model t (also referred to as the *hopping* integrals). However, the Coulomb energy, which is required to remove an electron from a site and add it to another site is parameterised by U, also known as the *Hubbard U*. If the Coulomb energy parameter, U, is large but not infinite, each lattice site will be singly occupied and the electron could visit a neighbouring site, provided the spins are antiparallel (in accordance with Pauli's exclusion principle). This leads to insulating behaviour and such systems are commonly referred to as *Mott insulators*. The Hubbard Hamiltonian consists of two components for a system with one orbital per site, and takes the form,

$$\hat{H}^{Hubbard} = -t \sum_{\langle i,j \rangle} \sum_{\sigma} (c^{\dagger}_{i\sigma} c_{j\sigma} + c^{\dagger}_{j\sigma} c_{i\sigma}) + U \sum_{i} \hat{n}_{i_\uparrow} \hat{n}_{i_\downarrow} \tag{2.12}$$

where $c^{\dagger}_{i\sigma}$ and $c_{i\sigma}$ are the creation and annihilation operators of an electron with spin σ=$\uparrow$,$\downarrow$ at lattice site i. The occupation number operator, $\hat{n}_{i\sigma}$ is defined as $\hat{n}_{i\sigma}$=$c^{\dagger}_{i\sigma} c_{i\sigma}$ and t is the transfer integral. The first term is the kinetic energy term, which defines the energy contribution arising from electrons hopping between nearest-neighbouring lattice sites. The second term represents the Coulomb repulsion between two electrons that occupy the same orbital.

A definition of the low-energy spectrum of a magnetic system is derived from the competing transfer integral t and on-site Coloumb repulsion U terms. Thus, the absolute zero behaviour of the Hubbard model is controlled by two parameters: the relative interaction strength, U/t, and the average electron density per electron site, n/L, where n is the total number of electrons, L is the number of lattice sites. When $U/t \to 0$, the Hubbard Hamiltonian corresponds to the tight-binding Hamiltonian derived from band theory. In the other limiting case, $U/t \to \infty$, the electrons minimise the Coulomb repulsive energy by occupying different lattice sites. In the large U/t regime (in the half-filled limit), the low energy states of the Hubbard model can be mapped onto an antiferromagnetic Heisenberg Hamiltonian (with an exchange constant, $J = 4t^2/U$).

3

The Magnetocaloric Effect

This chapter introduces the MCE, particularly the theory and thermodynamics associated with the effect. Initially, the basic thermodynamic concepts behind the MCE are outlined and the Gibbs free energy for a magnetic system is described. Following this, details of magnetic refrigeration are given. Various classes of materials suitable for magnetocaloric applications are then presented and the magnetocaloric properties of manganites are discussed comprehensively. The final section briefly introduces theoretical concepts associated with the MCE and also highlights studies in which the MCE has been considered from a theoretical perspective.

3.1 Thermodynamics

As described in the introduction, the MCE is effectively the heating or cooling of a magnetic material, in response to the application and removal of a magnetic field adiabatically. It is an intrinsic property of all magnetic materials. In order to quantify the MCE exhibited by a material, and understand the nature of a magnetic phase transition, one must consider the thermodynamic properties of a system which are determined by the free energy. In the presence of an external magnetic field H, the Gibbs free energy G, is given by:

$$G = U - TS + PV - MH \tag{3.1}$$

where U is the internal energy, T is the absolute temperature, H is the applied magnetic field and P is the pressure. The entropy S, volume V and, magnetization M are given by the first derivatives of the Gibbs free energy in Equations, 3.2, 3.3 and 3.4, respectively.

$$S(T,P,H) = -\left(\frac{\partial G}{\partial T}\right)_{P,H} \tag{3.2}$$

$$V(T,P,H) = \left(\frac{\partial G}{\partial P}\right)_{T,H} \tag{3.3}$$

$$M(T,P,H) = -\left(\frac{\partial G}{\partial H}\right)_{T,P} \tag{3.4}$$

In accordance with the second law of thermodynamics, the specific heat C of a system can be defined as the second derivative of the Gibbs free energy with respect to temperature,

$$C(T,H) = T\left(\frac{\partial S}{\partial T}\right)_{P} = -T\left(\frac{\partial^2 G}{\partial T^2}\right)_{P} \tag{3.5}$$

Phase transitions are generally classified as either $first\text{-}order$ or *second-order*. The general characteristic of a transition is an abrupt change in one or more physical properties. By definition, if the first derivatives of the Gibbs free energy are discontinuous at the phase transition, the transition is of first order. If, however, the first derivative is continuous and the second derivative is discontinuous, then the phase transition is of second order.

As seen in Equation. 3.2, the entropy S, of a magnetocaloric material is dependent upon the temperature T, magnetic field H and pressure P. When a sufficiently high external magnetic field is applied adiabatically to a material, the spin moments align, and the magnetic part of the entropy decreases due to the coupling of the magnetic field and the magnetic moments. In order to keep the total entropy (spin and lattice contributions) in an adiabatic process constant, the crystalline lattice part of the entropy increases and the material heats up. This heat is then transferred to the ambient atmosphere and the material returns to its initial temperature. Subsequently, when the magnetic field is removed adiabatically, the crystalline lattice entropy decreases and the material cools down. This adiabatic cycle of magnetic cooling is depicted in Figure. 3.1. The cycle is reversible, if we assume that thermal hysteresis loss is negligible.

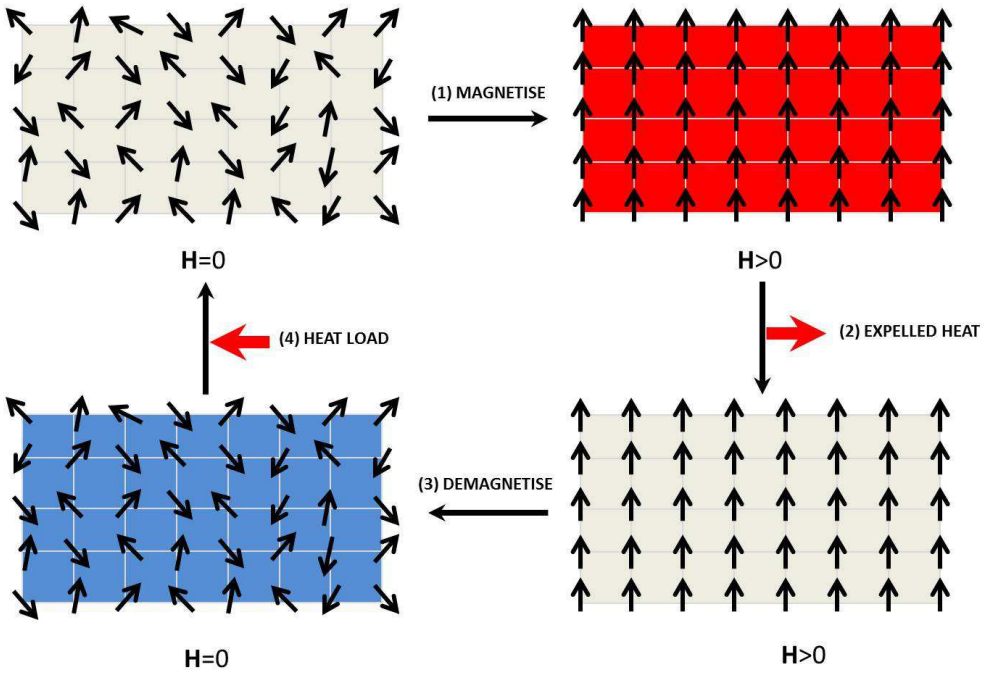


Figure 3.1: A magnetic material is converted reversibly between different magnetic states ((1)-(4)) due to the application and removal of an external magnetic field, and changes temperature as result.

3.2 Measuring the Magnetocaloric Effect

The MCE can be determined by the entropy change in an isothermal process via integration of the thermodynamic Maxwell relation (Equation 3.6) and the temperature change in an adiabatic process (Equation 3.7) [39], where $C(T, H)$ is the specific heat capacity of a material.

$$\Delta S_{iso}(T, \Delta H) = \int_{H_0}^{H_1} \left(\frac{\partial M(T, H)}{\partial T} \right)_H \mathrm{d}H \tag{3.6}$$

$$\Delta T_{ad}(T, \Delta H) = -\int_{H_0}^{H_1} \frac{T}{C(T, H)} \left(\frac{\partial M(T, H)}{\partial T} \right)_H \mathrm{d}H \tag{3.7}$$

Values of ΔS_{iso} and ΔT_{ad} are commonly used as a basis to compare the magnetocaloric properties of materials. These two quantitative characteristics are shown in Figure. 3.2 - a graphical representation of a magnetic refrigeration cycle. The total entropy S_{tot} of a magnetic material at constant pressure is dependent on both the applied

magnetic field (H) and temperature (T). Further, contributions to S_{tot} arise from the lattice, electronic and magnetic entropies, which is defined as

$$S_{tot} = S_{lat} + S_{elec} + S_{mag}. \tag{3.8}$$

at constant pressure. Experimentally, the MCE is usually determined indirectly, through magnetization and specific heat measurements. However, the adiabatic temperature change can be calculated directly from measurements of the sample temperature (T_0 and T_1) in magnetic fields H_0 and H_1, where the subscripts 0 and 1 denote the initial and final temperature/magnetic field, respectively. The correct evaluation of the MCE is, however, a controversial issue. It is worth noting that indirect methods of determining the MCE require extensive processing of numerical data which could result in significant experimental errors, yielding inaccurate results. Limitations of such numerical procedures have been studied extensively by Pecharsky and Gschneidner [40].

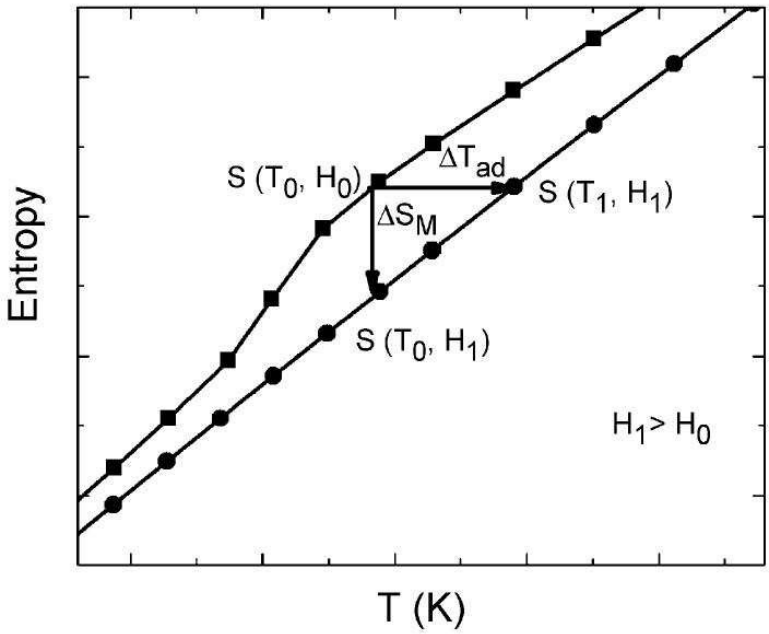


Figure 3.2: Total entropy versus temperature diagram for two values of the applied magnetic field, $H_1>0$. The horizontal and vertical arrows show the adiabatic temperature change (ΔT_{ad}) and the isothermal magnetic entropy change (ΔS_M), respectively. This figure is taken from ref. [41] with permission.

3.3 Materials Research

There are several promising classes of materials which exhibit a considerable MCE and have tunable transition temperatures. Current research aims to discover magnetic materials that display a large MCE at or near RT, are economically viable and operate in fields generated by permanent magnets. Subsequently, continual efforts are being made to search for magnetocaloric materials that exhibit a first order phase transition in a narrow temperature range, since this is expected to maximise the MCE [19,42–44]. However, there are large thermal and magnetic hystereses associated with first order behaviour. Such hystereses have a detrimental effect on the refrigerant capacity q, which is expressed as

$$q = \int_{T_{cold}}^{T_{hot}} \Delta S(T,H) dT \tag{3.9}$$

and is effectively a measure of how much heat can be transferred between a hot and cold sink in an ideal refrigeration cycle. It is therefore unclear whether materials exhibiting a first, or second order phase transition should be used for applications in magnetocalorics. Hence, the properties, which define the ideal magnetic refrigerant, may vary with the refrigeration system and the desired temperature interval. In terms of an explicit criteria for selecting magnetic refrigerants, there are some prerequisites such as a high saturation magnetisation (*i.e.* magnetic ions with large spin moments), which is proportional to the MCE. Further, a small specific heat and a large thermal conductivity are also desirable, since the temperature change and heat exchange rate are optimised [19]. Considering a significant range of materials display magnetocaloric properties, a discussion of all such materials would clearly be beyond the scope of this thesis. Therefore, the main classes of materials are briefly discussed in this section; the maximum entropy change ΔS_{MAX} exhibited by such magnetocaloric materials is shown in Fig. 3.3.

The laves phases are intermetallic compounds with stoichiometry AB_2, where A is rare-earth metal (including Sc and Y) and B is mainly a transition metal but could also be other elements such as Al, Ga and Ge [41,44]. Amongst the RCo_2-based compounds, $ErCo_2$, $HoCo_2$ and $DyCo_2$ exhibit first order magnetic transitions and a large MCE is observed [41]. In such materials an itinerant metamagnetic transition occurs upon the application of a magnetic field, which is described as a transition from a paramagnet to an ordered structure of itinerant electrons [45]. Although the first order magnetic phase transition laves phases exhibit a $\Delta S_{MAX} \approx 30 \mathrm{Jkg}^{-1}\mathrm{K}{-}1$ at a $\mathrm{T}_{peak} \approx 50\mathrm{K}$ for a $\Delta H =$

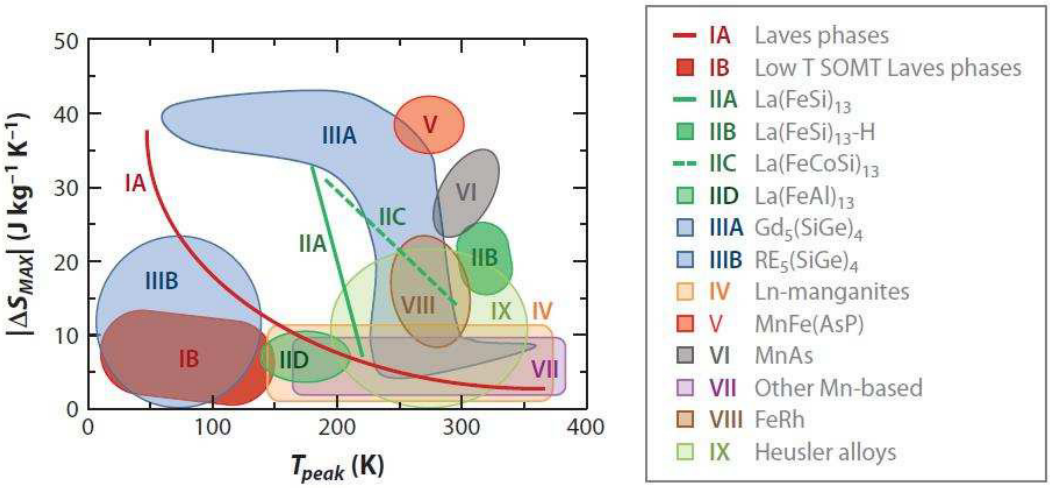


Figure 3.3: The maximum entropy change ΔS_{MAX} for $\Delta H = 5$T versus the peak temperature for different classes of magnetocaloric material. This figure has been taken from Reference [44] with permission.

5T, a general parabolic decrease is observed with an increasing transition temperature, as can be seen in Fig. 3.3. This is attributed to the second order character of phase transitions at higher temperatures [41]. Therefore, the laves phases are generally of interest for applications at low temperatures.

The rare-earth metal, Gd has a large magnetic moment and exhibits a considerable MCE near room temperature; it has therefore been the focus of research for magnetocaloric applications in recent years. Subsequently, Gd has been used in prototype room temperature regenerator designs [8, 46], and has been considered to be the most active magnetic refrigerant thus far. The ΔS_M, determined from magnetisation measurements, is -9.8JK^{-1}kg^{-1} for a magnetic field variation from 0T to 5T, and the ΔT_{ad} value is 11.6K near $T_c = 294$K [47]. Since rare-earth metals are acutely expensive, the usage of Gd as a solid refrigerant is commercially limited. For this reason, transition metal based alloys have an advantage since they are much cheaper than rare-earth metals.

Materials undergoing a magnetostructural phase transition with large values of ΔS_M are often referred to as *giant* magnetocaloric materials. Remarkably in the late 1990s, Pecharsky and Gschneidner coined the term, *Giant Magnetocaloric Effect* (the first order magnetic transition laves phases discussed previously also exhibit this effect) after it was discovered that the MCE in the alloy, $Gd_5Si_2Ge_2$ was around 50% larger than that determined for Gd [6]. Despite the fact that the transition temperature

(of 276K) is much lower than that of Gd, $Gd_5Si_2Ge_2$ is considered to be a potential candidate to improve the efficiency of large scale magnetocaloric refrigeration since the following MCE parameters have been determined: ΔS_M = -18Jkg^{-1}K^{-1} and ΔT_{ad} = 15K for a ΔH = 5T [6]. Subsequent studies on the substitution of Gd with other rare-earth metals have provided evidence for a consequent reduction in the MCE [44].

The GMCE has also been observed in itinerant-electron compounds such as $LaFe_{13-x}Si_x$, and in general, a significant amount of research has been conducted on the magnetocaloric properties of the La[Fe(Si,Al)]$_{13}$ family (a comprehensive review can be found in reference [48]). The possibility of tuning the transition temperature with composition in such systems has been explored by Gutfleisch *et al.*, through the variation of x and/or hydrogenation [49, 50]. $LaFe_{13-x}Si_x$ is a strong candidate for cooling devices, since it undergoes a first order field-induced itinerant-electron metamagnetic phase transition (FM-PM) [51, 52]. Jia *et al.* have determined that a decrease in x results in a depression of the T_C and an increase in x causes a decrease in the volume contraction, which results from the phase transition [53]. Although the magnetic entropy change in $LaFe_{13-x}Si_x$ is dominant, the lattice entropy change is comparably large and counteracts most of the magnetic one. Hence, a more detailed, theoretical understanding of magneto-elastic/structural transitions is required to understand the MCE of such materials.

In 2004, Gama *et al.* [54] reported on the existence of a pressure-induced colossal MCE in MnAs. The reported values for MnAs exceeded those of many active refrigerant materials, hence the term *colossal*. MnAs undergoes a first order magneto-structural transition from a FM-hexagonal structure to a PM-orthorhomic structure, at a transition temperature T_t (not exactly a conventional type Curie temperature) of 318K. It is considered to be a good candidate, since the ΔS_M value is -30JK^{-1}kg^{-1} and the ΔT_{ad} for ΔH = 5T is 13K [55]. Unfortunately, its usage is limited due to a considerably large thermal hysteresis and also due to arsenic being a poisonous constituent. This has led to a strong effort to develop arsenic-free alloys with comparable, or even improved, magnetocaloric properties. Substitution of As by Sb in the compound, $Mn(As_xSb_{1-x})$ reduces the thermal hysteresis and also decreases the transition temperature to 230K at x=0.3, whilst maintaining first-order magneto-structural properties. The MCE is reduced slightly such that, ΔS_M is in the range of -25 to -30JK^{-1}kg^{-1} and ΔT_{ad} for ΔH = 5T is 10K [55,56]. Moreover, through the addition of Fe and P, the alloy $MnFeP_xAs_{1-x}$ maintains first order transition properties near room temperature for 0.26≤x≤0.66 [57]. The Mn-Fe-P-Si compounds with a hexagonal Fe_2P-type structure are also promising candidates, since the GMCE exhibited can be tuned by varying the Mn:Fe, P:Si ratio.

In addition, the thermal hysteresis can be reduced simultaneously [58].

Ferromagnetic Heusler alloys such as Ni-Mn-Z (Z = Ga,In,Sn,Sb), which exhibit either a positive or negative MCE, depending on their stoichiometry, have attracted much attention in recent years. In non-stoichiometric $Ni_{2+x}Mn_{1-x}Ga$ alloys, a coupled magneto-structural transition from FM-martensite to PM-austenite takes place [59–61]. A positive MCE is displayed in the composition range of $0.18 \leq x \leq 0.27$. The reasoning behind the large MCE exhibited by such materials is related to the sum of entropy changes associated with the transition. Such field-induced magneto-structural transitions resulting from the coupling of magnetic and structural degrees of freedom are promising features for magnetocaloric applications.

3.4 Manganites as Magnetocaloric Materials

A class of materials for which the ΔS_{MAX} is shown in Fig. 3.3 but is not discussed in the previous section are the La-based manganites (or manganese oxides), which are transition metal oxides. This particular class of materials, displays a rich diveristy of crystallographic, magnetic and electronic phases, attributed to a strong interplay between spin, charge, orbital and lattice degrees of freedom. Manganites are promising candidates for magnetocaloric applications, since they are cheap, non-toxic, resistant to corrosion, easy to manufacture and have easily tunable transition temperatures [19]. In transition metal oxides, Mn can exhibit a magnetic moment as large as $5\mu_B$. This is one of the factors contributing to the considerable MCE exhibited by manganites. As a consequence of the effects of strong electron correlation, a complete microscopic understanding of the physics underlying the properties of manganites has not yet been achieved. A thorough understanding of the magnetocaloric properties of functional oxides has been an important issue for magnetic refrigeration technology. In this research, the primary focus is the characterisation of the strong interplay between the electronic and geometrical structure of $La_{1-x}Ca_xMnO_3$ manganites, as well as a quantitative theoretical description of the MCE in doped manganites, for the implementation of such materials in magnetic refrigeration technology.

3.4.1 Structure and Properties

In this section, the perovskite manganite structure will be discussed since it is directly related to its magnetocaloric behaviour and properties. Manganites belong to a class of distorted perovskites, which have the chemical formula, ABO_3. Fig. 3.4 shows the ideal cubic perovskite structure.

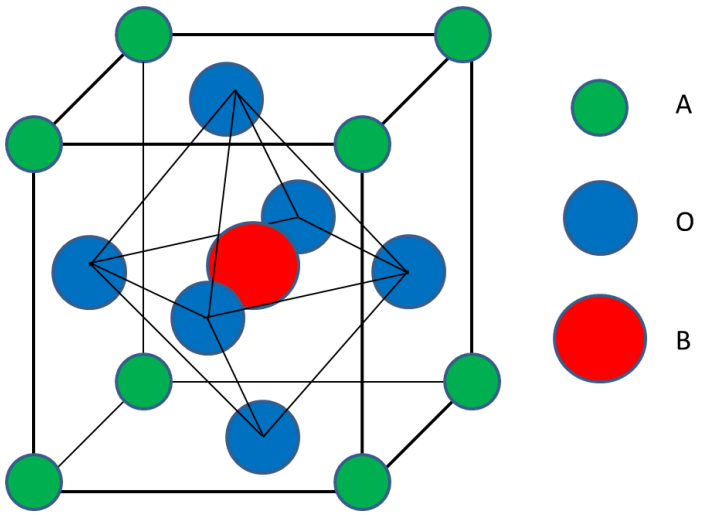


Figure 3.4: The ABO_3 cubic perovskite structure packed with BO_6 octahedra, which are connected at the vertices.

$LaMnO_3$ is the parent compound for La-based manganites and crystallises in the orthorhombic structure, which is a modification from the cubic perovskite structure. One of the possible origins in lattice distortion is the deformation of the MnO_6 octahedra arising from the Jahn-Teller (JT) effect. In $LaMnO_3$, the Mn ions have a formal charge of 3+ with a $3d^4$ ($t_{2g}{}^3e_g{}^1$) electronic configuration. The electronic structure is however more complicated than this simplified ionic model. Nevertheless, this approach is useful to outline the following important interactions, which are depicted in Fig. 3.5: The crystal field, caused by the MnO_6 octahedron of surrounding negative charges, splits the fivefold degenerate $3d$ orbital into higher energy doubly degenerate e_g ($d_{x^2-y^2}$, d_{z^2}) states and lower energy triply degenerate t_{2g} (d_{xy}, d_{xz}, d_{yz}) states. There is a strong on-site ferromagnetic coupling, U_H between the e_g and t_{2g} electron spin, which is a consequence of Hund's rule. The e_g degeneracy is lifted by a JT distortion of the MnO_6 octahedra.

Another lattice distortion comes from the ionic radii mismatch, which affects the connective pattern of the MnO_6 octahedra. This distortion is governed by the tolerance factor t (characteristic parameter commonly used to describe manganites), which is defined as,

$$t = \frac{r_A + r_O}{\sqrt{2}(r_B + r_O)} \tag{3.10}$$

where r_A, r_B and r_O represent the average ionic radii of each element. For t=1,

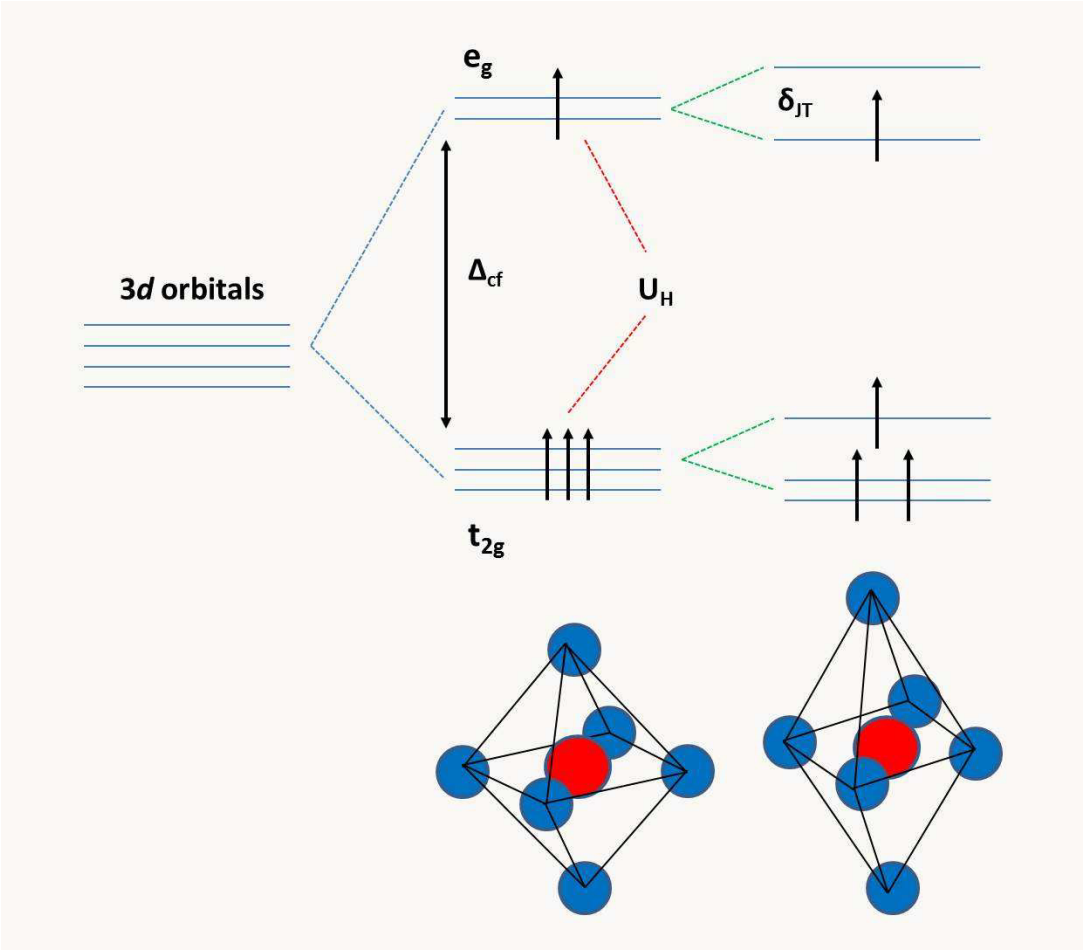


Figure 3.5: The crystal-field splitting of the five-fold degenerate atomic $3d$ levels into lower energy (triply degenerate) t_{2g} and higher energy (doubly degenerate) e_g levels. The JT distortion of MnO_6 octahedron further lifts each degeneracy. (This figure is modified from Ref. [62].)

the cubic structure in Fig. 3.4 is realised. However, for $0.96<t<1$, the lattice structure becomes rhombohedral and for $t<0.96$, the structure is transformed into orthorhombic [63].

3.4.2 Doped Perovskite Manganites

An important feature of perovskites is that the structure is very robust against chemical modifications at the A-site. Doping at the La-site is of interest since the exchange interaction could be modified, potentially changing the magnetic and hence, the magnetocaloric properties. Manganites with the general formula $R_{1-x}A_xMnO_3$ (R being a trivalent rare earth and A a divalent earth alkaline metal) are perovskite structured

oxides, which display a range of interesting phenomena, such as high temperature superconductivity [64, 65], colossal magnetoresistance (CMR) [16, 66–68] and the magnetocaloric effect (MCE) [19, 69, 70]. The properties of manganites are stongly dependent on the doping concentration x as well as external variables, such as temperature, pressure and electric or magnetic fields.

Experimental studies on manganites doped with earth alkaline elements, such as Ca, Ba and Sr, have been the subject of intense study since the discovery of CMR [15, 16]. A number of stable magnetic phases exist in various doped perovskite manganite systems. Substition of La with ions of a larger radius (i.e. Sr, Ba and Pb) could possibly allow tuning of T_{C} without reducing the MCE. The $\mathrm{R}_{1-x}\mathrm{A}_x\mathrm{MnO}_3$ series, and the $\mathrm{La}_{0.67}\mathrm{Ca}_{0.33}\mathrm{MnO}_3$ composition in particular, has been considered a potential candidate for magnetic refrigeration. The experimentally determined ΔS_{iso} value and Curie temperatures of a range of compositions of this manganite series are given in Table. 3.1. Generally, the temperature at which the change in magnetic entropy peaks normally coincides with the Curie temperature in magnetocaloric manganites. However, it is evident from Table. 3.1 that there is a large dispersion in the MCE data. It is worth noting that complexities such as chemical disorder [71, 72], nonstoichiometry and inhomogeneities [12] are expected to affect the magnetocaloric properties [73–75] and could explain the large variation, but this is not known.

The MCE in $\mathrm{La}_{1-x}\mathrm{M}_x\mathrm{MnO}_3$ films (where, M=Ca, Sr, Ba) was first reported by Morelli *et al.* [15]. Later, Guo *et al.* reported that the magnetic entropy change, ΔS_M, in $\mathrm{La}_{0.75}\mathrm{Ca}_{0.25}\mathrm{MnO}_3$ polycrystalline samples was of the same order of magnitude as that displayed by Gadolinium (for the same field change) [18, 76]. However, polycrystalline manganites have been found to display non-uniform MCE curves, when compared to single crystalline materials [19]. The $\mathrm{La}_{2/3}\mathrm{Ca}_{1/3}\mathrm{MnO}_3$ compound exhibits the largest MCE amongst the compositions investigated for this series of manganites, as can be seen in Table. 3.1. However, the T_{C} is 267K which is quite below room temperature [18, 76–79]. Although this could potentially limit the usage of this composition as an active magnetic refrigerant at RT, Hueso *et al.* acknowledged the possibilty of tuning the transition temperature without suppressing the large MCE values of $\mathrm{La}_{0.67}\mathrm{Ca}_{0.33}\mathrm{MnO}_3$ nanopaticles, synthesized by sol-gel techniques [80]. Later studies reported that the magnitude of the magnetic entropy change ΔS_M is inversely proportional to the grain size. Experimentally, in $\mathrm{La}_{0.75}\mathrm{Ca}_{0.25}\mathrm{MnO}_3$, an anomalous thermal expansion is observed at the transition [81]. These studies also confirm that strong structural and magnetic coupling at T_{C} can greatly influence ΔS_M. When compared to the intermetallic compounds and alloys of rare earths, the tunability of T_{C}

via doping, lower cost, higher electrical resistivity and chemical stability implies that the manganites are strong candidates for magnetic refrigeration at RT.

Composition	T_C (K)	ΔH (T)	-ΔS_{iso} (Jkg^{-1}K^{-1})	Reference
$La_{0.80}Ca_{0.20}MnO_3$	230	1.5	5.50	[18]
$La_{0.80}Ca_{0.20}MnO_3$	176	1.5	3.67	[82]
$La_{0.75}Ca_{0.25}MnO_3$	224	1.5	4.70	[76]
$La_{0.70}Ca_{0.30}MnO_3$	256	1.0	1.38	[83]
$La_{0.70}Ca_{0.30}MnO_3$	227	1.0	1.95	[84]
$La_{0.67}Ca_{0.33}MnO_3$	260	1.5	4.30	[18]
$La_{0.67}Ca_{0.33}MnO_3$	259	3.0	2.60	[85]
$La_{0.67}Ca_{0.33}MnO_3$	252	5.0	2.06	[15]
$La_{0.67}Ca_{0.33}MnO_3$	267	3.0	6.04	[77]
$La_{0.60}Ca_{0.40}MnO_3$	263	3.0	5.00	[86]
$La_{0.55}Ca_{0.45}MnO_3$	238	1.5	1.90	[18]

Table 3.1: The Curie temperature T_C and magnetocaloric potential ΔS_{iso} for compositions of the $La_{1-x}Ca_xMnO_3$ manganite series [19].

Since manganites are characterized by rich phase diagrams, many phases compete at low temperatures. Consequently, phase separation (PS) can occur leading to inhomogeneous states [12]. PS between hole undoped antiferromagnetic and hole-rich ferromagnetic regions in manganites has been reported using scanning tunneling spectroscopy (STS) [87], neutron scattering [88, 89] and x-ray absorption [12, 90–92]. More recently, it has been found that multiple-phase transitions occur in PS manganites such as $La_{5/8y}Pr_yCa_{3/8}MnO_3$ where the MCE peaks with both positive and negative values in a wide temperature range [93, 94]. Hence, PS manganites can be used to broaden the temperature range and improve regenerative magnetic refrigerator designs. The occurence of PS could be atrributed to strain [95] as well as local chemical disorder [71,72]. However, the exact origins of such inhomogeneities and the key mechanisms involving PS are unclear.

3.5 Modelling of the Magnetocaloric Effect

The MCE has been studied in many materials, largely due to experimental efforts, as described in the previous sections. A theoretical understanding of the magnetocaloric properties of materials is, however, an essential step towards designing materials with improved performance. Accurate theoretical models of the MCE could notably simplify

the design process. However, an evident shortcoming of the theoretical aspect of magnetocaloric materials is the scarcity of studies carried out to disentangle and quantify the separate contributions to the entropy change across a phase boundary, particularly from an *ab initio* perspective. Nevertheless, this section reviews some signicant theoretical works in the field of magnetocaloric materials.

First principles calculations have commonly been carried out to investigate the electronic and magnetic properties of magnetocaloric materials [96–105]. In a number of such studies, the exchange coupling constants and magnetic moments have been extracted and subsequently used as parameters in thermodynamic models, which allow one to compute finite temperature macroscopic variables. Electron correlation effects on the electronic structure of $Gd_5Si_2Ge_2$, which exhibits a magnetostructural transition close to RT, have been studied by Harmon *et al.* and Paudyal *et al.*, using the tight binding linear muffin-tin orbital method, within the framework of the local spin density approximation [96,98]. The combination of first principle calculations and magnetothermodynamic models, such as the Bean-Rodbell model [37], provides a useful analysis of the magnetostructural transition since, in this case, the predicted transition temperature and associated magnetic entropy change were in good agreement with experimental values [98]. Although such studies have enabled a more in-depth understanding of alloys such as $Gd_5Si_2Ge_2$, the ability to predict candidate materials, without synthesising and measuring the MCE, has been relatively limited.

Theoretically, metamagnetic transitions have also been of interest for the MCE, which are in effect, order-order transitions. For example, there has been a recent growth in studies related to the origin and tunability of metamagnetism in Fe_2P. DFT calculations conducted by Delczeg-Czirjak *et al.* to disentagle entropic contributions, determined that the vibrational component stablises the hexagonal phase of Fe_2P, whereas the electronic and magnetic contributions favour the orthorhombic structure in Si-substituted $Fe_2P_{1-x}Si_x$ alloys [106]. Further, Gercsi *et al.* were able to determine preferential sites for the dopants and the consequent increase in the Fe moment [107]. Such studies indicate the potential of first principle calculations in optimising the magnetocaloric properties of metamagnetic materials. However, it must be noted that finite temperature effects are not incorporated explicitly. First principles calculation techniques have also been developed and implemented for chemically disordered materials, i.e., the *Korringa-Kohn-Rostoker* (KKR) method with the *coherent potential approximation* (CPA) [108]. More recently, Staunton *et al.* have adopted the *disordered local moment* (DLM) theory, which has been used in conjunction with the statistical mechanics of local moments to predict the temperature dependence of the

metamagnetic critical fields in CoMnSi-based alloys [105].

The Monte Carlo Approach has also been used to study the MCE in several materials. For example, Nòbrega *et al.* [109] used this approach to study the MCE in R_5Si_4 (R=Gd,Tb), where a model Hamiltonian consisting of three terms was developed. These terms describe the spin-spin interaction, the single ion anisotropy and the Zeeman interaction of the total angular momentum with an external field. The determined ΔS_M and ΔT_{ad} were found to be in good agreement with experimental data. Moreover, a smooth increase in the magnetic entropy around the ordering temperature was observed, which was absent in corresponding theoretical calculations within the mean field approach. Similarly, Buchelnikov *et al.* also implemented the Monte Carlo method to determine the magnetocaloric properties of the Heusler alloy Ni-Mn-Ga [59, 99], which undergoes a magnetostructural phase transition, as mentioned previously. *Ab initio* calculations of the the magnetic exchange parameters were carried out to determine the magnetic energy scales, which allowed a first principles calculation of T_C. The model Hamiltonian implemented to describe the coupling of magnetic and structural degrees of freedom consisted of the q-state Potts [110] and the Blume-Emery-Griffiths (BEG) [111] model, which described the martensitic transformations in $Ni_{2+x}Mn_{1x}Ga$ accurately. Further, Monte Carlo studies by Restrepo-Parra *et al.* reported the variable-temperature magnetic properties of the manganite series $La_{1-x}Ca_xMnO_3$ through the implementation of the Heisenberg Hamiltonian with an additional term corresponding to the magnetocrystalline anisotropy, which is dependent upon the stoichiometry [112, 113]. Subsequently, the determined critical temperatures for the compositions considered were found to be in good agreement with experimental reports.

An alternative to first principles modelling is the implementation of thermodynamic models. In such models, the system can be described using macroscopic quantities, which are typically obtained from experimental data. Thermodynamic models, generally, allow one to gain an understanding of critical behaviour in first [114, 115] and second order phase transition materials [116–118]. Such models have contributed towards an understanding of the physics behind the MCE (a succinct review can be found in reference [44]).

4

Theoretical Concepts and Techniques

In this chapter, the level of theory and background of the quantum mechanical approaches used to model manganites will be detailed. Foremost, the electronic structure methods, which form the basis of our simulations, will be discussed. This will be followed by a description of the approximations that are made to carry out such simulations. Details of the computational code used and the procedure of geometry optimisation will then be outlined. Subsequently, the Monte Carlo approach implemented to determine macroscopic thermodynamic quantities will be described.

4.1 Electronic Structure Methods

The use of reliable *ab initio* electronic structure methods, combined with experiments, is key to providing a detailed insight into the structural and electronic properties of matter. Due to the availability of increasingly powerful computational tools in the last few decades, many theoretical methods have been developed to study such properties of materials. A first principles description of matter is based on the determination of the ground state, which is dependent on the atomic constituents, such as the electrons and nuclei. The total energy of the ground state is determined through minimisation of the energy with respect to the electronic and nuclear coordinates. This implies a complex many-body problem of interacting particles. Different methods, in which various approximations are made, have been employed to improve the accuracy of the many-body Schrödinger Equation (SE) solution at lower computational costs. The suitability of a particular method is dependent on several criteria, which are influenced

by the structure and electronic features of the system being studied.

In this thesis, quantum mechanical simulations have been carried out in the framework of the Density Functional Theory (DFT). This commonly employed electronic structure method has been known to provide a reasonably accurate description of the structural and electronic properties of a wide range of materials. The purpose of adapting this method in particular is to interpret existing experimental data and develop a first principles description of the MCE in manganites, as well as, parameterisation of the Ising Hamiltonian, in order to direct experimental efforts towards designing new and improved magnetocaloric materials. Further clarification and a detailed description of the electronic structure methods mentioned herein could be found in References [119–121].

4.1.1 The Schrödinger Equation

In principle, the ground state energy, electronic structure and properties of a non-relativistic many-body system can be determined from the time-independent non-relativistic SE, which is arguably the most fundamental equation in *ab initio* electronic structure methods and is given by,

$$\hat{H}\Psi = E\Psi \tag{4.1}$$

where $\hat{H}$ is the electronic Hamiltonian operator, E is the energy of the many-body system and Ψ is the many-body wavefunction.

The SE can be solved analytically for the hydrogen atom, which gives us an expression for single electron orbitals. However, in order to describe the quantum mechanical behaviour of a many electron system, it is necessary to calculate the many-body wavefunction for the system. Solving the Schrödinger equation for the interaction of many electrons is, however, a complex problem, which can be considered to be beyond the capability of quantum chemists and solid state physicists. Due to the complexity of the many-body problem, the following approximations are made to solve the Schrödinger equation:

1. Born-Oppenheimer Approximation
2. The Variational Principle
3. Hartree Approximation

Such approximations are discussed in the following paragraphs. To begin with, if one considers the *Born-Oppenheimer Approximation*, which is central to quantum

chemistry and is based on the assumption that the mass of the nuclei is considerably larger than the mass of an electron (by a factor of ∼2000). It then follows that the velocity of the nuclei must be very low and is therefore negligible relative to the velocity of the electron. The Hamiltonian operator, given in Equation. 4.2 [119], is a sum of three terms: the kinetic energy (operator), the interaction of the electrons N with an external potential generated by M nuclei, and the electron-electron interaction, respectively.

$$\hat{H} = -\sum_{i=1}^{N} \frac{1}{2}\nabla_i^2 - \sum_{i=1}^{N}\sum_{A=1}^{M} \frac{Z_A}{r_{iA}} + \sum_{i=1}^{N}\sum_{i>j}^{N} \frac{1}{r_{ij}} \tag{4.2}$$

In addition, the total wavefunction can be expressed as a product of the electronic wavefunction Ψ_e (function of the electron coordinates but has a parametric dependence on the nuclear coordinates) and nuclear wavefunction Ψ_n (function of the nuclei coordinates only) 4.3.

$$\Psi = \Psi_e \Psi_n \tag{4.3}$$

Secondly, a core component of many quantum mechanical codes that determine the ground state of a system is *the variational principle* which states that the approximated energy of a state is higher than that of the ground state unless Ψ corresponds to Ψ_0. This can be written quantitatively as

$$E\left[\Psi\right] \geq E_0 \tag{4.4}$$

where the ground state energy E_0 can be determined by searching all possible wavefunctions and identifying the wavefunction Ψ_0, which minimises the total energy. Such approximations simplify the problem of solving the SE greatly.

Further attempts to solve the quantum many-body problem were made by Hartree [122] and Fock [123]. The Hartree-Fock Method is the simplest parameter-free, wavefunction-based electronic structure method, which describes electrons under the influence of a mean field potential. In the Hartree-Fock approximation, electron correlation is not implemented. The many-body wavefunction is the Slater determinant, which is expressed as a product of one-electron wavefunctions. More details on Hartree-Fock theory can be found in Ref. [124].

Although the Hartree-Fock approach yields a good description of materials with well localised electrons, the computation of the non-local exchange potential yields unsatisfactory results for metallic systems. This method also tends to underestimate

bond lengths and overestimates binding energies compared to experimental results, due to the neglect of electron-electron correlation effects. Moreover, a large basis set is required to retrieve an adequate level of accuracy.

The Hartree Approximation is a common starting point for a number of more recent improved approaches, which are able to accurately predict the chemical properties of molecular and crystalline systems. However, the use of improved methods where the absence of electron correlation is addressed, such as Configuration Interaction (CI), Møller-Plesset Perturbation Theory (MP), Coupled Cluster (CC) and Quantum Monte Carlo (QMC), is limited due to their rather extensive demand of computational resources [120].

4.1.2 Density Functional Theory (DFT)

An alternative approach to go beyond wavefunction-based electronic structure techniques, namely *Density Functional Theory*, can be applied to compute the ground state energetics of a system. In comparison to other quantum mechanical methods, DFT can provide useful results at a reasonable computational cost for a wide range of materials. The basis for this theory is the proof by Hohenberg and Kohn [120] that the ground state energy is determined completely by the electron density $\rho(\mathbf{r})$. Consequently, the number of variables is reduced to three (spatial variables of the electron density), as opposed to $3N$ in the Hartree-Fock method. The theorems of DFT first proposed by Hohenberg and Kohn [125] in 1964 may be stated as follows:

1. The electron density determines the external potential V_{ext}. For a given ground state charge density $\rho_0(\mathbf{r})$ it is possible to calculate the corresponding ground state wavefunction $\Psi_0(\mathbf{r}_1,\mathbf{r}_2,.....\mathbf{r}_N)$.

2. The ground state wavefunction must minimize the energy. In accordance with the variational principle, the minimum approximated energy is greater than or equal to the ground state energy. Consequently, the density functional theory is restricted to studies of the ground state.

The proof of this theorem has been given by Hohenberg and Kohn, as well as Levy in 1979 [126]. It was argued that the local maxima (which are also referred to as cusps) in the electron density define the position of the nuclei. In addition, the height of the cusps defines the corresponding nuclear charges and integration of the electron density over all space gives the total number of electrons N. Hence, the Hamiltonian operator,

which depends only on the positions and atomic numbers of the nuclei and the total number of electrons, can be expressed trivially in terms of the electron density.

The theorems above lead to the underpinning statement of DFT, which is given by Equation. 4.5, where $E[\rho]$ is a universal functional and μ is the electronic chemical potential.

$$\delta \left[E\left[\rho\right] - \mu \left(\int \rho(\mathbf{r}) d\mathbf{r} - N \right) \right] = 0 \tag{4.5}$$

The energy functional $E[\rho]$ can be used to determine the ground state energy, E_0 as well as the charge density $\rho(\mathbf{r})$. This functional is divided into the following components, which are explicitly dependent upon the charge density only:

$$E\left[\rho\right] = T\left[\rho\right] + V_{ext}\left[\rho\right] + V_{ee}\left[\rho\right] \tag{4.6}$$

where $T[\rho]$ is the kinetic energy, $V_{ext}[\rho]$ is the electron-nucleus interaction and $V_{ee}[\rho]$ corresponds to the electron-electron interaction.

In principle, if the exact functionals are known, the exact ground-state energy may be determined. While the second term is defined entirely by V_{ext}, the exact dependence of the kinetic and electron-electron interaction energies on the density is unknown. In a key breakthrough, Kohn and Sham realized that things would be considerably simpler if the Hamiltonian were one for a non-interacting system of electrons moving in an effective field. A fictitious system of N (non-interacting) electrons is considered, which is described by a single determinant wavefunction in N orbitals (called Kohn-Sham orbitals). The overall ground state density of the $fictitious$ system is the same as that of the $real$ system, in which the electrons do interact. The energy functional is divided into the following components,

$$E\left[\rho\right] = T_{ni}\left[\rho\right] + V_{ext}\left[\rho\right] + V_H\left[\rho\right] + \Delta T\left[\rho\right] + \Delta V_{ee}\left[\rho\right] \tag{4.7}$$

where the terms on the r.h.s. refer, respectively, to the kinetic energy of the non-interacting electrons, the electron-nucleus interaction, the classical electron-electron interaction, the correction to the kinetic energy due to the non-interacting nature of electrons assumed and all corrections to the classical treatment of the electron-electron interaction energy. The problematic terms $\Delta T[\rho]$ and $\Delta V_{ee}[\rho]$ are then summed to form a term E_{xc}, typically referred to as the exchange-correlation energy, which includes the effects of quantum mechanical exchange and correlation. The exchange-correlation energy is therefore the only unknown functional in the calculation of the energy and a

precise description of the functional becomes the most important factor in influencing the accuracy of DFT calculations.

4.1.3 Exchange-Correlation Functionals

The development of exchange-correlation functionals has been a key research area in quantum chemistry and material science for the last few decades. A general classification of the different DFT methods is based on the degree of locality of the exchange-correlation functional (local, semi-local, or gradient-dependent, and non-local) adopted. Such functionals and their performance are discussed in this section.

The functional dependence of E_{xc} on the electron density is commonly expressed as

$$E_{xc}[\rho] \approx \int \rho(\mathbf{r})\varepsilon_{xc}(\rho(\mathbf{r}))d\mathbf{r} \tag{4.8}$$

where the energy density ϵ_{xc} is treated as a sum of the individual exchange and correlation contributions. In the *Local Density Approximation* (LDA) [127], the value of ϵ_{xc} at some point $\mathbf{r}$ could be computed exclusively from the 'local' value of the electron density ρ at that particular point. However, the only functionals, which conform to this definition and have seen much application, are those that derive from the analysis of a uniform electron gas (*jellium*), as in the case of the Thomas-Fermi-Dirac approximation. The spin has been ignored up to to this point, but has easily been incorporated in the LSDA (*Local Spin Density Approximation*), a natural extension to the LDA, by considering functionals of the individual α and β electron densities.

The electronic properties of systems with delocalised electrons such as metallic conductors (*i.e.* those whose electronic structure closely resembles the uniform electron gas) are also described correctly within the LDA, which is partly due to the systematic self-cancellation of errors in the exchange and correlation energies. However, studies have shown that LDA tends to underestimate lattice constants by 2-3% for metals and insulators [128–130]. Since the local exchange potential does not consider the electronic redistribution in bonds, the computed binding energies of various systems are inaccurate. Bond strengths are generally overestimated by 20-30% [131] as the the exchange contribution (to the bond strengths) is usually much larger than the correlation contribution. Moreover, electronic band gaps are typically underestimated, which is more significant for strongly correlated systems.

It was realised very early that the local uniform density at each given point is not a reasonable approximation for the varying electron densities of many systems. The LDA has been improved by adding a functional that also depends on the gradient of the

electron density $\nabla\rho$. Such adaptations of the LDA are commonly known as semi-local *Generalised Gradient Approximations* (GGAs) methods and have the form:

$$E_{xc}^{GGA} \approx \int \rho(r)\varepsilon_{xc}(\rho, |\nabla\rho|)d\mathbf{r} \tag{4.9}$$

In general, GGAs give a reliable description of chemical bonds (such as, covalent, metallic and hydrogen bonds) [132, 133] and a reasonably accurate estimate of binding energies of small molecules and solids [131], when compared to LDA functionals. However, GGAs fail to describe insulating (localised electron) systems accurately and also provide a rather inaccurate description of weak interactions, such as dispersion forces. Logically, the next step in the development of GGAs is to include a dependence on the second derivative of the electron density. Such functionals are known as *meta*-GGAs and provide a further improvement in the binding energies when compared to GGAs. However, higher-order corrections are exceedingly difficult to calculate. Furthermore, the issue with self-interaction in heavily localised systems, such as ionic solids, still remains [21, 134, 135].

Hybrid functionals include a portion of the exact Hartree-Fock exchange energy. Consequently, they require more computational effort when compared to non-hybrids. The B3LYP (Becke, three-parameter, Lee-Yang-Parr) functional, developed by Becke [136] is a hybrid of the exact, Hartree-Fock exchange with local and gradient corrected exchange terms. B3LYP is a commonly used functional and has the form [22, 137, 138]:

$$E_{xc}^{B3LYP} = (1-a_0)E_x^{LSDA} + a_0E_x^{HF} + a_x\Delta E_x^B 88 + a_c\Delta E_c^{LYP} + (1-a_c)E_c^{VWN} \tag{4.10}$$

The coefficients (a_0=0.2, a_x=0.72, and a_c=0.81) are determined by fitting predicted values to a set of atomization energies, proton affinities, ionization potentials and total atomic energies. ΔE_x^{B88} is Becke's correction to the exchange functional. E_c^{LYP} is the Lee-Yang-Parr correlation functional and E_c^{VWN} is used to provide the different coefficients of the local and gradient corrected correlation functionals.

The hybrid exchange B3LYP functional has been proven to be accurate in computing the binding energies, geometries and vibrational frequencies of a broad range of molecules and solid-state materials, when compared to GGA methods [120, 131, 134, 135]. Typically, such properties of systems with strong correlation effects [139] are described significantly well, since the incorporation of 20% Fock exchange corrects the self-interaction error. Furthermore, the combination of a non-local and a

semi-local exchange potential increases the flexibility of the functional and, thus, its ability to provide accurate results for a range of systems, from strongly-localised to itinerant-electron. B3LYP also provides an accurate description of magnetic moments and values of magnetic coupling constants, close to experimental values, in strongly correlated systems [23–27, 139]. In contrast, LSDA is known to overestimate, and HF to underestimate, the magnetic couplings [23]. Therefore, the B3LYP functional is an appropriate functional for describing the electronic and magnetic properties of magnetic materials.

4.2 The Basis Set Approximation

In this section, the basis set approximation is introduced, which is essentially a method of choosing mathematical functions to construct a trial wavefunction. The unknown one-electron HF/KS wavefunctions ψ_i are expanded in a linear combination of atomic orbitals (LCAO), χ_μ,

$$\psi_i(\mathbf{r}) = \sum_\mu a_\mu^i \chi_\mu(\mathbf{r}) \tag{4.11}$$

where a_μ^i are the expansion coefficients. The basis functions are commonly approximated using plane-wave or local orbitals. Each atomic orbital χ_μ can be expanded into another set of known functions, G_j:

$$\chi_\mu(\mathbf{r}) = \sum_j c^j G_j(\mathbf{r}) \tag{4.12}$$

In principle, an exact mathematical representation of the orbitals would require an infinite set of basis functions. This is, nonetheless, impossible in real calculations and, in practice, a finite set of basis functions are used. A larger basis set gives an improved representation of the orbitals. However, the basis set is generally a compromise between the computational cost and accuracy.

Atomic orbital basis sets (also referred to as *Gaussian basis sets* herein) have been used in this research, and are discussed in the following subsection 4.2.1. The plane wave approach, which is widely used amongst the solid state community will also be described briefly (in subsection 4.2.2) for comparison purposes. The choice of whether to use a plane wave or Gaussian basis set is often dependent on the system being investigated.

4.2.1 Atomic Orbital (Gaussian) Basis Sets

Molecules can be described as an assembly of slightly perturbed atoms. This is the fundamental idea behind using localised atomic orbitals in a periodic system. Further, an atomic-like basis set allows easier population analysis and computation of properties such as the projected densities of state.

Historically, in quantum chemistry , Slater Type Orbitals (STOs) have been used to describe basis functions, which are similar to the eigenfunctions of the hydrogen atom. Slater type orbitals exhibit an exponential dependence on distance and the atomic orbitals have a cusp at the nucleus. However, STOs suffer from a fairly significant limitation. Some of the integrals, specifically the three- and four- center bielectronic integrals have no analytical form. Moreover, the evaluation of the integrals is time consuming and computationally inefficient.

In 1950, Boys [140] determined that the requirement to have an analytical solution of the four-index integral is to change the radial decay of STOs from e^{-r} to e^{-r^2}. Thus, the atomic orbitals have the form of a Gaussian function. This improves the calculation of integrals greatly, when compared to STOs. Hence, the all-electron Gaussian Type Orbitals (GTO) are used widely as basis functions and have the general Cartesian form:

$$G_{\alpha,l_x,l_y,l_z}(x,y,z) = \zeta x^{l_x} y^{l_y} z^{l_z} e^{-\alpha r^2} \tag{4.13}$$

where $x^{l_x} y^{l_y} z^{l_z}$ is the angular part of the orbital and $e^{-\alpha r^2}$ is the radial (Gaussian) part; the α exponent controls the width of the GTO. ζ is a normalisation constant and the sum of l_x, l_y and l_z specifies the type of orbital for e.g. l_x+l_y+l_z=0 is an s-type GTO (and has spherical symmetry). In order to describe the orbitals accurately and increase computational efficiency, a minimum number of basis sets is used, where only an s single function is used for each occupied orbital. The Gaussian type basis functions are expanded as a linear combination of individually normalised *primitive* Gaussians.

The size of the basis set can vary from the minimum basis set to more complicated basis sets, for example, the split valence double zeta (SVDZ) where two functions are used for each minimal basis function. Certain orbitals are often grouped together, such as sp shells (which are essentially s and p functions with the same set of exponents). Thus, the number of electronic integrals, are reduced and effectively, the speed of the calculations increases.

4.2.2 Plane-Wave (PW) Basis Sets

Basis sets composed of sets of PWs form a complete orthonormal basis set and can be applied universally to any system. In PW calculations, the electron density is described as a linear combination of functions, which have the form:

$$\Psi(\mathbf{r}) = \sum_{\mathbf{G}} c_k^{\mathbf{G}} e^{i(\mathbf{k}+\mathbf{G})\cdot\mathbf{r}} \tag{4.14}$$

where $\mathbf{k}$ is the reciprocal wave vector restricted to the first Brillouin zone (BZ), $\mathbf{G}$ is the reciprocal lattice vector and $\sum_{\mathbf{G}}$ over the Fourier components $c_k^{\mathbf{G}}$ of the one-electron orbitals.

Generally, PWs up to a certain kinetic energy, which is referred to as a plane wave cutoff, are used. The PW cutoff could be increased, which corresponds to the addition of more PWs to the basis set, until convergence with respect to a particular property is achieved. A limitation of PWs, when compared to GTO basis sets, is that a prohibitively large number of basis functions are required to accurately represent valence wavefunctions in proximity of the nuclei. In addition, great difficulties are encountered in describing semi-core and core electron densities. In order to reduce computational requirements and to describe core electrons more practically, pseudopotentials are more commonly used. Thus, all-electron calculations cannot be performed with PW basis sets. The main advantage of PW codes is the easier development and implementation of new functionalities, when compared to the localised basis functions. It must also be noted that the B3LYP-PW scheme does not provide results at the same level of accuracy as the all-electron B3LYP approach in the study of magnetic systems, particularly strongly localised electron systems [141].

4.3 Periodic Model

In DFT, an effective treatment of ideal crystal systems is to consider an infinite periodic system of unit cells (basis units), in either one dimension (polymers), two dimensions (surfaces or slabs) or three dimensions (bulk). We are interested in solving the SE for a periodic system. Therefore, it follows that the total potential V(r) must also be periodic.

$$V(\mathbf{r}) = V(\mathbf{r}+\mathbf{R}) \tag{4.15}$$

$\mathbf{R}$ is the primitive lattice translational vector, $\mathbf{R}$=$n_1\mathbf{a}_1$+$n_2\mathbf{a}_2$+$n_3\mathbf{a}_3$, where n_1, n_2

and n_3 are integers and $\mathbf{a}_1$, $\mathbf{a}_2$ and $\mathbf{a}_3$ are the real space lattice vectors. Inherently, the reciprocal lattice is defined using the vectors: $\mathbf{b}_1$, $\mathbf{b}_2$ and $\mathbf{b}_3$, which obey the orthogonality rule with respect to the real space lattice:

$$\mathbf{a}_i \cdot \mathbf{b}_j = 2\pi\delta_{ij} \tag{4.16}$$

The reciprocal lattice points are described using the wavevector, $\mathbf{k}$ ($\mid \mathbf{k} \mid = 2\pi/\lambda$). In the presence of a periodic potential, the wavefunction, $\psi(\mathbf{r})$ is given as:

$$\psi(\mathbf{r} + \mathbf{R}) = \psi(\mathbf{r})e^{i\mathbf{k}\cdot\mathbf{R}} \tag{4.17}$$

where $|\psi(\mathbf{r})|^2$ is the charge density. Any $\psi(\mathbf{r})$ differs only by a phase factor, $e^{i\mathbf{k}\cdot\mathbf{R}}$ between equivalent positions in the lattice. Equation 4.17 is more commonly known as *Bloch's theorem* [142] and its more general form is (a Bloch function): $\psi(\mathbf{r})$=$u(\mathbf{r})e^{i\mathbf{k}\cdot\mathbf{r}}$, where $u(\mathbf{r})$ is a periodic function with the periodicity of the lattice. The Bloch function allows one to exploit the translational symmetry of the periodic system. Hence, the SE can be solved for all the electrons in the unit cell at an infinite number of $\mathbf{k}$ points in the Brillioun zone. However, more practically, the total energy is converged to within the required accuracy with respect to the sampling of a finite number of equally spaced $\mathbf{k}$ points.

4.4 The CRYSTAL Code

The simulations of $LaMnO_3$ and the doped compounds: $La_{0.75}Ca_{0.25}MnO_3$ and $CaMnO_3$ are performed using the CRYSTAL09 [143] software package. The code is based on the expansion of the crystalline orbitals as a linear combination of a local basis set (BS) consisting of atom centered Gaussian orbitals. Calculations of the ground state energetics and properties of systems with three-dimensional (crystals), two-dimensional (slabs), one-dimensional (polymers) and zero-dimensional (atoms or molecules) periodicity can be performed using HF and DFT treatments of the exchange and correlation. The periodic model, which was discussed in section 4.3 has been implemented in CRYSTAL09.

The basis set for each atom must be defined in the CRYSTAL09 input. In this work, the Mn, O and Ca ions are described by a triple valence all-electron BS (Appendix A): an 86-411d(41) contraction (one s, four sp, and two d shells), an 8-411d(1) contraction (one s, three sp, and one d shells) and an 8-65111(21) contraction (one s, three sp, and two d shells), respectively; the most diffuse $sp(d)$ exponents are α^{Mn}=0.4986(0.249),

α^{O}= 0.1843(0.6) and α^{Ca}= 0.295(0.2891) Bohr^{-2}. The La basis set (Appendix A) includes a relativistic pseudopotential to describe the core electrons, while the valence part consists of a 411p(411)d(311) contraction scheme (with three s, three p and three d shells); the most diffuse exponent is α^{La}=0.15 Bohr^{-2} for each s, p and d [144].

4.4.1 Geometry Optimisation

The equilibrium structure of a system is determined through the exploration of the total energy minima and saddle points on the potential energy surface (PES). The determination of the most stable structure is of primary importance in the modeling of systems and several techniques have been proposed for the geometry optimisation of chemical systems [145]. Basic tools to describe the PES are the first- and second-derivatives. The number of local minima typically increases exponentially with the number of variables and therefore, exploring the entire PES is unfeasible. Consequently, the difficulty in determining the global minimum (which is usually desired) increases.

Finding the optimal geometry of a given structure is not a trivial task. The gradient-based algorithms have commonly been employed for geometry optimisation techniques [146]. The simplest is the *steepest descent* method, where a series of function evaluations are performed in the negative gradient direction. An approximate minimum may then be determined once the function starts to increase. The advantage of this algorithm is that it is simple and requires computational storage of the gradient vector only. If the minimisation is carried out accurately, the function value will always be lowered and, therefore, this method guarantees to approach a minimum (steepest descent never actually reaches the minimum). However, as the minimum is approached, the rate of convergence is rather slow (significantly slow if there is strong coupling between various degrees of freedom).

The *Conjugate Gradient* method is an improvement to the steepest descent method such that, each line search is not along the current gradient but along a line that is constructed. Therefore, it is 'conjugate' to the previous search direction(s). The first step is equivalent to a steepest descent step, however, successive searches are performed along a line, which is a mixture of the current gradient and previous search direction. This method requires slightly more computer storage when compared to the steepest descent method. However, Conjugate gradient methods have improved convergence characteristics when compared to the steepest gradient.

The more robust method is the *Newton Raphson*, which is implemented in most modern atomistic simulation software packages (including CRYSTAL). All diagonal

elements of the second derivative matrix , the Hessian, must be positive for a minimum. This method allows one to predict the distance that the current configuration is from the stationary point, as well as the nature of the stationary point. In comparison to the steepest descent and conjugate gradient methods, the Newton-Raphson method is only able to locate local minima. The construction and inversion of the Hessian matrix can also be expensive. Numerous updating schemes exist, where an approximation to the Hessian is made prior to the optimisation procedure and is updated every few steps, to obtain a better approximation and reduce computational costs (since the Hessian is not updated at every step). Such a scheme is the *Broyden-Fletcher-Goldfarb-Shanno* (BFGS) [147], which has been adopted for geometry optimisation in the CRYSTAL code.

4.5 Monte Carlo Methods

Monte Carlo Simulations are an important technique implemented in computational physics to study systems with a large number of coupled degrees of freedom, particularly in statistical mechanics. Such systems change in a stochastic manner and depend on random number sequences, generated during the simulation. Monte Carlo techniques use a class of computational algorithms and allow calculations of thermal averages for (interacting) many-particle systems, taking into account statistical fluctuations and their effects.

4.5.1 Metropolis Algorithm

A Monte Carlo code has been written, which applies the standard Metropolis Algorithm and has been used to generate lattice configurations of variables distributed with the correct Boltzmann weight. This algorithm has been implemented to calculate the mean energy for a Monte Carlo cycle in the following way. The energy of an initial lattice configuration is calculated. A random lattice site (i, j, k) is then selected and the spin state is flipped. The difference between the initial configuration, E_1 and the new, configuration, E_2 is determined by, ΔE=E_2-E_1. If ΔE<0, the new configuration is accepted. The transition probabilty is unity, since this is an importance sampling method. If however, ΔE>0, then, the transition probability factor is the Boltzmann factor:

$$p = e^{-\Delta E/k_B T} \tag{4.18}$$

In this case, a random number r is generated such that, $0< r <1$. If $r < p$, the new configuration is accepted otherwise, the spin is flipped to preserve the old configuration. In figure 4.1 a two-dimensional square lattice is depicted in which the nearest-neighbour spin states of a random lattice site are shown. The Metropolis algorithm uses single-spin-flip dynamics, the new state will have an energy E_2 differing from the previous energy E_1 by at most $2J$ for each bond between the spin flip and its neighbours.

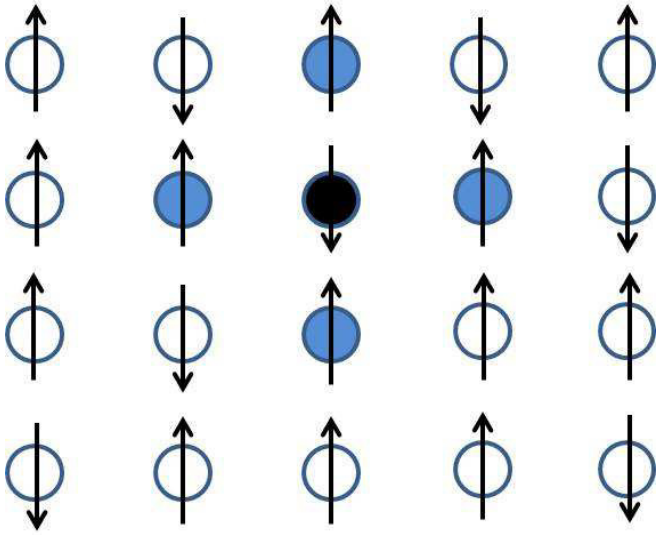


Figure 4.1: Two-dimensional 5x4 lattice (trial configuration).

4.5.2 Outline of Monte Carlo Code

The Monte Carlo code, which has been written in Fortran95 for the purpose of this thesis, allows one to investigate phase transitions in a two-dimensional square and three-dimensional cubic lattice. The Ising Hamiltonian has been implemented within the code.

Upon equilibration of the lattice, the code calculates thermal averages of macroscopic variables for an interacting lattice site system. The lattice configuration consists of +1 spin states also described as the $FM\ configuration$. This configuration is then randomized using the random number generator implemented within the code, which allows the program to randomly select a lattice site and perform the Metropolis algorithm.

Given the energy and magnetization of the Ising lattice at a selection of times during

the simulation, macroscopic variables such as the magnetic entropy S_{mag}, specific heat C_{mag} and susceptibilty χ_{mag} associated with the order parameter(s) can be obtained (see Appendix B for the relevant derivations).

A random number generator is a procedure that returns a different and apparently random number (pseudo-random number) each time it is called [148]. In such a procedure, the numbers are generated by a deterministic algorithm which must be reasonably complex to ensure that the numbers generated are random enough. The string of pseudo-random numbers produced is generally determined by a fixed number called a *seed*. It is vitally important to use implementations of a good standard random number generator, applicable to the system in question. In this work, the random number generator used produced a floating point number, which was uniformly distributed between 0 and 1.

Monte Carlo cycles are performed over a particular temperature range-specified in a user input file. This allows one to determine critical behaviour and identify discontinuities in the energy and its derivatives.

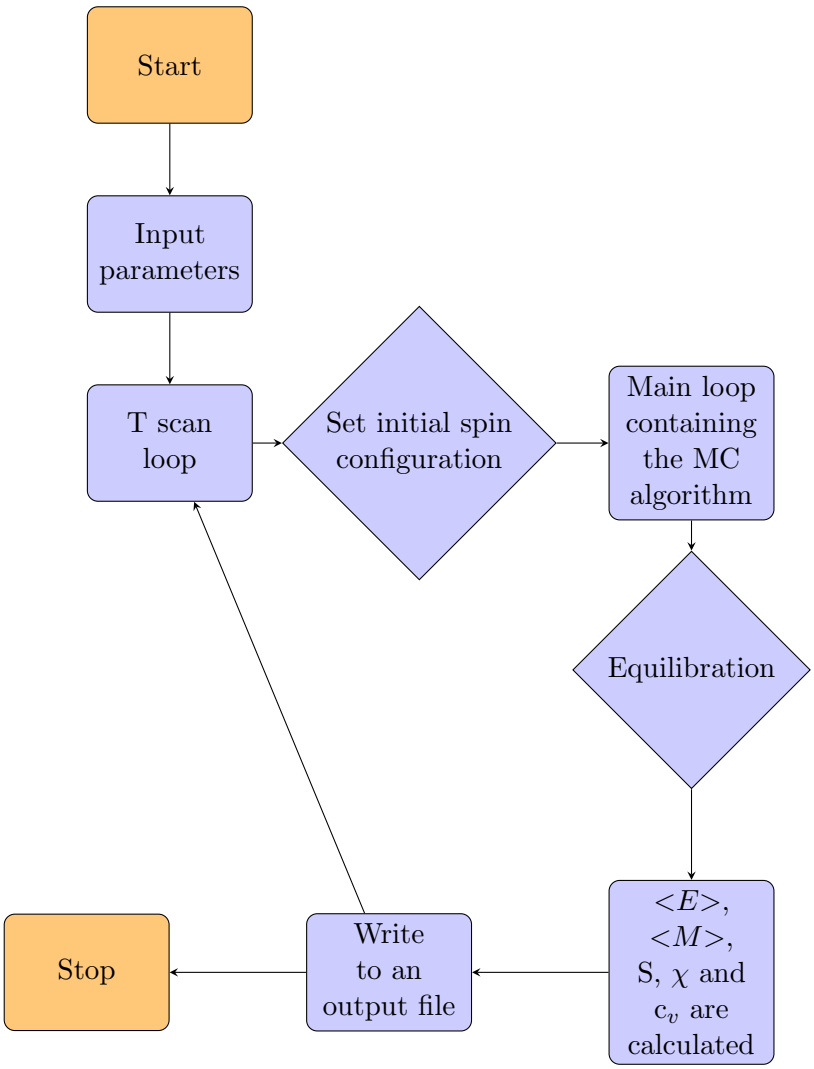


Figure 4.2: Flow chart showing the main components of the 3D Ising model Monte Carlo code. The input parameters correspond to the lattice size, number of Monte Carlo steps, number of equilibration steps, the initial and final temperature, and the temperature interval.

5

The End-point Stoichiometric Compounds: $LaMnO_3$ and $CaMnO_3$

In this chapter, the end-point compounds of the manganites series $La_{1-x}Ca_xMnO_3$, $LaMnO_3$ and $CaMnO_3$ are studied. A thorough understanding of the parent compound, $LaMnO_3$ is effectively a prerequisite to achieve a better understanding of the doped compounds. Since the ionic radii of La^{3+} (1.032Å) is larger than that of Ca^{2+} (1.000Å) [149], and the valency of the two ions differs, it is of primary importance to understand how their structural, bonding and electronic properties vary. In addition, this study is necessary to verify the accuracy of our computational methods with respect to available experimental data.

Previous calculations based on DFT within the local density approximation (LDA) for the cubic phase of $LaMnO_3$ fail to describe the insulating state, since the LDA excessively delocalises the electrons due to electronic self-interaction [150]. This approximation also underestimates the band gap for the ground state orthorhombic phase [151] and a qualitatively correct description of the orbitally ordered ground state is difficult to obtain [152]. Further, studies based on the generalised gradient approximation (GGA) of the exchange-correlation fail to predict the correct magnetic ground state [153, 154]. The band structure and insulating character of $LaMnO_3$ are described correctly qualitatively through the use of the Hartree-Fock (HF) method in its spin polarised (unrestricted Hartree Fock (UHF)) implementation [144, 155, 156]. However, the band gap is significantly overestimated due to the neglect of electron correlation. Moreover, physical properties such as the exchange constants are underestimated [156].

Other first principle studies [157, 158], for the end-point compounds, have focused on the LDA+U method. This approach treats the on-site Coulomb interactions in a mean-field approximation using semiempirical parameters and has been implemented as a correction to the local spin density approximation (LSDA) [159, 160]. Although this method significantly improves the description of the end-point compounds, it is not ideal since the electronic structure and energetics are highly dependent on the choice of the U parameter. Therefore, it is necessary to go beyond standard exchange-correlation potentials, which are limited in describing localised electronic states. This chapter of the thesis is, therefore, also concerned with providing a basis for validating the theory and numerical approximations, which are later used to study the effects of doping in $LaMnO_3$.

5.1 Orthorhombic $LaMnO_3$

At low temperatures, $LaMnO_3$ crystallises in the orthorhombic *Pnma* space group. The corresponding crystallographic cell is shown in Fig. 5.1, where each Mn ion is sixfold coordinated with O ions, forming octahedral cages that are linked by O ions. The orthorhombic structure comprises four formula units (20 atoms) where the MnO_6 octahedra are rotated and tilted. This is attributed to the relative sizes of the constituents and the facilitation of a more efficient space filling. The framework structure is susceptible to distortions, which may lower the symmetry of the structure.

5.1.1 Experimental Structure

Initially, single-point energy calculations were carried out at the *Pnma* experimental geometries determined by Dyakonov *et al.* [162] and Hauback *et al.* [163], which are given in Table 5.1. This is a necessary step to disentangle the effect of the geometry and the Hamiltonian. In the experimental studies considered, bulk polycrystalline samples were prepared using a standard solid-state reaction technique. Further, the crystallographic and magnetic structures were determined using neutron power diffraction measurements. The discrepancy between the geometries considered may be related to the synthesis conditions, as well as the oxygen content.

The energetics for the FM and A-AFM spin configurations (see Fig. 5.2) were computed and are reported in Table 5.1. Although the ground state for orthorhombic $LaMnO_3$ is AFM, B3LYP predicts that the FM state is 8.81meV/FU lower in energy. However, the prediction for the low temperature (9K) geometry is in agreement with

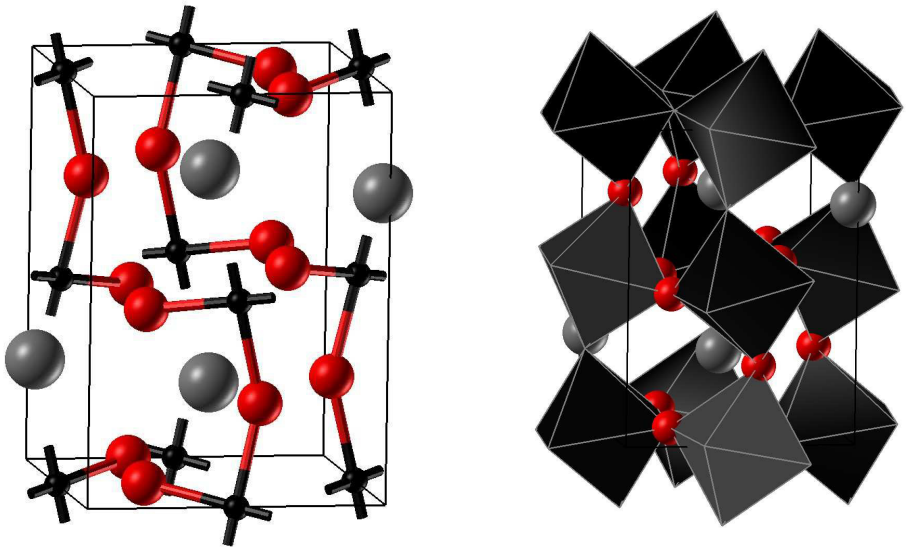


Figure 5.1: Crystallographic cell of *Pnma* $LaMnO_3$ for the optimized B3LYP geometry (left), where **b** is the longest lattice vector. The tilted and rotated MnO_6 octahedra (right). Large (grey), medium (red) and small (black) spheres correspond to the La, O and Mn atoms, respectively. Reproduced from Reference [161].

experiment. This provides strong evidence for a strong coupling between the structure and magnetism. The orthorhombic unit cell for the Dyakonov *et al.* geometry is 2.1% smaller than that of the Hauback *et al.* unit cell. Previous calculations using the GGA+U method have predicted that the FM and A-AFM states compete at low values of strain, particularly when the cell is compressed [164]. This may explain the FM ground state predicted for the Dyakonov *et al.* geometry in this work.

	a(Å)	**b** (Å)	**c**(Å)	V (Å^3)	T(K)	AFM ΔE (meV)	FM ΔE (meV)
Dyakonov *et al.* [162]	5.505	7.807	5.544	238.3	190	28.3	0.00
Hauback *et al.* [163]	5.730	7.672	5.536	243.4	9	0.00	8.81

Table 5.1: Experimental lattice parameters for $LaMnO_3$ (Dyakonov *et al.* and Hauback *et al.* geometries). The calculated energy difference with respect to the ground state for each geometry, ΔE is reported in meV per formula unit.

5.1.2 Optimized Structure

A full structure optimisation of the lattice parameters and internal coordinates was performed. The optimised and experimental lattice parameters of the ground state

(AFM (A)) and metastable magnetic structures are reported in Table 5.2. The collinear magnetic spin configurations, which are shown in Fig. 5.2, were generated by varying the initial conditions of the SCF solutions to the DFT equations. The calculated lattice parameters **b** and **c** are in good agreement with the experimental values; the percentage errors are 0.82% and 1.41%, respectively. The **a** lattice parameter is overestimated by 4.89%. However, there is no experimental certainty for this parameter, since values between 5.472Å and 5.748Å are reported [165]. In addition, $LaMnO_3$ shows oxidative nonstochiometry, which structurally implies excess oxygen/cation vacancies [166, 167]. Preceding experimental works have also reported on the sensitivity of the lattice vectors to the stoichiometry of the sample, which decrease with increasing oxygen content [163, 168]. Previous structural optimisations with different levels of theory (UHF and GGA) (given in Table 5.2) indicate a range of **a** values, which are inclined to the upper limit. The estimated thermal expansion of the experimental lattice parameters is 0.08%, between 9K and room temperature (RT) based on the data provided in Table 5.2. Therefore, the variation of the lattice parameters with temperature is considered to be negligible.

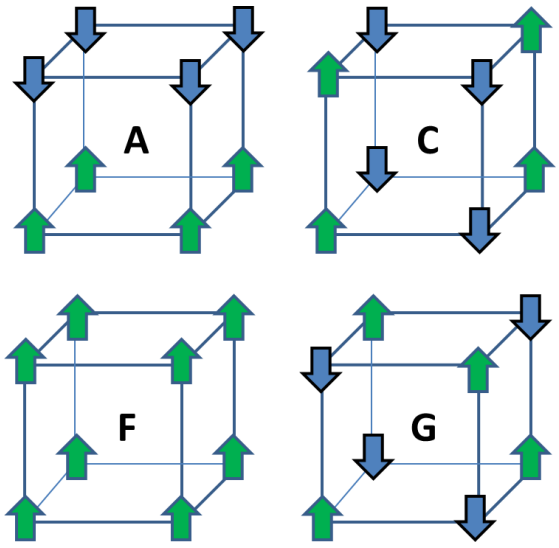


Figure 5.2: The A-, C-, F- and G- type collinear spin configurations considered, where the arrows indicate the ordering of Mn spin moments. Reproduced from Reference [161].

The general phenomenology of the $LaMnO_3$ electronic structure is provided by the

	MS	SC	**a**(Å)	**b** (Å)	**c**(Å)	V (Å^3)	ΔE (meV)	T(K)
		Opt.						
B3LYP	AFM (C)	↑↓↓↑	6.055	7.739	5.598	262.3	27.2	
B3LYP	AFM (G)	↑↓↑↓	6.076	7.713	5.600	262.4	22.7	
B3LYP	FM (F)	↑↑↑↑	5.995	7.758	5.613	261.1	5.1	
B3LYP	AFM (A)	↑↑↓↓	6.010	7.735	5.614	261.0	0.0	
			4.89%	*0.82%*	*1.41%*	*6.74%*		
UHF [156]	AFM (A)	↑↑↓↓	5.740	7.754	5.620	249.3		
GGA [153]	AFM (A)	↑↑↓↓	5.753	7.721	5.559	246.9		
		Exp.						
[169]	AFM (A)	↑↑↓↓	5.699	7.718	5.539	243.6		RT
[162]	AFM (A)	↑↑↓↓	5.505	7.807	5.544	238.3		190
[163]	AFM (A)	↑↑↓↓	5.730	7.672	5.536	243.4		9

Table 5.2: Optimized and experimental lattice parameters for $LaMnO_3$ for various magnetic structures (MS). In the fourth column, the arrows refer to the spin configuration (SC) of the four Mn atoms shown in Fig 5.1a). The percentage difference between the ground state magnetic structure and the corresponding low temperature experimental one (AFM (A) for $LaMnO_3$) is given in italics. The energy difference with respect to the ground state, ΔE is also reported in meV per formula unit.

ionic model. The Mn ions have a formal charge of 3+ and a $3d^4$ configuration. In the MnO_6 octahedron the Mn d-orbitals are split into triply degenerate t_{2g} and doubly degenerate e_g manifolds. The e_g degeneracy is lifted by a JT distortion of the MnO_6 octahedra, as is evident from the Mn-O bond lengths of $LaMnO_3$, reported in Table 5.3. There are two long (apical) and two pairs of shorter (equatorial) Mn-O bond lengths, due to the presence of JT distorted 3+ sites. The two longer equatorial bond lengths are directed along the **b** lattice vector. The optimized B3LYP bond lengths are comparable to the experimental bond lengths, determined from diffraction studies [170]. The apical bond lengths are over estimated by 6%, which is primarily attributed to the cooperative JT distortion in the simulated, perfectly stoichiometric and defect-free, structure.

Starting from the optimised structure, the effects of uniaxial strain have also been investigated to determine the implications of the overestimated **a** lattice vector on the Mn-O bond lengths. A full optimization (cell parameter(s) and atomic coordinates) was run in the presence of a constraint on the lattice parameters (a, b or c, respectively). The effect of a compressive and tensile uniaxial strain for **a**, **b** and **c**, on the apical and equatorial bond lengths, is shown in Fig. 5.3. The bond lengths are labelled in accordance with the optimised unstrained structure.

The apical bond lengths are in the plane defined by **a** and **c** and have a large component along **a**. The most significant effect on the apical bond lengths is due to a con-

Optimized Mn-O (Å)	Experimental Mn-O (Å)	N	% difference
1.919	1.91	2	0.47
1.986	1.96	2	1.32
2.310	2.18	2	5.96

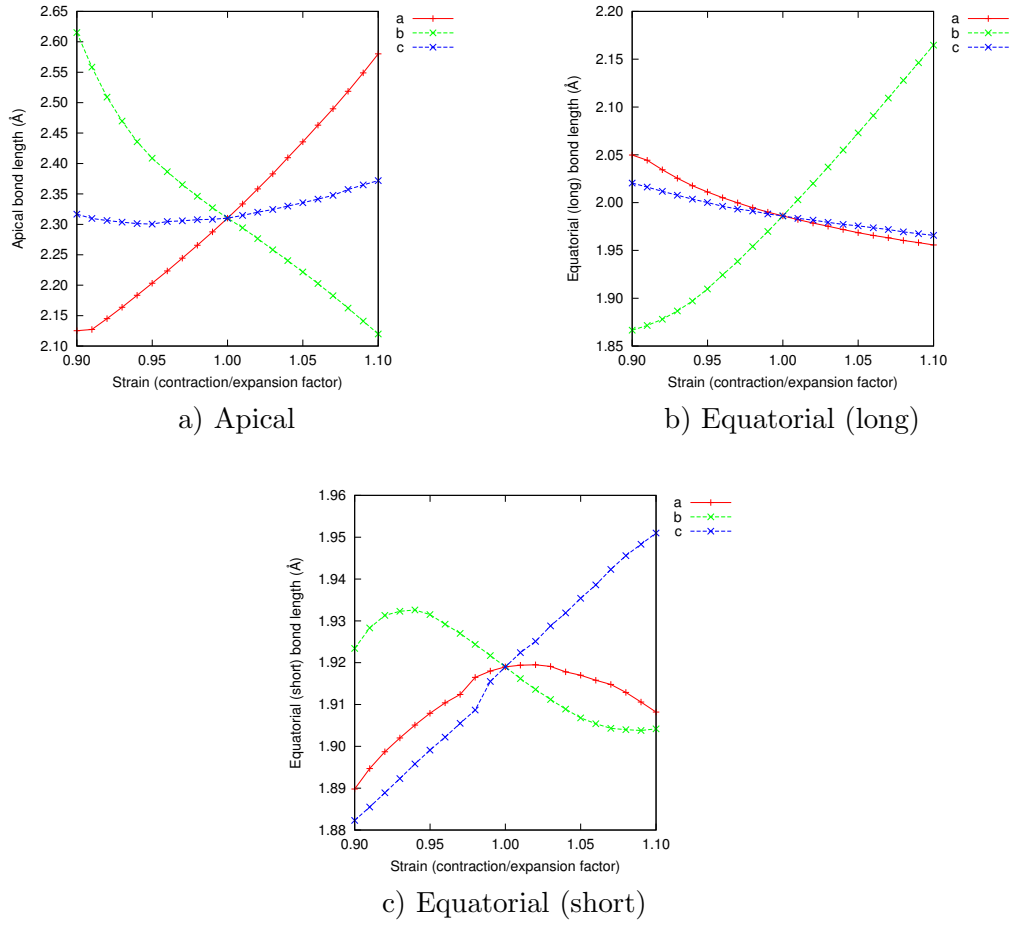
Table 5.3: Optimized and experimental Mn-O bond lengths for the $LaMnO_3$, where N is the number of neighbours. The experimental bond lengths have been calculated based on unit cell dimensions and atomic coordinates determined from powder neutron diffraction studies at 9K [163, 171]. The lattice vectors corresponding to the low temperature structure considered here are given in Table 5.2.

traction and expansion of the **a** lattice parameter, which is evident in Fig. 5.3. Hence, the discrepancy in the calculated apical bond lengths is related to the overestimated **a** lattice vector, for which there is also a considerable uncertainty in the measurement. In comparison, the two longer equatorial bond lengths are directed along the **b** lattice vector and therefore, the largest variation in these bond lengths is primarily due to a contraction and expansion of **b**. Since the calculated **b** lattice vector is in good agreement with the experimental **b**, there is not a discrepancy in the equatorial bond lengths as expected. The shorter equatorial bond lengths increase upon an expansion of **c** and a contraction of **b** (of up to 6%). Consequently, the initial short equatorial bond length becomes the *longer* one. There is a linear variation for a contraction of **a** and **c**, which have a relatively reduced effect when expanded.

5.1.3 Electronic Structure

The total spin polarised electronic density of states (DOS) for the $LaMnO_3$ ground state and metastable spin states are shown in Figure 5.4 with projections onto the La, Ca, Mn and O atoms. Zero energy corresponds to the Fermi level, so occupied and unoccupied states are characterised by negative and positive energies, respectively.

The observed A-type magnetic structure is 5.1meV below the FM case, as can be seen in Table 5.2. UHF calculations have predicted that the latter is the most stable phase for the cubic $LaMnO_3$ structure [156]. $LaMnO_3$ is predicted to be an insulator with a fundamental direct band gap of 3.22eV, which is larger than the reported experimental value of 1.1eV [172, 173] from optical measurements. The calculated indirect band gap of 2.66eV is evident in Figure 5.4a). Due to the AFM ordering of spins and the fact that optical transitions are spin conserving, it is difficult to assign an indirect gap from optical studies. However, a transport gap of 0.24eV has been estimated from resistivity measurements [174]. B3LYP typically overestimates optical band gaps in



a) Apical

b) Equatorial (long)

c) Equatorial (short)

Figure 5.3: The apical (a)) and equatorial optimised bond lengths (b) and c)), as a function of compressive and tensile uniaxial strain (**a**, **b** and **c**).

ionic systems due to inadequacy of the theory and also the neglect of excitonic binding. This discrepancy is, however, somewhat larger than expected and may be due to the effects of defects [166–168] on the optical spectrum. In previous theoretical work, the calculated band gap has been found to be sensitive to treatment of exchange and correlation [144].

The lower valence band DOS corresponding to the A-AFM electronic ground state is mainly attributed to the O $2p$ and Mn $3d$ bands, which hybridize, indicating partial covalency. The O $2p$ and Mn $3d$ bands have contributions of a similar magnitude to the DOS near the Fermi energy. These particular states also dominate the conduction band. The exchange splitting of the Mn $3d$ states is evident. In comparison, the FM state is metallic and the DOS states at the Fermi level are primarily attributed to the O

$2p$ and Mn $3d$ bands. In this case, hybridisation is found to be strongly spin dependent, since the majority Mn d and O p bands overlap, whilst the minority Mn d and O p bands are separated by a gap. The G- and C-type states are both insulators, and the former exhibits the largest indirect band gap amongst the ground and metastable state(s).

The calculated net atomic charges and magnetic moments for the C-, G- and F-type magnetic structures are given in Table 5.4. Since the the e_g orbital is singly occupied, the Mn magnetic moment is expected to be $4\mu_B$ in accordance with Hund's rule. However, due to the hybridisation of the O $2p$ and Mn $3d$ bands (shown in Fig.5.4a)), the magnetic moment is $3.81\mu_B$/FU for the ground state. This is comparable to $3.42\mu_B$, which has been determined from neutron diffraction measurements [163].

MS	q_{Mn}	$q_{O(9-12)}$	$q_{O(13-20)}$	μ_{Mn}
AFM (A)	1.824	-1.281	-1.303	3.812
AFM (C)	1.824	-1.282	-1.303	3.778
AFM (G)	1.822	-1.279	-1.303	3.757
FM	1.826	-1.284	-1.302	3.832

Table 5.4: The net atomic charges q=Z(n_α+n_β) in units of electrons and spin moments μ=(n_α+n_β) in units of μ_B/FU obtained from the Mulliken population analysis for the optimised $LaMnO_3$ structure.

5.1.4 Magnetic Ordering and Phases

The determined ground state magnetic structure is the A-type antiferromagnet, as can be seen in Table 5.2. This is in agreement with previous studies [162, 163, 169]. The A-type ordering of spins consists of ferromagnetic MnO_2 planes coupled antiferromagnetically along the **b** axis. Antiferromagnetic coupling is observed when adjacent Mn e_g orbitals have the same orientation. In Fig. 5.5, the spin density plot for the ground state A-AFM phase is shown. The in-plane polarisation of the O-$2p$ orbitals by the Mn-$3d$ is evident, this is expected to affect exchange coupling mechanism. In contrast, the polarisation along **b** is significantly reduced. An asymmetry in the oxygen spin density is clear.

The broken symmetry Kohn-Sham approach is used [175, 176] to study the magnetic order and to determine the nearest-neighbour superexchange coupling constant J, which is positive for FM and negative for AFM interactions. The coupling constant has been obtained from $\Delta E = E^{AFM} - E^{FM}$, the difference of total energies of the FM and AFM structures (given in Table 5.2), which is proportional to J and is given

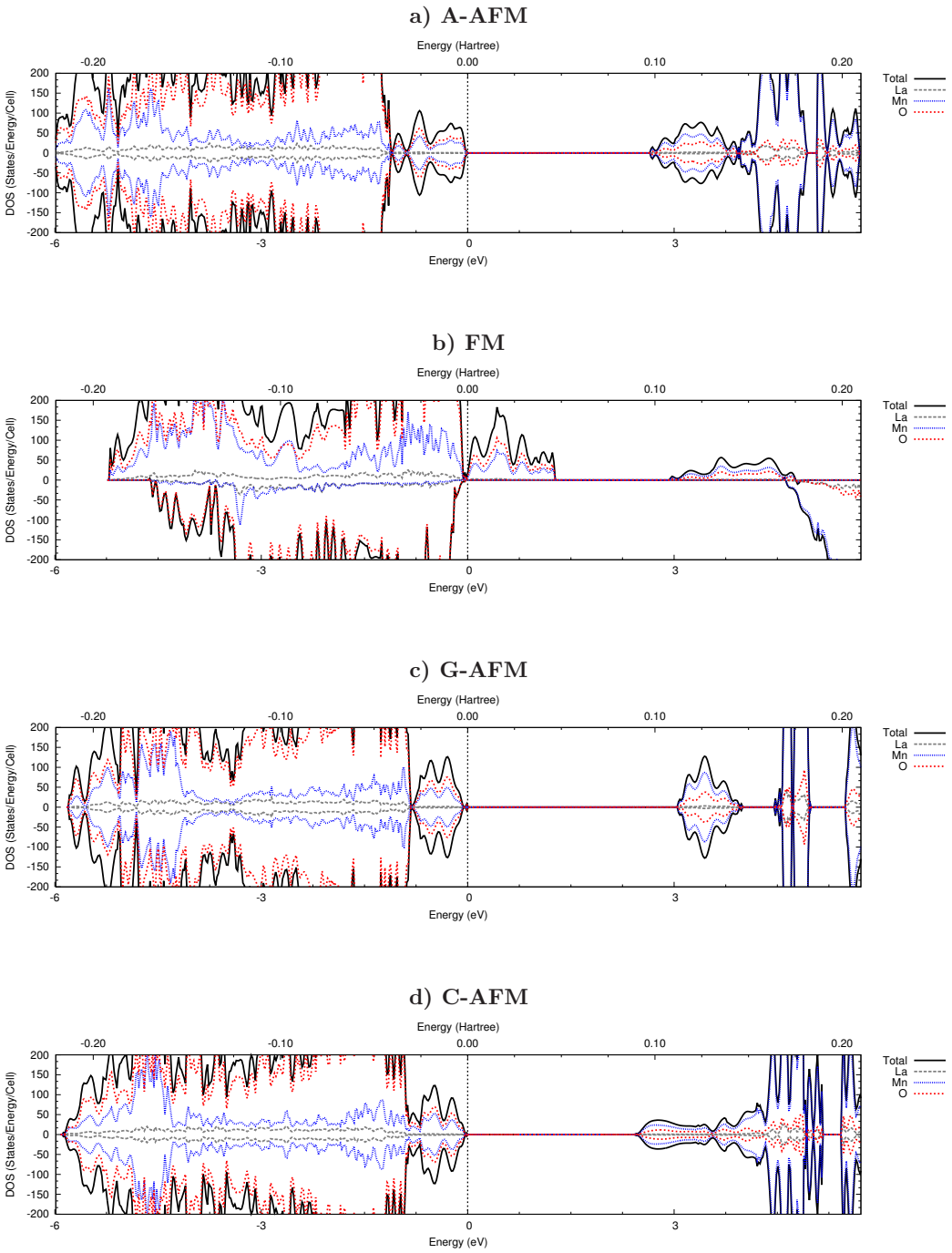


Figure 5.4: Total density of states for $LaMnO_3$ with projections on the La, Mn and O atoms; the Fermi level is at 0eV. Reproduced from Reference [161].

by $\Delta E = N \cdot Z \cdot J \cdot S_z S'_z$ where N is the number of symmetric Mn atoms in the ferromagnetic cell, Z is the number of the next nearest (Mn) neighbours to each of the N Mn with opposite spin, $S_z S'_z$ is the product of the z component of neighbouring Mn spin moments, according to the Ising Hamiltonian. One of the assumptions of the nearest-neighbour Ising model is that the magnitude of the spin does not depend on the magnetic order. These calculations assume a homogeneous MnO_6 octahedron, J_{eq} and J_{ap} are calculated, where J_{eq} is the magnetic coupling along the direction defined by the equatorial Mn-O bond and J_{ap} is the magnetic coupling constant along the direction defined by the apical Mn-O bond. Since a $3d^4$ configuration is considered, the value of S_z is $4\mu_B$/Mn. The mapping of the DFT energetics to the superexchange model and the detailed derivations for J_{eq} and J_{ap} are given in Appendix C.

The calculated J_{eq} and J_{ap} coupling constants are 1.38mev and -0.64meV, respectively. Thus, the magnetic ordering in the plane, in which the apical bond lengths lie, is AFM but weak. The magnitude of exchange coupling constants obtained from these calculations are larger than those obtained from neutron-scattering measurements, where the spin wave modes have been calculated using an anisotropic three-dimensional Heisenberg Hamiltonian including a single ion anisotropy term. The values for J_1 and J_2 were determined to be 0.83meV and -0.58meV, where J_1 is defined as a distinct exchange constant in the basal plane ab (FM exchange integral) and J_2 an exchange constant in the adjacent MnO_2 planes along **c** (AFM exchange integral) [177]. The J_{eq} calculated here is larger by a factor of 2 than J_{ap}. In comparison, this factor is around 1.4 for the FM and AFM coupling constants determined from neutron-scattering measurements.

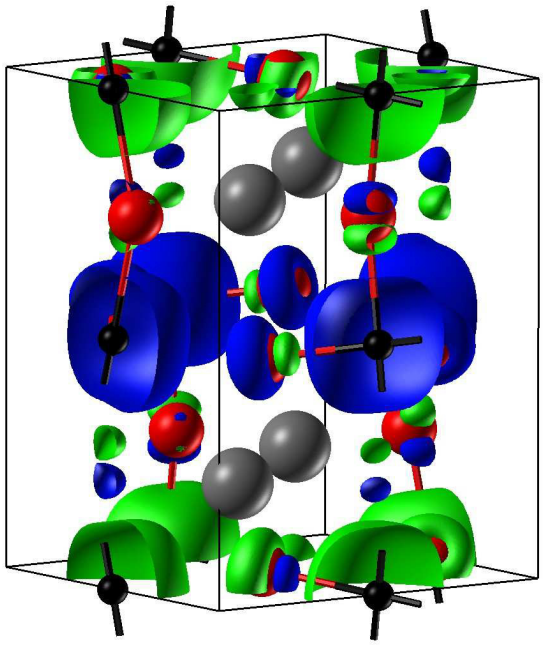


Figure 5.5: Isovalue surfaces of the calculated spin density for A-AFM $LaMnO_3$ where, the spin isosurface values are as follows: green is 0.005 (spin up) and blue is -0.005 (spin down) in units of |e|/bohr^3. Reproduced from Reference [161].

5.2 Orthorhombic $CaMnO_3$

$CaMnO_3$ has essentially the same structure as the parent compound, $LaMnO_3$ and therefore, also forms in the *Pnma* orthorhombic perovskite structure. However, the ionic radius mismatch between La^{3+} and Ca^{2+} leads to a contraction in all lattice dimensions (**a**, **b** and **c**) for $CaMnO_3$. The corresponding crystallographic cell for the optimsed B3LYP geometry is shown in Fig. 5.6. The Mn ions are also sixfold coordinated with oxygen ions to form a MnO_6 octahedron. The Ca ion is situated within the gaps between the corner sharing MnO_6 octahedra and is surrounded by 12 O ions.

5.2.1 Optimized Structure

The optimized cell parameters for $CaMnO_3$ are given in Table 5.5, and are in good agreement with the cited low temperature (10K) *Pnma* experimental phase determined by neutron powder diffraction. The percentage errors are all within 1% of the experimental values. In the previous section, it has been established that the effect of temperature on the lattice parameters of $LaMnO_3$ is insignificant. In comparison, the

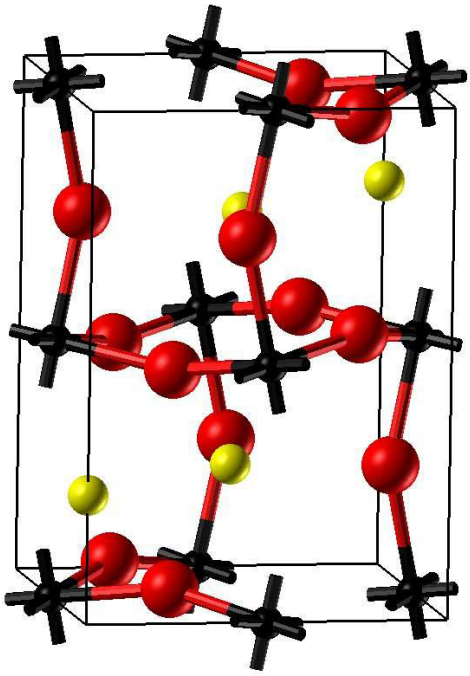


Figure 5.6: Crystallographic cell of *Pnma* $CaMnO_3$ for the optimised B3LYP geometry, where **b** is the longest lattice vector (left). Large (red), medium (yellow) and small (black) spheres correspond to the O, Ca and Mn atoms, respectively. Reproduced from Reference [161].

thermal expansion of $CaMnO_3$ in the temperature range 10K to RT, is estimated to be 0.34% from the data listed in Table 5.5.

In $CaMnO_3$, the Mn ions have a formal charge of 4+ with a $3d^3$ configuration, which is also provided by the ionic model. The Mn-O bond lengths are homogeneous, when compared to those of $LaMnO_3$, since the octahedra are not JT distorted. There is a good agreement with the experimental bond lengths obtained from diffraction studies [163], which are shown in Table 5.6. The percentage errors are all within 1% of the experimental values.

5.2.2 Electronic Structure

The electronic density of states for the $CaMnO_3$ ground state (AFM (G)) and metastable states, with projections on the Ca, Mn and O atoms are shown in Fig. 5.7.

	MS	SC	**a**(Å)	**b** (Å)	**c**(Å)	V (Å^3)	ΔE (meV)	T(K)
		Opt.						
B3LYP	FM (F)	↑↑↑↑	5.319	7.515	5.328	213.0	31.3	
B3LYP	AFM (A)	↑↑↓↓	5.318	7.495	5.332	212.5	11.7	
B3LYP	AFM (C)	↑↓↓↑	5.298	7.519	5.328	212.2	3.4	
B3LYP	AFM (G)	↑↓↑↓	5.302	7.505	5.330	212.1	0.0	
		Exp.						
[171]	AFM (G)	↑↓↑↓	5.279	7.448	5.264	207.0		RT
[178]	AFM (G)	↑↓↑↓	5.276	7.440	5.256	206.3		10

Table 5.5: Optimized and experimental lattice parameters for $CaMnO_3$ for various magnetic structures (MS). In the fourth column, the arrows refer to the spin configuration (SC) of the four Mn atoms shown in Fig 5.6a). The percentage difference between the ground state magnetic structure and the corresponding low temperature experimental one (AFM (G) for $CaMnO_3$) is given in italics. The energy difference with respect to the ground state, ΔE is also reported in meV per formula unit.

Optimized Mn-O (Å)	Experimental Mn-O (Å)	N	% difference
1.916	1.90	2	0.84
1.917	1.90	2	0.89
1.919	1.90	2	0.99

Table 5.6: Optimized and experimental Mn-O bond lengths for $CaMnO_3$, where N is the number of neighbors. The experimental bond lengths have been calculated based on unit cell dimensions and atomic coordinates determined from powder neutron diffraction studies at 9K [163,171]. The lattice vectors corresponding to the low temperature structure considered here are given in Table 5.5.

The calculated band gap for $CaMnO_3$ of 2.35eV is comparable with the value of 3.1eV [173] deduced from frequency dependent optical-conductivity spectra. The ground state (Fig. 5.7a)) lower valence band DOS is attributed to the O $2p$ bands with minor contributions from other Mn and Ca states. The conduction band is dominated by O $2p$ and Mn $3d$ bands. $CaMnO_3$ is also an insulator, since the JT-split Mn($3d$)$e_g{}^1$ is depleted for x=1. Further, the bonding has a significant ionic component, since the hybridization of the O $2p$ and Mn $3d$ states is less significant when compared to $LaMnO_3$. The FM state is also insulating, as can be seen in Fig. 5.7b). If we then analyse the spin quantities, the spin moment on the Mn for the G-type spin configuration is $2.85\mu_B$. This value is close to the d^3 configuration expected for a completely ionic system.

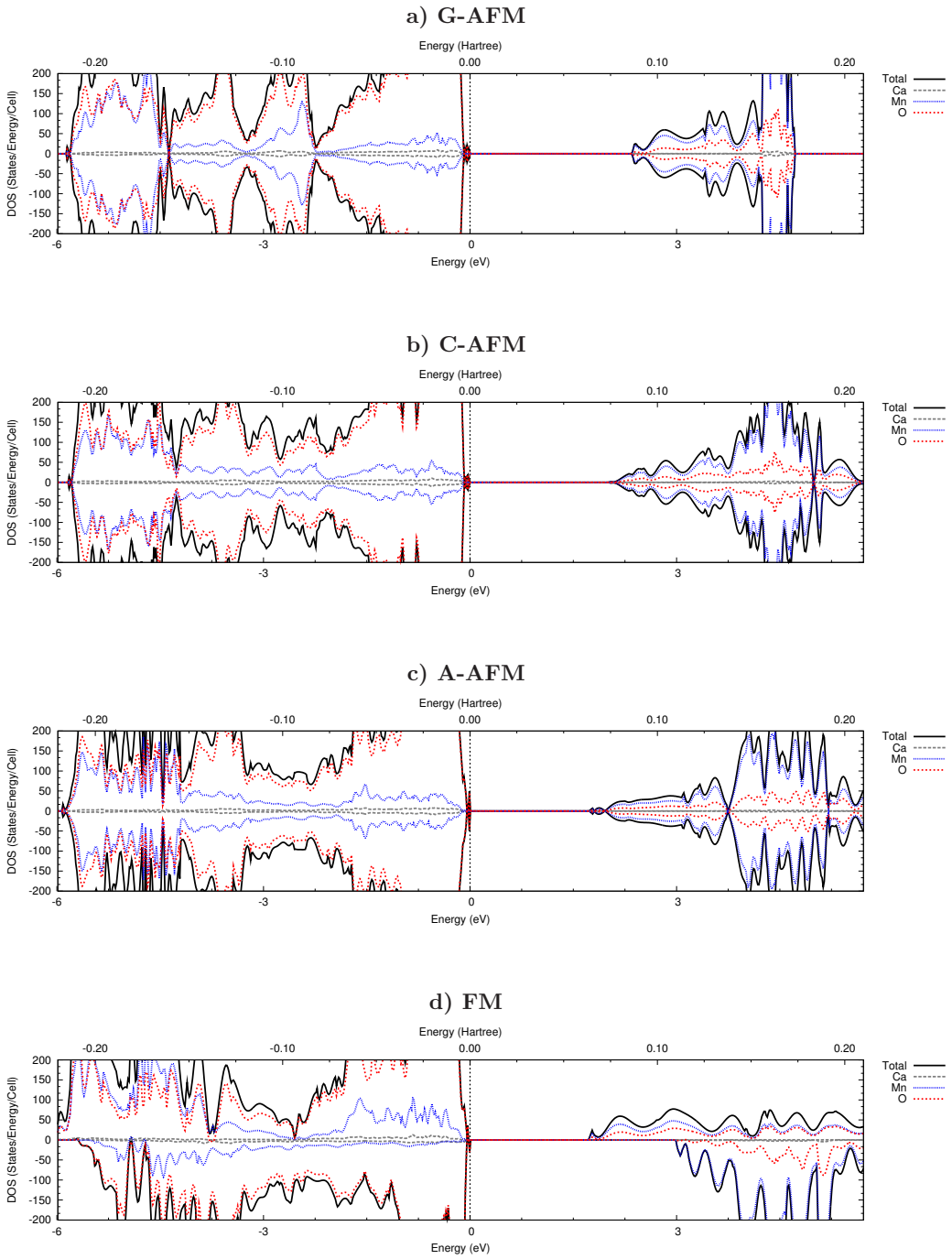


Figure 5.7: Total density of states for $CaMnO_3$ with projections on the Ca, Mn and O atoms; the Fermi level is at 0eV. Reproduced from Reference [161].

5.2.3 Magnetic Ordering and Phases

At the optimised $CaMnO_3$ geometry, the ground state is AFM, Table 5.5 indicates that the lowest energy magnetic structure is G-type, where the Mn are coupled antiferromagnetically in all crystallographic directions. Thus, B3LYP predicts the correct ground state [179]. The difference between the C- and G-type magnetic structures is 3.5meV, which is particularly small.

The isovalue surface of the spin density for the ground state G-AFM phase is shown in Fig. 5.8. It can be see that the polarisation of the O-2p orbitals is significantly reduced, when compared to $LaMnO_3$. However, the in-plane polarisation and the polarisation along **b** is of a similar magnitude. Hence, the exchange coupling mechanism is expected to be the same in both directions. The energy differences between the ground and metastable states in Table 5.5 have been used to compute J_{eq} and J_{ap} coupling constants. The methodology implemented in section 5.1 to compute such quantities is also used here. Subsequently, the calculated values for J_{eq} and J_{ap} are -3.09meV and -4.36meV, respectively.

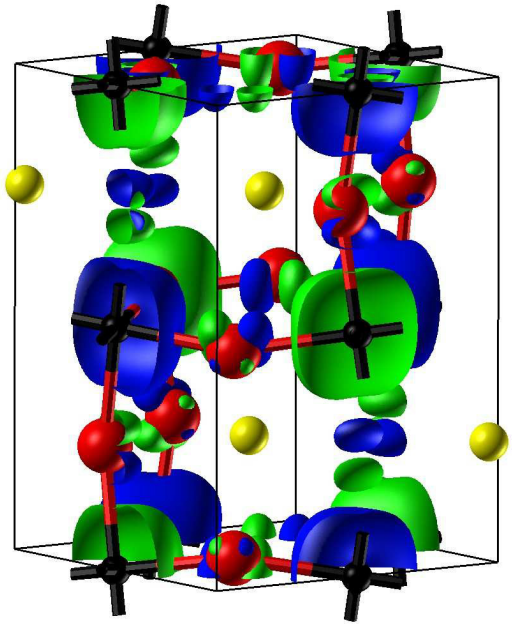


Figure 5.8: Isovalue surfaces of the calculated spin density for G-AFM $CaMnO_3$ where, the spin isosurface values are as follows: green is 0.005 (spin up) and blue is -0.005 (spin down); in units of |e|/bohr^3. Reproduced from Reference [161].

5.3 Summary

In this chapter a detailed investigation into the the very different structural and magnetic symmetries of the orthorhombic end-point compounds, $LaMnO_3$ and $CaMnO_3$, using hybrid-exchange density functional theory has been presented. The most stable phases, A-AFM for $LaMnO_3$ and G-AFM for $CaMnO_3$, have been predicted correctly. The existence of Mn^{3+} JT ions in $LaMnO_3$, results in strongly distorted MnO_6 octahedra, which are not present in $CaMnO_3$. The O $2p$ and Mn $3d$ states are responsible for the energy bands near the Fermi level, which contribute to the electronic properties for $LaMnO_3$ and $CaMnO_3$. There is a strong hybridization of the O $2p$ and Mn $3d$ bands in $LaMnO_3$, indicating semi-covalency. Moreover, this investigation indicates that the coupling between the Mn ions plays an active role in the resultant magnetic behaviour. A strong interplay between the crystalline distortions, electronic structure and magnetic orderings is evident. This chapter demonstrates the reliability of the description of the hybrid B3LYP functional for an investigation of the effects of doping in the manganite series, $La_{1-x}Ca_xMnO_3$.

6

The Effects of Doping in $La_{1-x}Ca_xMnO_3$, where x=1/4

The rich diversity in crystallographic, magnetic and electronic phases [11–13] displayed by Ca-doped manganites can be seen in Fig. 6.1. Early attempts to explain the electronic structure and magnetic properties of mixed-valency manganites were made by Zener [33, 34], who proposed that the low temperature FM-M phase for the $La_{1-x}Ca_xMnO_3$ series is attributed to the double-exchange (DE) mechanism. Zener's DE model involves spin coupling between Mn^{3+} and Mn^{4+} next-nearest-neighbour ions with the conduction electrons mediating the interaction. However, the DE model yields a T_C higher, by an order of magnitude, than that determined experimentally [67, 180]. It has been proposed [180, 181] that this discrepancy is due to the neglect of electron-lattice interactions in the DE model. The effective Debye-Waller factors of Mn-O pairs and the pair distribution function of local bond lengths (determined experimentally using extended X-ray fine absorption structure (EXAFS) and neutron powder-diffraction data) indicate distortions of the MnO_6 octahedron [88, 182–185]. Such experiments support the view that strong hole-lattice coupling is important. Understanding the transition from a low temperature, metallic, magnetically ordered regime to a high-temperature polaron-dominated and magnetically disordered regime requires a theory capable of describing the localised electronic state polaron and the strongly correlated metal. This is a major challenge for the theory of electronic structure in condensed matter.

The reliability of the hybrid-exchange functional B3LYP in describing the structural and electronic properties of manganites has been established in the previous chapter. An insight into the relevant energy scales, which contribute to the stability of the doped

compound, $La_{0.75}Ca_{0.25}MnO_3$ is provided in this chapter. We focus our attention on the interplay between a hole and local lattice distortion, to understand the relationship between the transport and structural properties. The competing interactions are disentangled and quantified to determine their implications on the magnetocaloric effect for this composition.

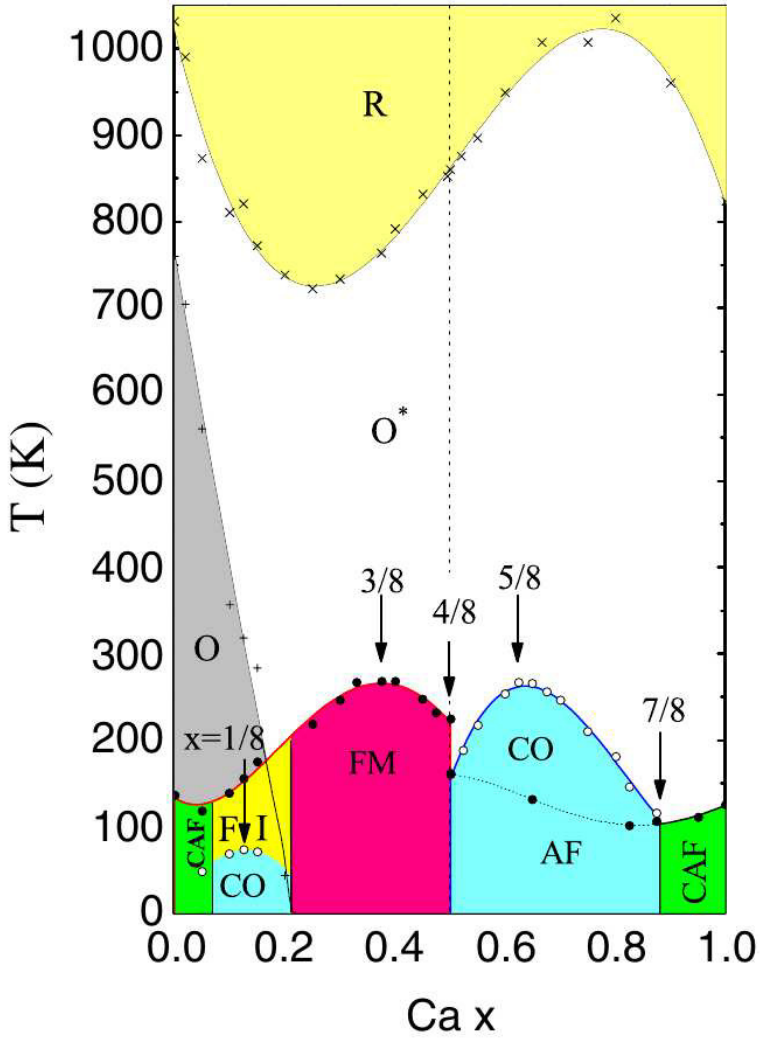


Figure 6.1: The $La_{1-x}Ca_xMnO_3$ phase diagram, where CAF=canted antiferromagnet, CO=charge ordered insulator, FI=ferromagnetic insulator, FM=ferromagnetic metal, AF=antiferromagnet, O*=paramagnetic insulating phase with no long-range JT order, from Ref. [186] with permission. © IOP Publishing & Deutsche Physikalische Gesellschaft. CC BY-NC-SA

6.1 Optimized Structure of $La_{0.75}Ca_{0.25}MnO_3$

The refined structural parameters from neutron-powder diffraction data for $La_{0.75}Ca_{0.25}MnO_3$ at 20K are shown in Table 6.1. Since the data has been fitted with structure factors based on a partial occupation of Ca sites, it is evident that the distribution of Ca is substitutionally disordered [187]. In our calculations, the disordered structure of $La_{0.75}Ca_{0.25}MnO_3$ has been approximated by an ordered Ca distribution; where a La atom has been replaced by a Ca atom in the unit cell of $LaMnO_3$, which contains four formula units. The optimised orthorhombic *Pnma* perovskite structure of $La_{0.75}Ca_{0.25}MnO_3$ is shown Fig. 6.2.

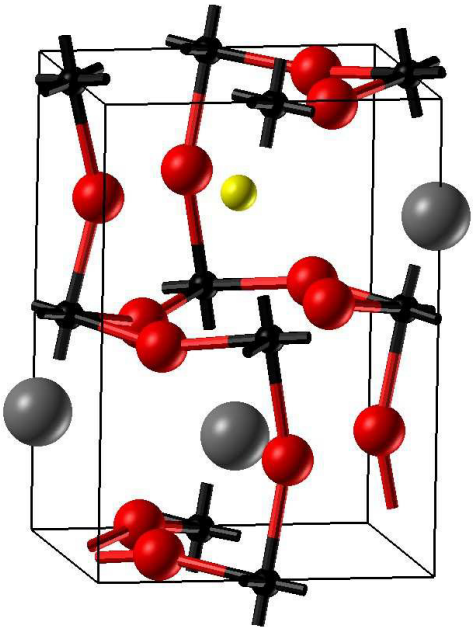


Figure 6.2: Crystallographic cell for the ordered lattice approximation to the substitutionally disordered $La_{3/4}Ca_{1/4}MnO_3$, where La-grey, O-red, Mn-black Ca-yellow and **b** is the longest lattice vector.

6.2 Where does the hole go?

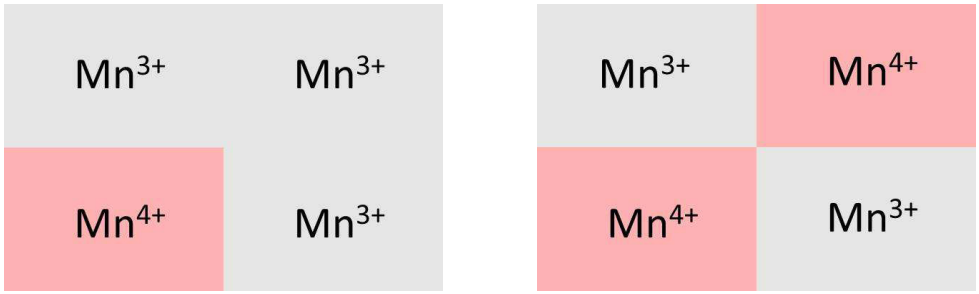
When a La^{3+} is replaced by a Ca^{2+}, the unit cell is essentially doped with a hole. In an ionic model, the nominal hole concentration in the O p-band for $La_{0.75}Ca_{0.25}MnO_3$ is n=1/4. The doped hole may delocalize in the O 2p-band or localize on an O site. On the other hand, a solution in which the hole delocalises in the Mn bands, or localises on a particular Mn is also viable. If the DOS for $LaMnO_3$ is considered, the upper valence band is a mixture of O and Mn states. Consequently, even in a rigid band model, the ground state for $La_{0.75}Ca_{0.25}MnO_3$ is not clear *a priori*.

Generally, by varying the initial density matrix, it is possible to converge various solutions in strongly correlated systems. The calculations with a delocalised hole in the O 2p-band do not converge to a stable solution herein. Thus, the electronic structures and energetics of the following stable solutions, which were found (depicted in Fig. 6.3), are compared: (1) the localization of the hole on a particular Mn ion with a consequent change in the oxidation state (from Mn^{3+} to Mn^{4+}) and (2) the delocalisation of the hole over two Mn ions.

a	(Å)	5.47057(3)
b	(Å)	7.73374(4)
c	(Å)	5.48853(3)
V	(Å^3)	232.208(2)
μ_z	(μ_B)	3.51(1)
Mn	u_{iso}(Å^2)	0.0003(2)
La/Ca	x	0.0213(1)
	z	-0.0043(1)
	u_{iso}(Å^2)	0.0023(1)
O(1)	x	0.4918(2)
	z	0.0640(1)
	u_{11}(Å^2)	0.0063(5)
	u_{22}(Å^2)	0.0012(4)
	u_{33}(Å^2)	0.0031(3)
	u_{13}(Å^2)	0.0004(3)
O(2)	x	0.2760(1)
	y	0.03323(6)
	z	0.72543(9)
	u_{11}(Å^2)	0.0035(2)
	u_{22}(Å^2)	0.0039(2)
	u_{33}(Å^2)	0.0032(2)
	u_{12}(Å^2)	0.00006(3)
	u_{13}(Å^2)	-0.0009(2)
	u_{23}(Å^2)	0.0007(3)

Table 6.1: Refined structural parameters from neutron powder-diffraction data for $La_{0.75}Ca_{0.25}MnO_3$ at 20K [187]. The space group symmetry is *Pnma* (No. 62) and the numbers in parenthesis are statistical errors of the last significant digit.

The lattice parameters for the calculated ground state, metastable state and the experimental geometry are given in Table 6.2. In the predicted ground state, a hole localises on a particular Mn. However, a deviation from the orthorhombic symmetry is evident, particularly in the angle β. This deviation is attributed to the ordered distribution of Ca imposed in the calculation, which leads to a cooperative distortion in the periodic structure. Such a distortion is not favoured in the observed material, which is substitutionally disordered.



a) Localised b) Delocalised

Figure 6.3: The stable states for $La_{0.75}Ca_{0.25}MnO_3$, where a) represents the localisation of the hole on a particular Mn and b) shows the delocalisation of the hole over two Mn in the unit cell.

	ΔE (meV)	**a**(Å)	**b** (Å)	**c**(Å)	α (°)	β (°)	γ (°)	V (Å^3)
D	45.8	5.635	7.812	5.569	90.0	87.8	90.0	244.8
L	0.00	5.622	7.842	5.559	90.3	89.4	90.0	245.1
Exp. [187]		5.470	7.734	5.489	90.0	90.0	90.0	232.2
		2.70%	*1.38%*	*1.26%*				

Table 6.2: Optimized and experimental [187] lattice parameters for the $La_{0.75}Ca_{0.25}MnO_3$ delocalised (L) and localised (D) hole solutions. The relative energy of the metastable state (delocalised hole) with respect to the ground state (localised hole) is also given. The percentage difference between the calculated ground state lattice vectors and the corresponding experimental ones is given in italics.

6.3 Formation of an Anti-JT Polaron

The electronic structure of $La_{1-x}Ca_xMnO_3$ is analysed with reference to the DOS for the metastable and ground state, which are shown in Fig. 6.4. Zero energy corresponds to the Fermi level, so occupied and unoccupied states are characterised by negative and positive energies, respectively. The minimum energy magnetic ordering for both states is FM. It is clear that there is a finite density of states at the Fermi level for the majority spin states and a gap in the minority spin states, in Fig. 6.4a). Hence, the delocalisation of the hole leads to a half-metallic state. The hybridization of the Mn d and O p majority spin states, above and below E_f, is evident. In comparison, the localisation of the hole on a particular Mn results in an insulating state, with a spin resolved band gap of 2.02eV in the majority and 4.22eV in the minority spin states (see Fig. 6.4b)). Therefore, the ground state comprises a FM insulator (FM-I) and the FM

metal (FM-M) is a metastable state.

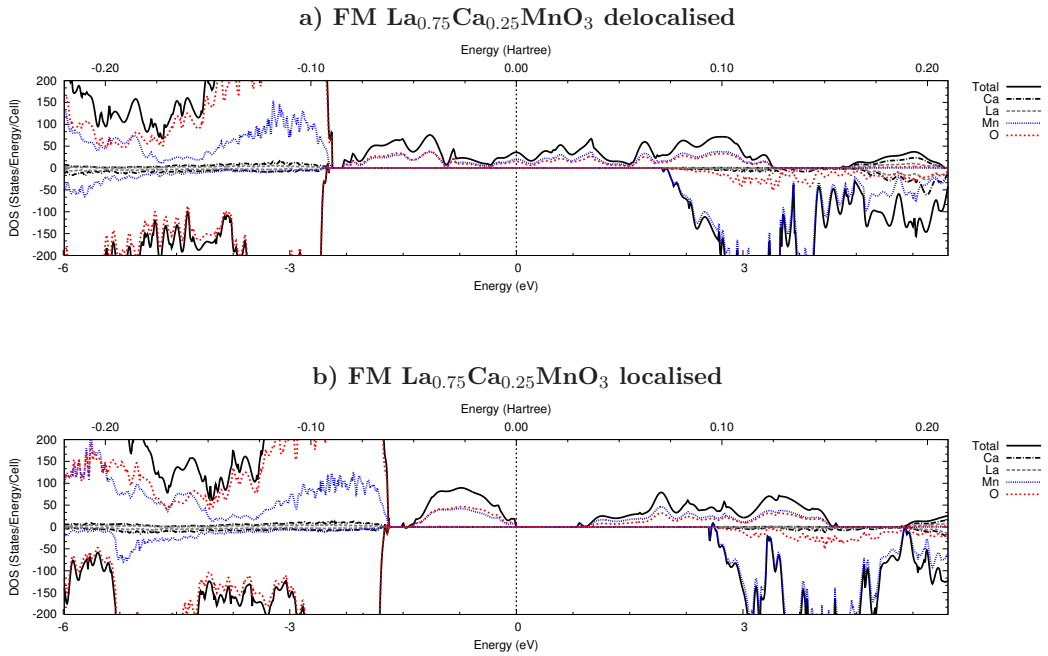


Figure 6.4: Total density of states with projections on the Ca, La, Mn and O atoms; the Fermi level is at 0eV.

A local distortion of the lattice is expected due to the difference in ionic radii between La^{3+} (1.032Å) and Ca^{2+} (1.000Å) [149] but also due to the difference between Mn^{3+} (0.645Å) and Mn^{4+} (0.530Å) [149]. The latter is attributed to the localisation of the hole on a particular Mn.

The optimised nearest neighbour bond lengths for the FM-M and FM-I are given in Table 6.3. It is evident that a distortion of the geometry occurs when the hole localizes. In the insulating state, it can be seen that the JT distortion of the MnO_6 octahedron associated with Mn(3) is lifted, since the bond lengths are more homogeneous when compared to those of the Mn(1), Mn(2) and Mn(4) centered octahedra in the unit cell. This is attributed to the localised hole, which induces an anti-polaronic distortion. The local 'undoing' of the JT distortion, lowers the electron-phonon energy and traps the hole in a small polaron state, thus restoring higher symmetry around the hole. In particular, this observation is in agreement with neutron diffraction experiments, where the local JT distortion in the insulating phase for $LaMnO_3$ decreases continuously with increasing Ca content [188]. The formation of an anti-JT polaron, in which the degenerate e_g orbital is not occupied provides direct evidence of a very strong charge-

lattice interaction.

Mn	Metal Mn-O (Å)	Insulator Mn-O (Å)
1	1.933	1.885
	1.954	1.903
	1.954	2.043
	2.018	2.114
	2.172	2.125
	2.209	2.146
2	1.914	1.907
	1.929	1.919
	1.967	2.042
	2.006	2.091
	2.026	2.103
	2.027	2.122
3	1.914	**1.914**
	1.929	**1.928**
	1.967	**1.939**
	2.006	**1.940**
	2.026	**1.962**
	2.027	**1.973**
4	1.933	1.880
	1.954	1.938
	1.954	2.047
	2.018	2.071
	2.172	2.114
	2.209	2.141

Table 6.3: Optimized Mn-O bond lengths for the $La_{0.75}Ca_{0.25}MnO_3$ unit cell in the FM-I and FM-M states. The Mn-O bond lengths corresponding to the Mn^{4+} are highlighted in bold.

6.4 Magnetic Ordering

The isovalue surface of the calculated spin density for the ground state $La_{0.75}Ca_{0.25}MnO_3$ phase is shown in Fig. 6.5. It is evident that there is a transition from the A-AFM structure in $LaMnO_3$, which is shown in the previous chapter, to FM ordering in $La_{0.75}Ca_{0.25}MnO_3$. This is attributed to the ionic radii of Ca^{2+} being 3.1% smaller than that of La^{3+} but also due to the lattice-hole interaction, which modifies the MnO_6 octahedra. A significant polarisation of the O-2p orbitals by the Mn-3d states is clear, which is expected to modify the exchange coupling mechanism.

The orbitally ordered structure is evident and the spin density distribution of the O atoms has the distinct shape of a d_{z^2} atomic orbital.

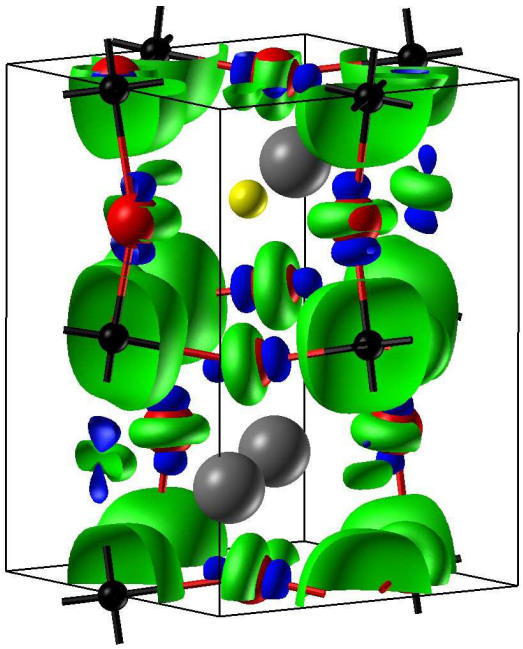


Figure 6.5: Isovalue surfaces of the calculated spin density for FM $La_{0.75}Ca_{0.25}MnO_3$ where, the spin isosurface values are as follows: green is 0.005 (spin up) and blue is -0.005 (spin down); in units of |e|/bohr^3.

6.5 Energetics

The energetics related to the hole conductivity, doping site, spin ordering and also the exchange coupling mechanism are disentangled and quantified in this section.

6.5.1 Hopping Barrier

If a conductivity model is considered where a localised hole is thermally activated to a conducting state over an energy barrier, which is also referred to as the hopping barrier herein, then a $\Delta E_{hopping}$ of 46meV (per formula unit) is required to delocalise the hole with respect to the FM-I ground state. Since $\Delta E_{hopping} > kT(\sim 26meV)$, it is expected that the hole would not delocalise at RT.

6.5.2 Doping Site Dependence

In $LaMnO_3$, the La sites are all equivalent. However, the localisation of the hole in $La_{0.75}Ca_{0.25}MnO_3$ removes the symmetry between the La sites. Consequently, there is a dependence of the energetics on the dopant site, which is shown in Fig. 6.6. In addition to this energy scale, there is also a dependence on the hopping barrier, which can be deduced from Fig. 6.6. The hopping barrier is much larger than the energy variation with the site of the dopant, which is ∼6-12meV.

It is evident that the energetically more favourable state is the one in which the Ca is doped at site 2 and the hole localises. This could be understood by analysing the Ca-Mn bond distances, which are given in Table 6.4. The spin resolved band gap for each state is also given, which increases by 0.02eV from the lower energy (Ca sites (2) and (3)) to the higher energy (Ca sites (1) and (4)) states. The Ca-Mn bond distances are longer for the lower energy solutions, when compared to the metastable states. This is consistent with a simple electrostatic picture in which the Ca ion and hole repel each other.

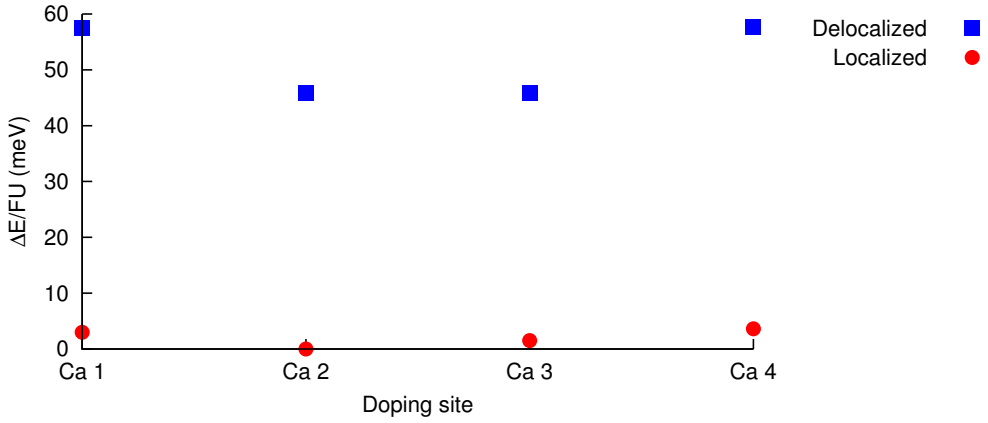


Figure 6.6: Energy difference (ΔE) per formula unit (FU) with respect to the ground state (FM with hole localised at Ca site 2) as a function of doping site for both the localised and delocalised hole solutions in the optimized ground state geometry. In the case of the delocalised hole solution, site 1 is equivalent to 4, and 2 to 3 by symmetry.

6.5.3 Disordered Ca Distribution

In Table 6.2, a deviation from the orthorhombic symmetry due to an ordered distribution of Ca is observed. An approximation to the disordered structure is made by fixing

Site	ΔE (meV)	Ca-Mn (Å)	$E_g \uparrow$ (eV)	$E_g \downarrow$ (eV)
1	12.0	3.214	2.00	4.22
2	0.0	3.325	2.02	4.22
3	6.1	3.328	2.02	4.22
4	14.5	3.223	1.99	4.22

Table 6.4: The energetics for Ca doping sites 1-4 in $La_{0.75}Ca_{0.25}MnO_3$, relative to the ground state (Ca site (2)). The calculated Ca-Mn bond distances are also shown, where the hole is localised on a Mn ion. The band gaps for the majority (↑) and minority (↓) spin states are given.

the angle β and optimising the lattice parameters and internal coordinates. The lattice parameters for the *Pnma* orthorhombic structure (α=β=γ=90°) are given in Table 6.5, where the relative energies of the metastable states with respect to the ground state are given. The energy difference between the monoclinic and orthorhombic localised hole solutions is of the order of 6meV. This is an approximation to the energy scale required to modify the Ca distribution, which suggests that at RT, a disordered distribution is expected, as observed experimentally [187].

	ΔE (meV)	**a**(Å)	**b** (Å)	**c**(Å)	α (°)	β (°)	γ (°)	V (Å^3)
D	65.8	5.652	7.791	5.556	90.0	90.0	90.0	244.7
L	5.56	5.631	7.843	5.548	90.0	90.0	90.0	245.0
Exp. [187]		5.470	7.734	5.489	90.0	90.0	90.0	232.2

Table 6.5: Optimized and experimental [187] lattice parameters for the *Pnma* orthorhombic $La_{0.75}Ca_{0.25}MnO_3$ delocalised (L) and localised (D) hole solutions. The relative energy of these states is calculated with respect to the ground state given in Table 6.2.

6.5.4 Magnetic Stability

The change in energy ΔE for spin configuration types - F, A, C and G - (for the most stable doping site, Ca site 2) is also shown in Fig. 6.7. As determined previously from the DOS and spin density plot, the ferromagnetic spin configuration is the ground state for both the localised and delocalised hole solutions. The G-type magnetic structure is the highest in energy, since AFM coupling along each crystallographic axis is energetically unfavourable for the low hole doping region of the phase diagram. The difference between the FM and A-AFM spin configurations is 20meV and 67meV for the localised

and delocalised hole solutions, respectively.

To understand the anti-JT polaronic distortion of the lattice, the spin moment of the Mn atoms for the ground and metastable states is indicated in Table 6.6. In the localised case, all the Mn atoms in the unit cell are inequivalent. Consequently, the possible number of spin configurations is larger than the delocalised case where two Mn atoms are inequivalent. The average magnetic moment for the delocalised state is $3.7\mu_B$/Mn. This is in good agreement with the experimental ferromagnetic moment of $3.4\mu_B$/Mn [179]. The magnetic moment for the ground state is $3.2\mu_B$, this is very close to the value of $3\mu_B$, which is expected for a completely localised hole. The $\uparrow\downarrow\uparrow\uparrow$ and $\uparrow\downarrow\uparrow\downarrow$ spin configurations result in a localised hole. However, the initial state is that of a delocalised hole. Thus providing evidence of a strong spin-charge coupling.

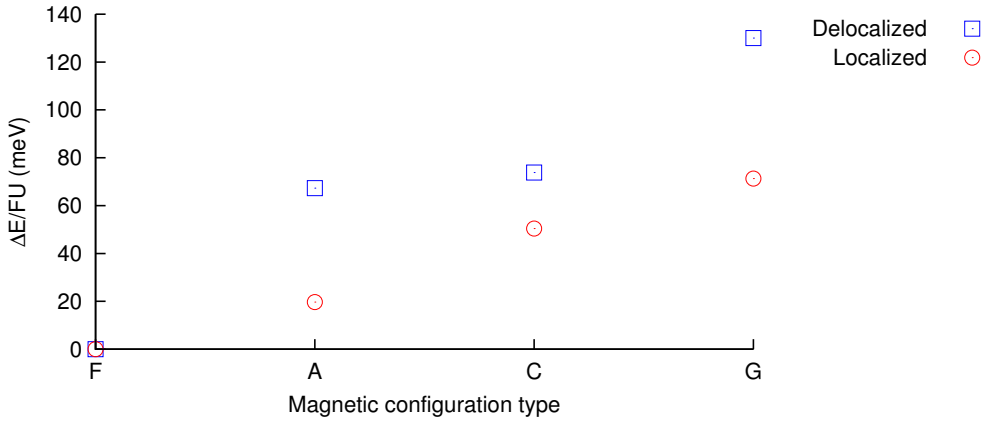


Figure 6.7: Energy difference (ΔE) per formula unit (FU) with respect to the ground state (FM with hole localised at Ca site 2) as a function of the spin configurations (types: F, A, C, G) for both the localised and delocalised hole solutions at the optimised ground state geometry.

6.5.5 Magnetic Coupling Constants

In the previous section, the nature and distribution of the spin density of $La_{0.75}Ca_{0.25}MnO_3$ was analysed. This section focuses on the analysis of the magnetic interactions between the Mn spins, which determine the observed magnetic phase. To achieve this, the energies of the F-, A-, C- and G-type spin configurations are employed, which are shown in Table. 6.6. The low-lying magnetic states are mapped onto the anti-ferromagnetic Ising model, which is represented by the Ising Hamiltonian. As described previously, this effective Hamiltonian describes the pairwise nearest-neighbour interac-

	SC	ΔE/FU (meV)	Mn1 (μ_B)	Mn2 (μ_B)	Mn3 (μ_B)	Mn4 (μ_B)
D	↑↑↑↑	0.0	3.86	3.52	3.52	3.86
	↓↑↑↑	45.0	-3.73	3.36	3.55	3.82
	↑↓↓↑	67.3	3.77	-3.40	-3.40	3.77
	↑↑↓↓	73.8	3.87	3.41	-3.45	-3.88
	↑↓↑↑	102.5	3.73	-3.63	3.12	3.82
	↑↓↑↓	130.4	3.73	-3.68	2.81	-3.75
L	↑↑↑↑	0.0	3.82	3.81	3.15	3.80
	↑↑↓↓	19.7	3.83	3.82	-3.05	-3.71
	↑↑↑↓	34.3	3.82	3.81	2.94	-3.73
	↑↓↓↓	34.8	3.74	-3.73	-3.14	-3.71
	↑↑↓↑	35.0	3.82	3.81	-2.82	3.82
	↑↓↑↑	36.2	3.73	-3.74	3.05	3.80
	↑↓↓↑	50.4	3.73	-3.73	-2.94	3.82
	↑↓↑↓	71.3	3.74	-3.74	2.83	-3.73

Table 6.6: Relative energies of various spin configurations per formula unit (FU) with respect to the ground state in the delocalised (D) and localised (L) hole optimised geometries. The expected total spin and calculated Mn spin moments are also shown.

tions of the Mn spin moments. The assumptions described to compute J_{ap} and J_{eq} for the end-point compounds have also been used for the doped compound. In the case of the delocalised hole, the spin values were taken to be S=3.75/2, and for the localised hole S=3/2 (see Appendix C). The determined J_{ap} and J_{eq} are given in Table 6.7. Since the in-plane and out-of-plane magnetic coupling is FM, the calculated exchange constants are positive. It is also evident that the FM coupling along J_{ap} is almost a factor of 2 larger than the J_{eq} for the metal. In comparison, J_{ap} and J_{eq} for the localised hole solution are smaller than those for the delocalised hole. This is attributed to the polaron ordered and insulating nature of the ground state. The computed values are comparable to the nearest neigbour exchange coupling constant of 7.83±0.06meV determined from inelastic neutron scattering measurements, where a Heisenberg model has been implemented to describe the magnon dispersion relation of $La_{0.75}Ca_{0.25}MnO_3$ [189].

	J_{ap} (meV)	J_{eq} (meV)
Delocalised	10.5	4.78
Localised	2.62	3.36

Table 6.7: Calculated J_{eq} and J_{ap} in meV for the delocalised and localised hole solutions.

6.6 Summary

Hybrid-exchange DFT calculations have been used to study the structural and electronic properties of $La_{0.75}Ca_{0.25}MnO_3$, which adequately reproduce major experimental features. The evolution of the structural properties as a function of doping, from $LaMnO_3$, have been investigated. The predicted most stable phase for an ordered Ca distribution in $La_{0.75}Ca_{0.25}MnO_3$ is the orthorhombic ferromagnetic-insulating (polaronic) state. An anti-JT polaron forms and the localised state is influenced by long range cooperative anti-JT distortions. The computed results for the delocalised hole are, in fact, fully consistent with the half-metallic behaviour displayed by the material [190]. Further, the calculated magnetic moment of $3.7\mu_B$/Mn is in agreement with the observed magnetic behaviour [179]. The magnetic coupling constants for the metastable and ground state were obtained from the total-energy differences computed for a set spin configurations within a simple nearest-neighbour Ising model. The magnitude (and the sign) of these constants indicates that the parallel arrangement of the magnetic moments is due to a strong ferromagnetic coupling between the Mn ions in all crystallographic directions, particularly for the metal. Competing interactions (summarised in Table 6.8), such as the hole conductivity, doping site, spin ordering and the magnetic coupling were disentangled and quantified. It has been deduced that the relative energy scales are of a similar magnitude, which indicate strong coupling between charge, orbital, spin and lattice degrees of freedom. This implies that there is not a dominant energy contribution, which may have significant implications on the MCE in the low hole density region of the $La_{1-x}Ca_xMnO_3$ phase diagram. This chapter completes a microscopic description of the lightly-doped insulator with an antiferromagnetic-to-ferromagnetic and metal-to-insulator transition.

	Energy (meV)
Hopping barrier	46
Disordered Ca distribution	6
Doping site dependence	6-12
Magnetic stability	0-130
Magnetic coupling	3-11

Table 6.8: Summary of the energetics determined (in meV) for competing interactions in $La_{0.75}Ca_{0.25}MnO_3$.

7

Entropy Contributions to the MCE

In this chapter, a combination of thermodynamics and first principles theory is applied to describe the MCE in $La_{0.75}Ca_{0.25}MnO_3$, which undergoes a phase transition from a FM-M to PM-I. Despite many experimental efforts to enhance the entropy change in manganites, the maximum ΔS_{iso} determined merely reaches modest values in the field of a permanent magnet [15, 18, 19, 76, 77, 80, 82–86, 191]. In the previous chapter, it has been demonstrated that the spin, orbital, lattice and electronic degrees of freedom are strongly intertwined. One may anticipate a large entropy change across the phase transition, in such strongly coupled systems, since a significant structural or volume change may occur at the magnetic transition. In this work, a preliminary approximation to the total entropy change ΔS for $La_{0.75}Ca_{0.25}MnO_3$ is made by quantifying the separate electronic, vibrational, elastic and magnetic contributions for a simple model with long range translational order. Thus, the charge, lattice and spin degrees of freedom are treated independently.

Through the implementation of first principles thermodynamic theory and the molecular field approximation, the Gibbs free energy can be expressed as [53]:

$$G(T, P, H) = U_{vib} + U_{elas} + U_{elec} + U_{ex} - MH + PV - TS \tag{7.1}$$

where the first four terms correspond to the internal energy (vibrational, elastic, electronic and magnetic, respectively). The fundamental assumption that the entropy change can be expressed as,

$$\Delta S_{total} = \Delta S_{vib} + \Delta S_{elas} + \Delta S_{elec} + \Delta S_{mag} \tag{7.2}$$

where ΔS_{vib}, ΔS_{elas}, ΔS_{elec} and ΔS_{mag} are the vibrational, elastic, electronic and magnetic contributions, respectively, is made. Equation 7.2 corresponds to the total isothermal change of the entropy (ΔS_{iso}) when a magnetic field is applied, which can also be determined using the Maxwell relations. We test the assumption of independent contributions by computing each and comparing to available experimental data.

Electronic structure and lattice dynamics of the spin disordered PM-I phase are approximated by that of the FM-I from the hybrid-exchange density functional calculations. The temperature dependence of the magnetisation and the ΔS_{mag} is studied using the Ising model for a cubic lattice, which is implemented within the MC approach (a MC code has been written and developed specifically for this purpose). Here, the magnetic coupling constants J_{ap} and J_{eq} determined from the DFT calculations have been used to parameterise the Ising Hamiltonian with an average of the two constants J_{ave}. Furthermore, the $Mn^{3.75+}$ is described by a classical Ising spin, and the La, Ca and O ions are considered to be non-magnetic in the MC simulations.

In Figure. 7.1, the change in the lattice parameters and cell volume of $La_{0.75}Ca_{0.25}MnO_3$, as a function of temperature, as obtained from high-resolution synchrotron x-ray powder diffraction data by Radaelli *et al.* is shown. An isotropic expansion of the cell occurs, without affecting the orthorhombic symmetry. The $\Delta V/V$ across the phase transition, as the system transits from a FM-M to a PM-I, has been determined to be $\sim 0.13\%$ [81]. This provides evidence for a lattice change accompanied with the FM-M to PM-I transition in $La_{0.75}Ca_{0.25}MnO_3$. It is expected that the ΔS_{iso} for this particular composition would be considerable, since the electronic and lattice contributions may play a significant role in enhancing the entropy change [81,192]. Further, the expected maximum theoretical entropy due to independent spins is $12.5 Jmol^{-1}K^{-1}$ which is calculated using the following expression (for a mole of magnetic atoms) [193],

$$S_{mag} = N_A k_B ln(2J+1) \equiv R ln(2J+1) \tag{7.3}$$

where J is the quantum number of the total angular momentum and is considered to be equal to the spin number, since the orbital angular momentum is completely quenched. However, the ΔS_{iso} determined from magnetization measurements of $La_{0.75}Ca_{0.25}MnO_3$ nanoparticles is -4.70$Jkg^{-1}K^{-1}$ (under an applied magnetic field of H=1.5T) [18]. It is not clear whether the entropy contributions counteract each other and therefore, in this chapter, the individual components of the entropy change occur-

ring due to the FM-M to PM-I phase transition in $La_{0.75}Ca_{0.25}MnO_3$ are separated and quantified.

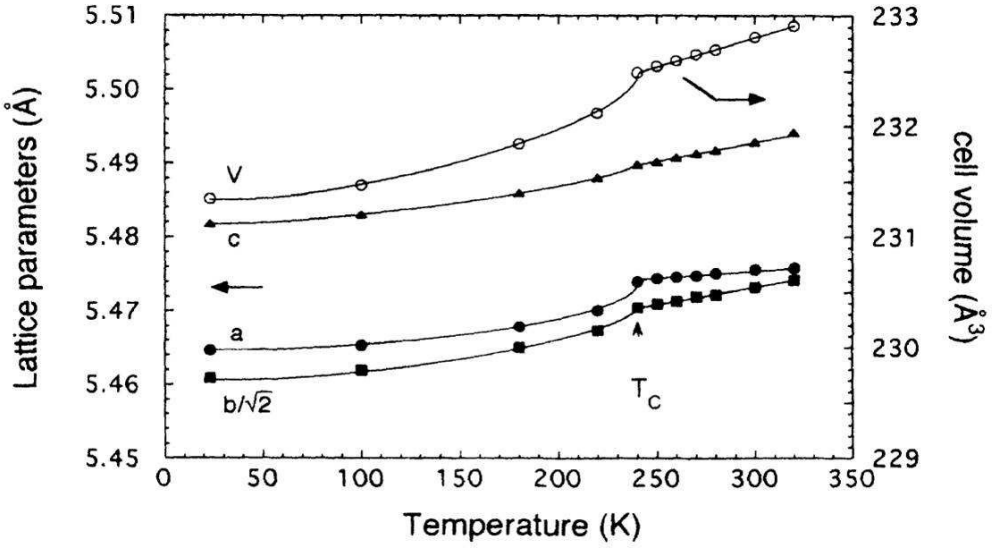


Figure 7.1: Lattice parameters and cell volume of orthorhombic $La_{0.75}Ca_{0.25}MnO_3$ as a function of temperature. Data obtained from high-resolution synchrotron X-ray powder diffraction data. The error bars are smaller than the symbols. Reprinted figure with permission from Ref. [81]. Copyright 1995 by the American Physical Society, see http://journals.aps.org/prl/abstract/10.1103/PhysRevLett.75.4488

7.1 Electronic Entropy

The M-I transition in $La_{0.75}Ca_{0.25}MnO_3$ modifies the density of states at the Fermi level, and strong evidence for this has been provided in the previous chapter. Consequently, the electronic entropy for the metallic and insulating phases is expected to differ significantly. The electronic entropy contribution to ΔS is computed using the finite temperature DFT approach [194], which allows one to express the free energy in terms of the Fermi function (given in Equation. 7.5),

$$F = E(T) - k_B T S(T) \tag{7.4}$$

$$f_i = (1 + e^{\frac{(\epsilon_i - \epsilon_F)}{k_b T}})^{-1} \tag{7.5}$$

$$S = \sum_{i}^{N_{states}} f_i ln f_i + (1 - f_i) ln(1 - f_i) \tag{7.6}$$

where N and f are the density of electronic states and Fermi distribution function, respectively. The Fermi function describes the probability of occupation at a certain temperature, which can be summed over all the k-points in the Brillouin zone for each band to determine the occupation levels. The computed values of the electronic entropy, ΔS_{elec} at 10K, 100K and 224K (T_{C}) are given in Table. 7.1. The values are positive, since S_{elec} for the insulator is zero and the transition is from a M to an I. As the temperature is increased from 10-224K, the magnitude of ΔS_{elec} increases.

ΔS_{elec} ($\mathrm{Jmol^{-1}K^{-1}}$)	Temperature (K)
0.01	10
0.19	100
0.45	224

Table 7.1: The electronic entropy contribution ΔS_{elec} to ΔS for the FM-M (LCMO at x=1/4) at 10K, 100K and 224K (T_C=224K), where S_{elec} for the FM-I is considered to be zero.

The entropy per charge carrier is accessible experimentally via the *Seebeck coefficient*, which is determined through measurements of the induced thermoelectric voltage in response to a temperature difference across the material [195]. This is based on the idea that different temperatures generate different carrier densities and the resulting carrier diffusion causes a thermal electromotive force. The Seebeck coefficient Q has been measured for $\mathrm{La_{0.75}Ca_{0.25}MnO_3}$ and an evident peak occurs at T_C which is indicative of a considerable ΔS_{elec}, as can be seen in Figure. 7.2.

Subsequently, we can estimate the experimental electronic contribution to the entropy change, which has been determined to be $\sim$0.17$\mathrm{Jmol^{-1}K^{-1}}$ (0.8$\mathrm{Jkg^{-1}K^{-1}}$) for a ΔH of 1T, from the following expression,

$$\Delta S_{elec}(T, \Delta H) = -\Delta Q N_x e, \tag{7.7}$$

where N_x is the carrier concentration and e is the charge of an electron. This is a similar order of magnitude when compared to the theoretical value obtained in this investigation using the finite temperature DFT approach.

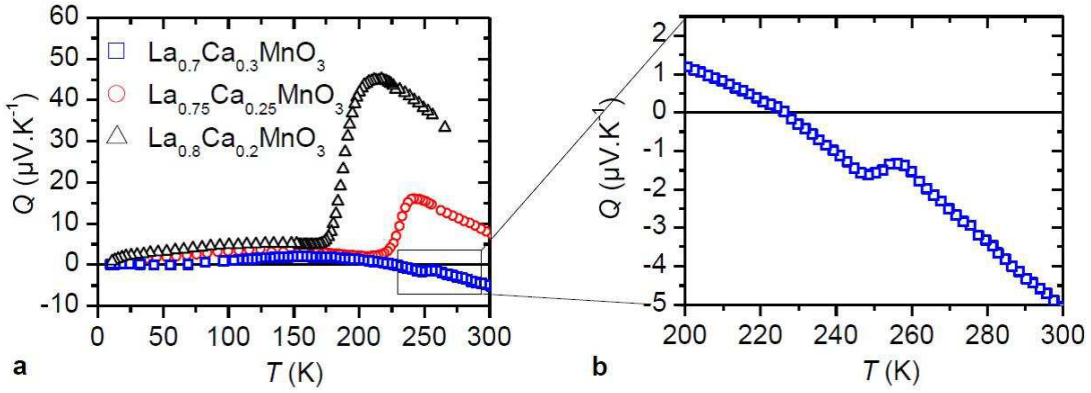


Figure 7.2: Seebeck coefficient Q obtained by Turcaud *et al* (with permission and this work is to be published) for $La_{1-x}Ca_xMnO_3$ at x=0.2, 0.25 and 0.3.

7.2 Vibrational Entropy

In order to sample the vibrational modes, the vibrational frequencies for the primitive (Γ-point, $\mathbf{k}$=0) and isotropic supercell (80 atom) were computed to determine the vibrational contribution S_{vib} to ΔS. The mass-weighted Hessian (or dynamical) matrix [196] is calculated by numerical evaluation of the first derivative of the analytical atomic gradients; the eigenvalues of the Hessian matrix correspond to the vibrational frequencies. Consequently, the vibrational specific heat (Equation. 7.8) and entropy (Equation. 7.10) have been calculated in the harmonic approximation, which are given in Table. 7.2.

$$C_{vib} = \left(\frac{\partial E}{\partial T}\right)_V = \sum_{k,j} k_B \left(\frac{\hbar\omega}{k_B T}\right)^2 = \frac{exp(\hbar\omega/k_B T)}{[exp(\hbar\omega/k_B T) - 1]^2} \tag{7.8}$$

$$F_{vib} = E_0 + \frac{1}{2}\sum_{k,j} \hbar\omega + k_B T \sum_{k,j} ln\left[1 - exp(-\hbar\omega/k_B T)\right] \tag{7.9}$$

$$S_{vib} = -\frac{\partial F_{vib}}{\partial T} \tag{7.10}$$

An increase in the vibational entropy, for the metal and insulator, is apparent when the cell is doubled. The S_{vib} for the metallic state is higher than that of the insulator as expected, and is evident in Table. 7.10. This is attributed to the softening of the vibrational modes in the metallic state. Further, the calculated ΔS_{vib} is 4.64 $Jmol^{-1}K^{-1}$ and is also positive (as is ΔS_{elec}).

Cell	Matrix elements	M/I	C_{vib} ($Jmol^{-1}K^{-1}$)	S_{vib} ($Jmol^{-1}K^{-1}$)
Primitive	$\begin{bmatrix} 1 & 0 & 0 \\ 0 & 1 & 0 \\ 0 & 0 & 1 \end{bmatrix}$	M	80.69	68.27
		I	78.02	58.65
				9.62
Double	$\begin{bmatrix} 1 & 0 & 1 \\ 0 & 1 & 0 \\ -1 & 0 & 1 \end{bmatrix}$	M	96.38	92.97
		I	94.59	88.33
				4.64

Table 7.2: The vibrational specific heat and entropy for LCMO at x=1/4, in the FM-M and FM-I states for the primitive cell and supercell, for which the matrix elements are defined in the second column. The ΔS_{vib} is given in italics in units of $Jmol^{-1}K^{-1}$.

7.3 Elastic Entropy

The elastic contribution to the total entropy change has been calculated from the following [53]:

$$\Delta S_{elas} = \frac{1}{T_C}\frac{B}{2}\left(\frac{\Delta V}{V}\right)^2 \tag{7.11}$$

where the value for the bulk elastic modulus B is taken to be 100GPa, which has been determined from the ultrasonic properties of $La_{0.67}Ca_{0.33}MnO_3$ [197]. The ΔV in this particular calculation corresponds to the difference in volume between the FM-M (244.8Å^3) and FM-I (245.1Å^3) state from the DFT calculations, which is 0.3Å^3. If we then assume the experimental T_C of 224K [18], the ΔS_{elas} is $1.81\times10^{-4}Jmol^{-1}K^{-1}$. The elastic contribution to ΔS is therefore, considered to be a negligible term. If, however, we assume the ΔV reported by Radaelli *et.al.* which is determined from high-resolution synchrotron x-ray powder diffraction data [81], then the ΔS_{elas} is $2.03\times10^{-4}Jmol^{-1}K^{-1}$, which is also based on the bulk modulus value of 100GPa. Therefore, the theoretical ΔS_{elas} is reasonable, since the experimental value is also negligibly small.

7.4 Magnetic Entropy

The FM-PM phase transition has been investigated through the implementation of the Ising model in a Monte Carlo approach. Initially, in section 7.4.1, the 2D model is considered and macroscopic quantities such as the internal energy, magnetisation, magnetic specific heat and succeptibility have been calculated as a function of temperature (at constant volume) for systems of finite size in the absence of a magnetic field. The effect of the lattice size on the thermodynamic properties is investigated and the obtained T_C value is compared to Onsager's analytical solution for the 2D Ising model. The developed code is validated by considering limiting cases (low and high temperatures), which are given in Appendix E. The 3D Ising model is then implemented in section 7.4.2 to determine the magnetocaloric properties of $La_{0.75}Ca_{0.25}MnO_3$ as a function of temperature. Furthermore, the ΔS_{mag} is quantified for a varying magnetic field of ΔH=2 and 4T, which is compared to available experimental data.

7.4.1 2D Ising Model

The systems considered were square lattices of spin sites ranging in size (where N corresponds to a single spin site) from 16x16 to 32x32. Periodic boundary conditions were implemented by calculating all quantities within an array size smaller than that allocated in the code. This ensured that all sites outlining the lattice had an equal number of neighbouring sites within the lattice. The exchange constant J and Boltzmann constant k_B were set to 1, such that the inverse temperature T^{-1} was equal to β. Consequently, the relevant temperature is referred to as the *reduced temperature* T_R, and the units are dimensionless. The internal energy was calculated from the first term in the Ising Hamiltonian since the external magnetic field H was set to zero. Each lattice site was assigned a spin variable $S = \pm 1$. The average magnetisation per lattice site <M> has been determined by summing S over all sites and dividing by the number of lattice sites N.

In order to obtain accurate results, it is important to establish that the lattice has thermalised. This is a process by which the system is brought to equilibrium at a given temperature. The magnetisation is changing up until thermalisation, after which it fluctuates around a steady average value. In this investigation, thermalisation was achieved by taking the initial configuration of the lattice and applying the Metropolis algorithm until equilibrium had been reached. The magnetisation at each Monte Carlo step was then computed to determine the number of steps required for equillibriation. When the magnetisation stabilised, it was assumed that the system had equilibrated.

At this point, measurements of quantities such as energy, magnetisation, susceptibility and specific heat were initiated. Such quantities were summed and then averaged from the point of equilibrium to a point at which the system was in a significantly differing state, this interval is also commonly referred to as the *correlation time*. The assumption that the equillibriation time is equal to the correlation time was made [1] in order to determine an estimate for the expectations values of all quantities.

Since there exists an analytical solution for the two dimensional (2D) Ising model in the absence of an external magnetic field, the reliability and accuracy of the developed code has been examined through a comparison of the calculated T_{C} and the theoretical value. The average energy, magnetisation, specific heat and susceptibility per spin has been determined for a system of 16x16 and 32x32 sites. The results are shown in Figs 7.3 and 7.4, which also indicate Onsager's analytical solution for the critical temperature. The computed energy is still significantly below zero for the maximum temperature considered in the simulation. This suggests that the neighbouring spins are still correlated, despite the fact that the bulk magnetisation averages to zero. Although the energy and magnetisation remain relatively unaffected by the lattice size, it can be seen that the primary features of the phase transition in the specific heat capacity and susceptibility became more rounded in significantly smaller lattice sizes, leading to an ambiguity in determining the critical point. This observation is also referred to as a *finite size effect* [198, 199].

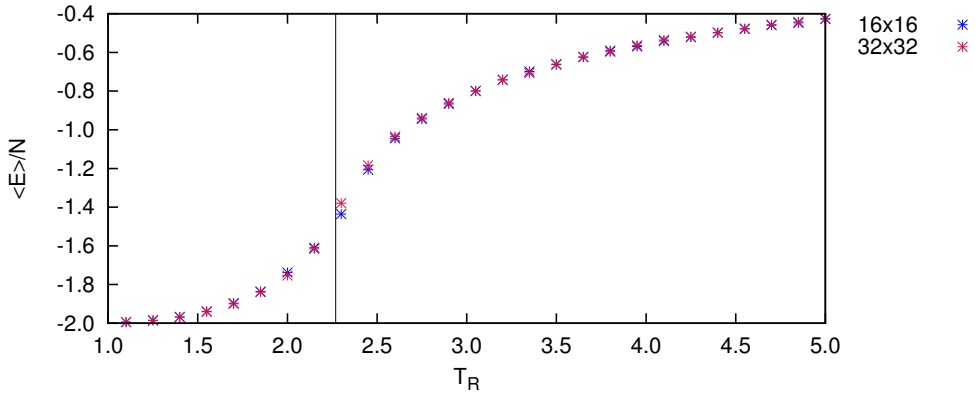
Spontaneous magnetization exists for all temperatures below T_{C}=2.269 [200] for the 2D Ising model (at zero field). The Curie temperature obtained from the Monte Carlo code is in good agreement with the theoretical value, since a value of T_{C}=2.4 is obtained. The sharp change in the energy and magnetisation per spin at $T\approx 2$ is evident in Fig. 7.3. Further, the fluctuations in $<E>$ and $<M>$ at the phase transition are associated with the C_v and χ, consequently a sharp divergence is observed in these quantities. Such features are typical characteristics of a phase transition. The results for the $<M>$ per spin above the transition temperature indicate that the magnetisation is small, whereas below this point, it is non-zero, and close to 1 for very low temperatures. This behaviour is sensible and in agreement with expectations of a FM-PM phase transition, since the change from one phase to the other is infinitely sharp in the thermodynamic limit.

Qualitative information about the phase transition has been obtained using DL Visualize. A snapshot of the system spin configuration has been taken at different

[1] In particular, this assumption worked fine for the Metropolis simulation of the Ising model considered herein [198].

temperature intervals to visualize the phase transition and is shown in Figure. 7.5. There are regions of coexistence of two phases in the lattice, at T=2.0 and 2.5, which is indicative of the FM-PM phase transition that occurs between these temperatures. The differences between the MC simulation results and the exact analytical results arises due to the fact that a finite number of spins are considered.

(a)



(b)

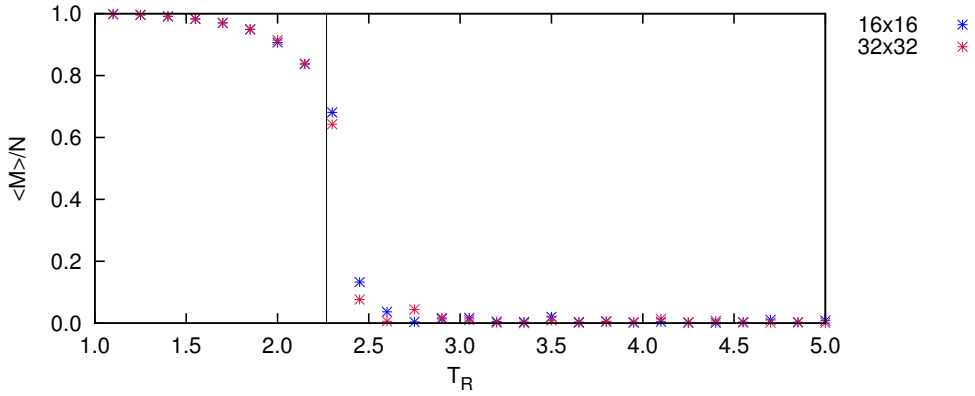
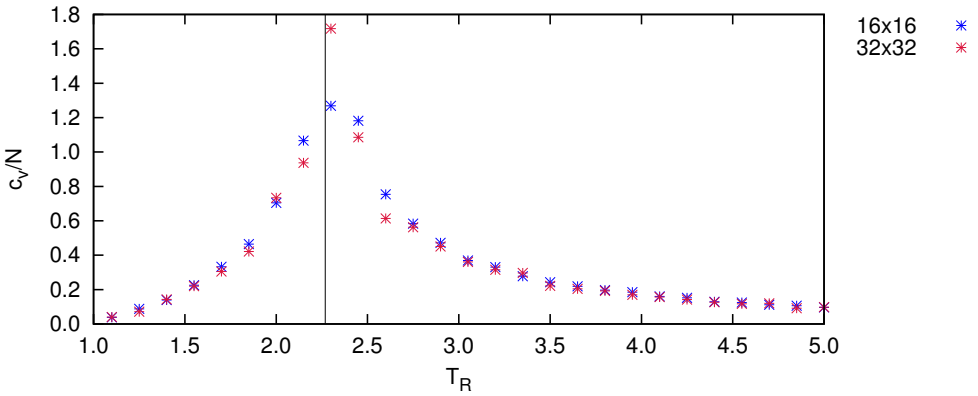


Figure 7.3: The average (a) Energy and (b) Magnetization per spin as a function of temperature calculated by Monte Carlo simulation for various lattice sizes. The vertical line at T_R=2.269 corresponds to Onsager's analytical value for the transition temperature T_C.

(a)



(b)

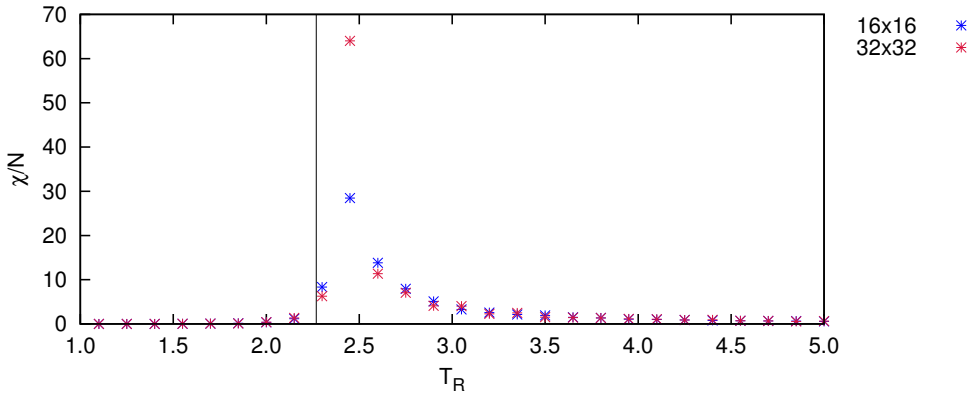


Figure 7.4: (a) Specific heat and (b) Magnetic susceptibility per spin as a function of temperature calculated by Monte Carlo simulation for various lattice sizes. The vertical line at T_R=2.269 corresponds to Onsager's analytical value for the transition temperature T_C.

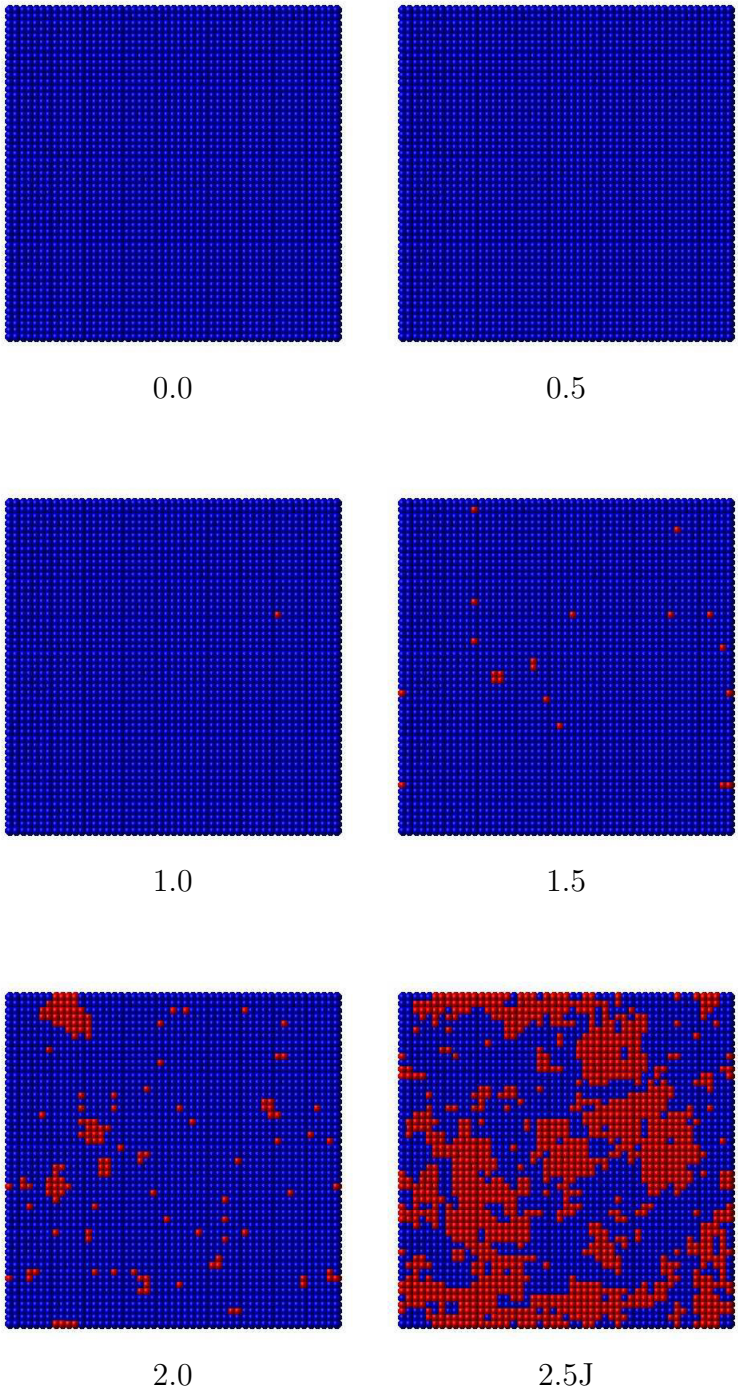


Figure 7.5: Configuration snapshots of a 50x50 square lattice at a finite temperature T (where J and k_B are equal to 1). The FM-PM magnetic phase transition is shown, where blue=spin up and red=spin down.

7.4.2 3D Ising Model

In this section, results corresponding to the 3D Ising model are reported. The Ising Hamiltonian has been parameterised with the exchange coupling constant J_{ave} calculated by averaging J_{ap} and J_{eq} determined from the hybrid-exchange DFT calculations for the FM-M (delocalised hole solution), which are given in Table 7.3. There are two independent model parameters in the MC simulations, the exchange coupling constant J_{ave} and the applied field H, which have been defined in units of meV. The Lande factor g has been taken as g=2. Further, the number of sites used in the simulations is N=10^3, and for a given temperature, the number of Monte Carlo steps to calculate equillibrium averages was taken as 10^6. The magnetic entropy has been computed using the following expression:

$$S_{mag} = \int_{T_1}^{T_2} \frac{C_{mag}}{T} dT \tag{7.12}$$

where the change in magnetic entropy corresponds to the difference in entropy in the presence (S_H) and absence (S_0) of a field, ΔS_{mag}=S_H - S_0. Since the results are compared to experimental data, particularly for ΔS_{mag}, the Boltzmann constant k_B has been set equal to 8.62×10^{-2}meV/K (in contrast to the 2D Ising model results in the previous section, where k_B=1).

	J (meV)
Apical	10.5
Equatorial	4.78
Average	6.69

Table 7.3: Calculated J_{ap}, J_{eq} and J_{ave} in meV for the FM-M (delocalised hole) $La_{0.75}Ca_{0.25}MnO_3$ from hybrid-exchange DFT calculations, where J_{ave} is an input parameter for the MC simulations.

Fig. 7.6 shows the temperature dependence of the internal energy and specific heat capacity for J_{ave} in the absence of a magnetic field. The discontinuity in the energy at T_C is evident, however, it does not diverge sharply at the transition, which could be attributed to strongly correlated regions such as clusters in large systems that are somewhat unaffected by single spin flips at the transition point. Consequently, the decrease in energy occurs over a broader temperature range in the critical region. Characteristic features of the order-disorder transition are also observed in the specific heat. The critical temperature $T_C \sim 320$K has been determined from the peak in the c_v curve, which occurs at 0.17mevK^{-1}. The calculated T_C has been overestimated by 30-44% when

compared to the T_C values of 177K and 224K determined from magnetisation measurements (defined as the maximum slope in dM/dT) of $La_{0.75}Ca_{0.25}MnO_3$ nanoparticles of different sizes [76].

The magnetic entropy S_{mag} and the change in magnetic entropy ΔS_{mag} for ΔH of 2 and 4T is shown in Fig. 7.7. The entropy is a continuous function of temperature and exhibits a discontinuity at T_C. At high temperatures, the magnetic entropy saturates since the system is in a completely disordered state. The saturation value corresponds to 0.69meV/K in Fig. 7.7. The maxima of the field-induced magnetic entropy change ΔS_{mag} occurs in the vicinity of T_C and the determined values are -3.75 and -6.60 $Jmol^{-1}K^{-1}$ (which correspond to -17 and 30 $Jkg^{-1}K^{-1}$, respectively). When compared to experimental data for ΔS_{iso}, the computed values are significantly larger than -1.03$Jmol^{-1}K^{-1}$ (4.7$Jkg^{-1}K^{-1}$), which has been calculated from magnetisation measurements of $La_{0.75}Ca_{0.25}MnO_3$ for an applied magnetic field of H=1.5T [18].

7.5 Summary

In this chapter, the electronic, lattice and magnetic contributions to the total entropy change, for $La_{0.75}Ca_{0.25}MnO_3$, have been studied by means of a combined DFT and Monte Carlo approach and are given in Table 7.5. In principle, the entropy change determined from experiments is not entirely a magnetic entropy change, but a total one due to the simultaneous variation of the magnetic order and phase volume at the transition. The results obtained from this investigation indicate that both the electronic and lattice entropy terms undergo a reduction at the FM-M to PM-I transition, and are therefore expected to counteract the magnetic one.

Term	Entropy ($Jmol^{-1}K^{-1}$)
Electronic	0.45
Vibrational	4.64
Elastic	2.03×10^{-4}
Magnetic	-6.60

Table 7.4: The calculated electronic, lattice and magnetic entropy contributions to ΔS for $La_{0.75}Ca_{0.25}MnO_3$.

The finite temperature DFT approach has been implemented to determine the electronic contribution, which is in good agreement with measurements of the Seebeck coefficient for $La_{0.75}Ca_{0.25}MnO_3$. The ΔS_{vib} term, which has been calculated in the

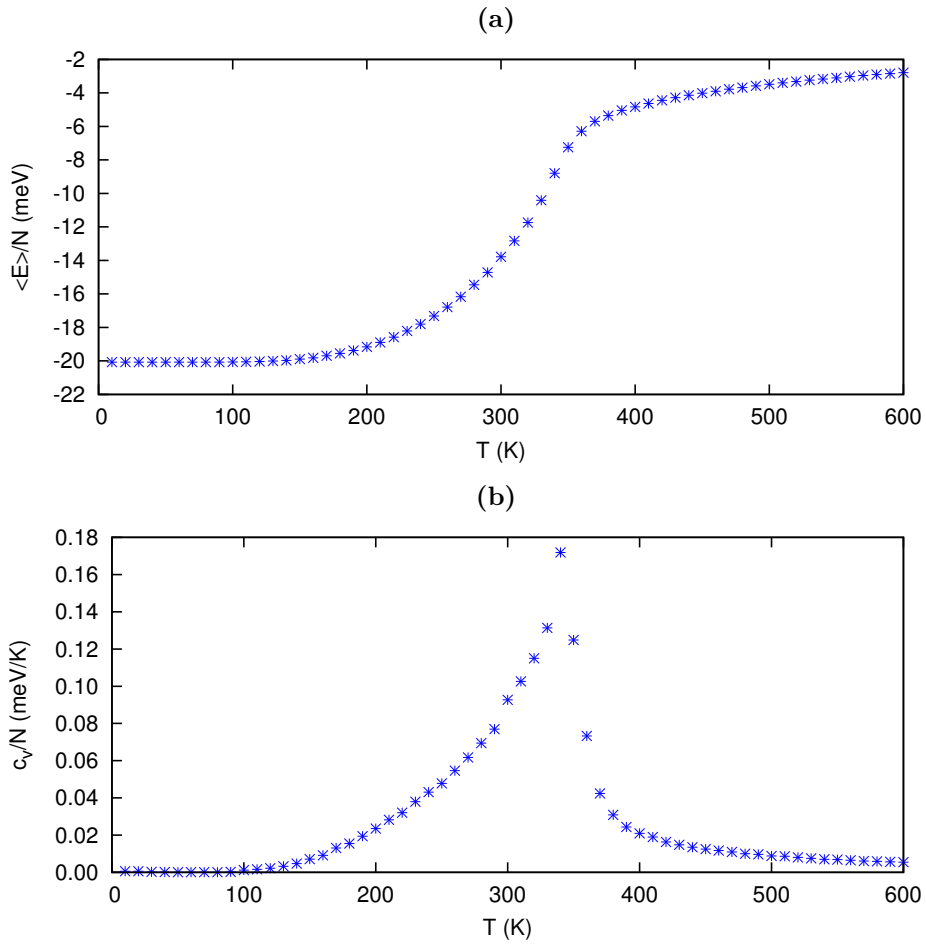


Figure 7.6: (a) energy and (b) specific heat capacity per spin calculated by the MC simulation for J_{ave} in a 10×10×10 lattice.

simple harmonic approximation, is the dominant positive term contributing to the total entropy change and is significant enough to have a deleterious effect. Further, the elastic contribution to the lattice entropy has been determined using $\Delta V/V$ for the metallic and insulating phases, and is negligibly small relative to the entropy contributions considered herein. The magnetic entropy and the T_C for $La_{0.75}Ca_{0.25}MnO_3$ have been computed through the implementation of a Monte Carlo code and the Ising Hamiltonian, which has been parameterised with the average nearest-neighbour coupling constant J_{ave} determined from hybrid-exchange DFT calculations. Further, the determined T_C value has been overestimated when compared to available experimental data. The field-induced magnetic entropy change has been quantified, and is of a similar magnitude to the vibrational term, but contributes negatively to ΔS.

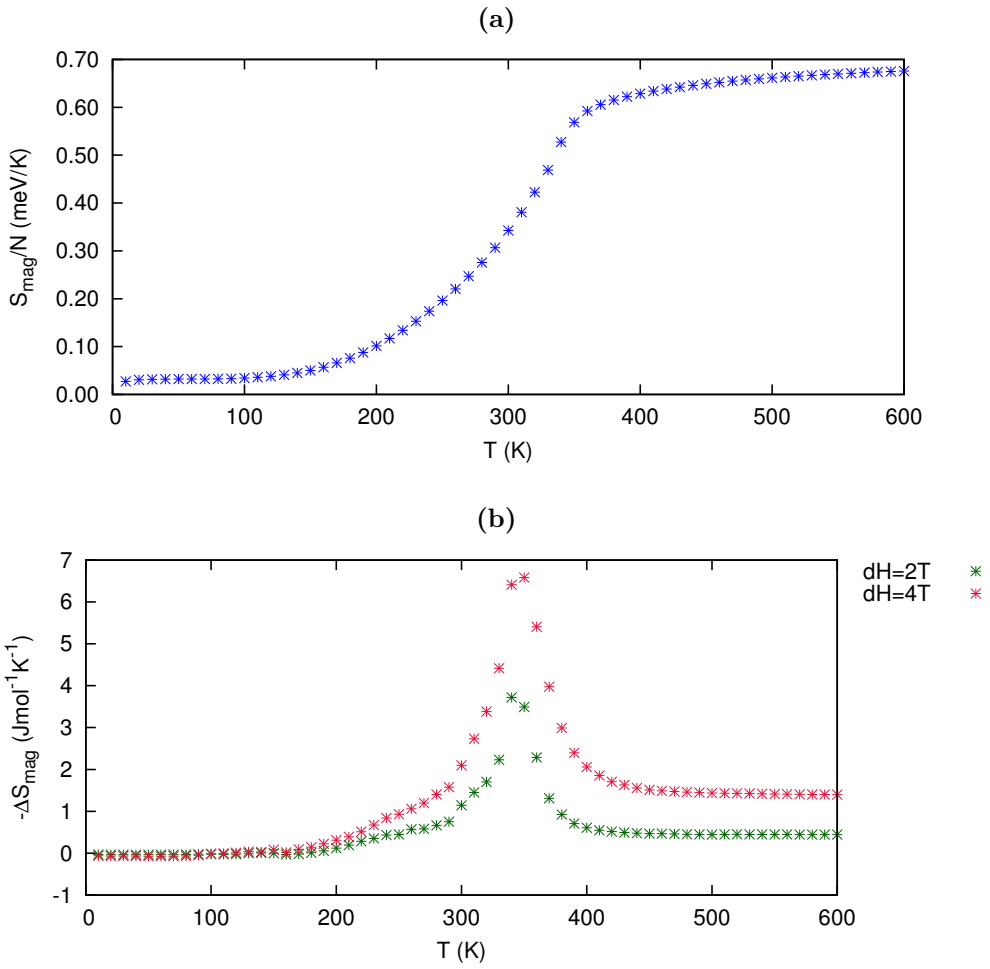


Figure 7.7: The magnetic entropy in zero field and the change in magnetic entropy - ΔS_{mag} due to an applied field ΔH of 2T and 4T, as a function of temperature calculated for J_{ave} in a 10×10×10 lattice.

It must be noted, however, that numerous approximations have been made in quantifying individual contributions to ΔS. Primarily, both the vibrational and elastic entropy terms are actually implicit functions of the magnetisation due to the magnetolattice coupling in $La_{0.75}Ca_{0.25}MnO_3$, which could be taken into consideration to progress further towards a complete predictive theory. In addition, for ΔS_{mag}, in the vicinity of a magnetoelastic transition, an extreme sensitivity of the J parameter with respect to small abrupt changes in the volume at the the transition is expected and could, therefore, be taken into account in the calculation of J. Hence, an explicit inclusion of a magnetoelastic coupling term in the Monte Carlo simulations may lead to

an improved estimation of T_{C} and ΔS_{mag}. Finally, one of the limitations that the Ising Model confronts us with is the finite size of the lattice considered. It is thus necessary to use a finite scaling methods in order to determine thermodynamic properties with greater accuracy.

8

Final Conclusions

In this work, periodic hybrid-exchange density functional calculations were performed to develop a first principles understanding of the MCE in the low hole density region of the manganite series $La_{1-x}Ca_xMnO_3$. Initially, the endpoint compounds, $LaMnO_3$ and $CaMnO_3$, were studied to determine the reliability of the B3LYP hybrid density functional in describing the structural and electronic properties of manganite systems. Studying the parent compound was also considered to be a prerequisite to achieve a better understanding of the doped compounds. Following this, the effects of Ca doping on the properties of $LaMnO_3$ were determined, and the relevant structural, magnetic, and electronic contributions to the stability of the doped compound $La_{0.75}Ca_{0.25}MnO_3$ were quantified. Further, through the implementation of fundamental thermodynamics and first principles theory, a preliminary description of the MCE in the doped compound was developed, where the separate electronic, vibrational, elastic and magnetic contributions to the entropy change ΔS, across the FM-M to PM-I phase transition, were quantified.

In Chapter 5, the study was focused on the endpoint compounds, where hybrid-DFT calculations predicted the very different structural and magnetic symmetries of $LaMnO_3$ and $CaMnO_3$ correctly. The most stable phases were found to be A-AFM and G-AFM for $LaMnO_3$ and $CaMnO_3$, respectively. The analysis of the structural properties showed that the MnO_6 octahedra in $LaMnO_3$ were strongly distorted due to the JT effect, however, this distortion was absent in $CaMnO_3$ due to the existence of Mn^{4+} ions. Furthermore, it was found that the O $2p$ and Mn $3d$ states were responsible for the energy bands near the Fermi level, which defined the electronic properties of both, $LaMnO_3$ and $CaMnO_3$. The semi-covalency in $LaMnO_3$ was attributed to a strong hybridization of the O $2p$ and Mn $3d$ bands. Further confirmation was provided by

the spin density analysis, in which the in-plane polarisation of the O-2p orbitals by the Mn-3d was qualitatively evident. The overall investigation of the endpoint compounds provided a fundamental insight into their low temperature structural and electronic properties. More importantly, valuable information about the exchange interaction in $LaMnO_3$ and $CaMnO_3$ was provided.

In Chapter 6, hybrid-exchange density functional calculations were performed to predict the most stable phase for an ordered Ca distribution in $La_{0.75}Ca_{0.25}MnO_3$. The ground state was determined to be the ferromagnetic-insulating state, where the doped hole localised on a particular Mn. An anti-Jahn-Teller polaron was observed and the localised hole state was influenced by long-range cooperative Jahn-Teller distortions. The delocalised hole state displayed half-metallic behaviour, which was fully consistent with experiment. The nearest neighbour magnetic coupling constants J_{ap} and J_{eq} were also determined for the FM-M and FM-I, since the MnO_6 octahedron was affected by a distortion which evidently led to a variation in Mn-O bond distances. The magnitude and sign of J_{ap} and J_{eq} indicated that parallel arrangement of the magnetic moments was favourable due to a strong ferromagnetic coupling between the Mn ions, particularly for the metal. In addition, the calculated magnetic moment of $3.7\mu_B$/Mn was also found to be in good agreement with experiment. The relative energy scales associated with the MCE were quantified and found to be of a similar magnitude. Consequently, this result provided strong evidence of strong coupling between the charge, orbital, spin, and lattice degrees of freedom.

Finally, in Chapter 7, the charge, lattice and spin degrees of freedom were treated independently and a preliminary approximation to ΔS was made. Although a predictive theory was not expected, highly accurate calculations were performed to test our hypothesis. The results obtained from the electronic structure calculations for the FM-I and FM-M states were used to determine the electronic, elastic and vibrational contributions. The finite temperature DFT approach was implemented to compute the electronic contribution. A ΔS_{elec} of $0.45\text{Jmol}^{-1}\text{K}^{-1}$ was obtained, which was found to be in good agreement with experimental data obtained from the Seebeck coefficient. However, in order to make an explicit comparison to experiment, a rigorous calculation could be carried to determine the Seebeck coefficient through the implementation of the Boltzmann transport equations and DFT calculations. The vibrational contribution S_{vib} was computed in the simple harmonic approximation and was found to be higher for the metal when compared to the insulator, due to the softening of the vibrational modes in the former phase. However, improvements to ΔS_{vib} could be made through the implementation of a disordered lattice, as well as calculating ΔS_{vib} in the anharmonic

approximation. The elastic entropy change was found to be negligibly small. A Monte Carlo code implementing the Metropolis algorithm was developed to simulate the spin degrees of freedom in accordance with the Ising model. The 3D Ising Hamiltonian was parameterised using the average nearest-neighbour exchange coupling constant J_{ave} determined from the hybrid-exchange density functional calculations. Subsequently, the magnetic entropy was determined as a function of the temperature and magnetic field. Conclusively, from the analysis of individual entropy contributions, it was evident that the electronic and lattice entropy changes opposed the magnetic entropy change. Therefore, the former terms have a deleterious effect on the total entropy change. In light of the understanding gained from this study, a suppression of the M-I transition may result in an increase in ΔS. Therefore, further theoretical studies on the low-hole density region of the Ca-doped manganites, which undergo a FM-I to PM-I, may be of interest.

This work demonstrates the reliability of the description of the hybrid B3LYP functional for strongly correlated systems, such as the $La_{1-x}Ca_xMnO_3$ manganite series and also provides a basis for further much more computationally demanding investigations, aimed at determining the effect of a disordered Ca distribution on the structural and electronic properties of $La_{1-x}Ca_xMnO_3$. The formalism adopted herein to determine individual contributions to the total entropy change of a system has provided a valuable insight into the competing components for $La_{0.75}Ca_{0.25}MnO_3$. However, the assumption that the entropy change in magnetocaloric materials is due to individual contributions from the electronic, lattice and magnetic contributions may be invalid in systems, in which there is strong coupling between various degrees of freedom. The hybrid-exchange density functional calculation results clearly verify the striking interplay between the spin, charge and lattice degrees of freedom in the system. Therefore, the effects of more complex interactions, such as spin-lattice and spin-orbit interactions on the entropy change should also be considered. In conclusion, the theoretical results and methodologies highlighted in the present work may not only provide a useful step towards the prediction of potential magnetocaloric materials, but also offer valuable guidance to experimental efforts for tuning the magnetocaloric properties of materials, particularly oxides.

Appendix A

Basis Sets

The basis sets used in this work are given in the Tables below. The exponents, α_j, and the coefficients, c_j, of the Gaussian type orbitals (GTOs) below were found to be optimal for the manganite compositions studied.

A.1 Oxygen

The basis set for O atoms was denoted as a 8-411d(1) contraction, corresponding to one s, three sp and one d shells.

Shell-type	α_j	c_j	
1s		s	
	8020	0.00108	
	1338	0.00804	
	255.4	0.05324	
	69.22	0.1681	
	23.90	0.3581	
	9.264	0.3855	
	3.851	0.1468	
	1.212	0.0728	
2sp		s	p
	49.43	-0.00883	0.00958
	10.47	-0.0915	0.0696
	3.235	-0.0402	0.2065
	1.217	0.379	0.347
3sp		s	p
	0.4567	1.0	1.0
4sp		s	p
	0.1843	1.0	1.0
3d		d	
	0.6	1.0	

A.2 Manganese

The basis set for Mn atoms was denoted as an 86-411d(41) contraction, corresponding to one s, four sp and two d shells.

Shell-type	α_j	c_j	
$1s$		s	
	292601.0	0.000227	
	42265.0	0.0019	
	8947.29	0.0111	
	2330.32	0.0501	
	702.047	0.1705	
	242.907	0.3691	
	94.955	0.4035	
	39.5777	0.1437	
$2sp$		s	p
	732.14	-0.0053	0.0086
	175.551	-0.0673	0.0612
	58.5093	-0.1293	0.2135
	23.129	0.2535	0.4018
	9.7536	0.6345	0.4012
	3.4545	0.2714	0.2222
$3sp$		s	p
	38.389	0.0157	-0.0311
	15.4367	-0.2535	-0.0969
	6.1781	-0.8648	0.2563
	2.8235	0.9337	1.6552
$4sp$		s	p
	1.2086	1.0	1.0
$5sp$		s	p
	0.4986	1.0	1.0
$3d$		d	
	22.5929	0.0708	
	6.1674	0.3044	
	2.0638	0.5469	
	0.7401	0.5102	
$4d$		d	
	0.249	1.0	

A.3 Calcium

The basis set for Ca atom was denoted as an 8-65111(21) contraction, corresponding to one s, three sp and two d shells.

Shell-type	α_j	c_j	
$1s$		s	
	191300.0	0.0002204	
	26970.0	0.001925	
	5696.0	0.0109	
	1489.0	0.04995	
	448.3	0.1701	
	154.6	0.3685	
	60.37	0.4034	
	25.09	0.1452	
$2sp$		s	p
	448.6	-0.00575	0.00847
	105.7	-0.0767	0.0602
	34.69	-0.1122	0.2124
	13.50	0.2537	0.3771
	5.820	0.6880	0.4010
	1.819	0.3490	0.1980
$3sp$		s	p
	20.75	0.0020	-0.0365
	8.400	-0.1255	-0.0685
	3.597	-0.6960	0.1570
	1.408	1.029	1.482
	0.7260	0.9440	1.025
$4sp$		s	p
	0.4530	1.0	1.0
$5sp$		s	p
	0.2950	1.0	1.0
$3d$		d	
	3.191	-0.1600	
	0.8683	-0.3130	
$4d$		d	
	0.2891	-0.4060	

A.4 Lanthanum

The basis set of the valence electrons for the La atoms was denoted as a 411p(411)d(311) contraction corresponding to one *s*, three *sp* and one *d* shells. The core electrons are described by a pseudopotential designed by Dolg *et al.* and adapted for usage in CRYSTAL09 [201, 202].

Shell-type	α_j	c_j
5*s*		*s*
	6.3238774	-0.086529557
	3.7199279	0.61078587
	2.1881929	-1.0956970
	0.51247125	0.80819274
6*s*		*s*
	0.27290268	1.0
7*s*		*s*
	0.15	1.0
5*p*		*p*
	6.5427184	-0.0094583546
	3.8486579	0.11792823
	2.2639164	-0.33256926
	0.63548358	0.49511706
6*p*		*p*
	0.31351355	1.0
7*p*		*p*
	0.15	1.0
5*d*		*d*
	3.1281946	0.017184007
	1.7836083	-0.10742130
	1.0491814	0.090724362
6*d*		*d*
	0.41219354	1.0
7*d*		*d*
	0.15	1.0

Appendix B

The Fluctuation Dissipation Theorem

The derivation of the specific heat, C_V and susceptibilty, χ using the fluctuation dissipation theorem is given below. Firstly, the canonical ensemble describes a system in which the energy is not fixed and can fluctuate around the thermal average of the energy $\langle E \rangle$, which is given by,

$$\langle E \rangle = -\frac{1}{Z}\frac{\partial Z}{\partial \beta} \tag{B.1}$$

where Z is the partition function. The specific heat, C_V can be derived in the following steps:

$$\begin{aligned} C_V &= \frac{\partial \langle E \rangle}{\partial T} \\ &= -\frac{\beta}{T}\frac{\partial \langle E \rangle}{\partial \beta} \\ &= -\frac{\beta}{T}\frac{\partial^2 lnZ}{\partial \beta^2} \\ &= \frac{\beta}{T}\frac{\partial}{\partial \beta}\left(\frac{1}{Z}\frac{\partial Z}{\partial \beta}\right) \\ &= \frac{\beta}{T}\left[\frac{1}{Z}\frac{\partial^2 Z}{\partial \beta^2} - \frac{1}{Z^2}\left(\frac{\partial Z}{\partial \beta}\right)^2\right] \\ &= \frac{\beta}{T}\left[\langle E^2 \rangle - \langle E \rangle^2\right] \end{aligned} \tag{B.2}$$

Similarly, the magnetic susceptibility, χ can be written in terms of the variance in the magnetization:

$$\begin{aligned} \chi &= \frac{\partial \langle M \rangle}{\partial H} \\ &= \beta \left[\left\langle M^2 \right\rangle - \langle M \rangle^2 \right] \end{aligned} \tag{B.3}$$

Appendix C

The Exchange Coupling Constants

$LaMnO_3$

$$\Delta E = E^{AFM}_{\uparrow\uparrow\downarrow\downarrow} - E^{FM} = N \cdot Z \cdot J_{ap} \cdot \hat{S}_z^2 = 4 \cdot 2 \cdot J_{ap} \cdot (4 \times \frac{1}{2})^2$$

$$\Delta E = E^{AFM}_{\uparrow\downarrow\downarrow\uparrow} - E^{FM} = N \cdot Z \cdot J_{eq} \cdot \hat{S}_z^2 = 4 \cdot 4 \cdot J_{eq} \cdot (4 \times \frac{1}{2})^2$$

$$\Delta E = E^{AFM}_{\uparrow\downarrow\uparrow\downarrow} - E^{FM} = N \cdot Z \cdot J_{ap} \cdot \hat{S}_z^2 + N \cdot Z \cdot J_{eq} \cdot \hat{S}_z^2 = 4 \cdot 2 \cdot J_{ap} \cdot (4 \times \frac{1}{2})^2 + 4 \cdot 4 \cdot J_{eq} \cdot (4 \times \frac{1}{2})^2$$

	meV
$E_{\uparrow\uparrow\downarrow\downarrow}{}^{AFM}$ - E^{FM}	-20.5
$E_{\uparrow\downarrow\downarrow\uparrow}{}^{AFM}$ - E^{FM}	88.4
$E_{\uparrow\downarrow\uparrow\downarrow}{}^{AFM}$ - E^{FM}	70.3

$CaMnO_3$

$$\Delta E = E^{AFM}_{\uparrow\uparrow\downarrow\downarrow} - E^{FM} = N \cdot Z \cdot J_{ap} \cdot \hat{S}_z^2 = 4 \cdot 2 \cdot J_{ap} \cdot (3 \times \frac{1}{2})^2$$

$$\Delta E = E^{AFM}_{\uparrow\downarrow\downarrow\uparrow} - E^{FM} = N \cdot Z \cdot J_{eq} \cdot \hat{S}_z^2 = 4 \cdot 4 \cdot J_{eq} \cdot (3 \times \frac{1}{2})^2$$

$$\Delta E = E^{AFM}_{\uparrow\downarrow\uparrow\downarrow} - E^{FM} = N \cdot Z \cdot J_{ap} \cdot \hat{S}_z^2 + N \cdot Z \cdot J_{eq} \cdot \hat{S}_z^2 = 4 \cdot 2 \cdot J_{ap} \cdot (3 \times \frac{1}{2})^2 + 4 \cdot 4 \cdot J_{eq} \cdot (3 \times \frac{1}{2})^2$$

	meV
$E_{\uparrow\uparrow\downarrow\downarrow}{}^{AFM}$ - E^{FM}	-78.4
$E_{\uparrow\downarrow\downarrow\uparrow}{}^{AFM}$ - E^{FM}	-111.3
$E_{\uparrow\downarrow\uparrow\downarrow}{}^{AFM}$ - E^{FM}	-125.1

$La_{1-x}Ca_xMnO_3$: Delocalised hole

$$\Delta E = E^{AFM}_{\uparrow\uparrow\downarrow\downarrow} - E^{FM} = N \cdot Z \cdot J_{ap} \cdot \hat{S}_z^2 = 4 \cdot 2 \cdot J_{ap} \cdot (3.75 \times \frac{1}{2})^2$$

$$\Delta E = E^{AFM}_{\uparrow\downarrow\downarrow\uparrow} - E^{FM} = N \cdot Z \cdot J_{eq} \cdot \hat{S}_z^2 = 4 \cdot 4 \cdot J_{eq} \cdot (3.75 \times \frac{1}{2})^2$$

$$\Delta E = E^{AFM}_{\uparrow\downarrow\uparrow\downarrow} - E^{FM} = N \cdot Z \cdot J_{ap} \cdot \hat{S}_z^2 + N \cdot Z \cdot J_{eq} \cdot \hat{S}_z^2 = 4 \cdot 2 \cdot J_{ap} \cdot (3.75 \times \frac{1}{2})^2 + 4 \cdot 4 \cdot J_{eq} \cdot (3.75 \times \frac{1}{2})^2$$

	meV
$E_{\uparrow\uparrow\downarrow\downarrow}{}^{AFM}$ - E^{FM}	295.2
$E_{\uparrow\downarrow\downarrow\uparrow}{}^{AFM}$ - E^{FM}	269.0
$E_{\uparrow\downarrow\uparrow\downarrow}{}^{AFM}$ - E^{FM}	521.5

$La_{1-x}Ca_xMnO_3$: Localised hole

$$\Delta E = E^{AFM}_{\uparrow\uparrow\downarrow\downarrow} - E^{FM} = N \cdot Z \cdot J_{ap} \cdot \hat{S}_z^2 = 2 \cdot 2 \cdot J_{ap} \cdot ((4 \times \frac{1}{2} \cdot 4 \times \frac{1}{2}) + (3 \times \frac{1}{2} \cdot 4 \times \frac{1}{2}))$$

$$\Delta E = E^{AFM}_{\uparrow\downarrow\downarrow\uparrow} - E^{FM} = N \cdot Z \cdot J_{eq} \cdot \hat{S}_z^2 = 2 \cdot 4 \cdot J_{eq} \cdot ((4 \times \frac{1}{2} \cdot 4 \times \frac{1}{2}) + (4 \times \frac{1}{2} \cdot 3 \times \frac{1}{2}))$$

$$\Delta E = E^{AFM}_{\uparrow\downarrow\uparrow\downarrow} - E^{FM} = N \cdot Z \cdot (J_{ap} + 2 \cdot J_{eq}) \cdot \hat{S}_z^2 = 2 \cdot 2 (J_{ap}((4 \times \frac{1}{2} \cdot 4 \times \frac{1}{2}) + (4 \times \frac{1}{2} \cdot 4 \times \frac{1}{2}))$$

$$+(2 \cdot J_{eq}((4 \times \frac{1}{2} \cdot 4 \times \frac{1}{2}) + (4 \times \frac{1}{2} \cdot 3 \times \frac{1}{2}))))$$

	meV
$E_{\uparrow\uparrow\downarrow\downarrow}{}^{AFM}$ - E^{FM}	78.7
$E_{\uparrow\downarrow\downarrow\uparrow}{}^{AFM}$ - E^{FM}	201.4
$E_{\uparrow\downarrow\uparrow\downarrow}{}^{AFM}$ - E^{FM}	285.4

Appendix D

Electronic entropy of a 1D chain of hydrogen atoms

The Crystal keyword SMEAR allows finite temperature smearing of the Fermi surface, which modifies the occupancy of the eigenvalues (ϵ_i) used in constructing the density matrix from the step function, to the Fermi function:

$$f_i = (1 + e^{\frac{(\epsilon_i - \epsilon_F)}{k_b T}})^{-1} \tag{D.1}$$

where, ϵ_F is the Fermi energy and k_bT is input as WIDTH in Hartree. The free energy of the system may be computed as:

$$F = E(T) - k_B T S(T) \tag{D.2}$$

The electronic entropy is given as:

$$S_{electronic} = 2 \sum_{i,k}^{N_{states}} (f_i ln f_i + (1 - f_i) ln(1 - f_i)) k_{i,weight} \tag{D.3}$$

where N is the number of (occupied and unoccupied) states, f_i is the Fermi distribution function and $k_{i,weight}$ is the k_i point geometrical weight, respectively. $S_{electronic}$=0.00463 for a 1D chain of hydrogen atoms. Since the calculation is for a closed shell, the sum must be multiplied by two, to account for the contribution from the β electrons, as well as the α. The entropy given in the Crystal code is a constant and therefore, to convert the entropy to $Jmol^{-1}K^{-1}$, it must be multiplied by the real gas constant, R (given by $k_B \times N_A$).

Appendix E

Validation of Monte Carlo Code: Limiting Case

The Metropolis algorithm works by choosing an acceptance probability for a transition from one state to another. The algorithm repeatedly chooses a new state, and then accepts or rejects it at random with the chosen acceptance probability. Two limiting cases were chosen for validation: $T \rightarrow 0$ and $T \rightarrow \infty$. In such cases, the limits of the probability for a transition from one spin state to another are $p \rightarrow 0$ and $p \rightarrow 1$, respectively. The initial spin configuration for a system was chosen to be ferromagnetic, for which $S=+1$ (spin up) at each lattice site. Table. E.1 shows the results of validation for the two limiting cases.

The phase transition in the Ising model is that from an ordered state to a disordered state. It is evident from these results that the algorithm is sampling the Boltmann distribution correctly, since the initial and final average magnetization per lattice site at $T=0$ and ∞ is equal to 1 and 0 (on average), respectively. As expected, all the attempts made to flip a spin state at $T=0$ have been rejected and at $T \rightarrow \infty$, all attempts have been accepted.

The main Monte Carlo loop containing the algorithm was performed for one of two cases (selected by the user in the input file), which are described as follows:

1. **Random selection of lattice site**: A lattice site was selected at random using a random number generator.

2. **Sweep of lattice site**: A lattice site was selected in a predefined way (all sites were swept).

The effects of randomly selecting a lattice site (case 1) and sweeping all the lattice sites (case 2), on the average spin and magnetization has also been investigated. As can be seen in Table. E.1, S and M have been obtained for various lattice sizes, over a T=0-6 temperature range. The obtained values are in good agreement for both, case 1 and case 2. At T=0, the system is in an ordered state, therefore the average magnetization is equal to 1 per lattice site. As the temperature increases, the system undergoes a phase transition and the magnetization reduces to 0. It can be understood that the way in which the lattice site is selected (either case 1 or case 2) does not result in largely differing values of S and M. The computation of quantities as such as S and M by averaging over the output count reduces errors significantly, which arise due to the stochastic nature of the simulation.

NxN	$\mathbf{T_{limit}}$	$\mathbf{M_i}$	$\mathbf{M_f}$	**S**	**Accepted**	**Rejected**
10x10	0.0	1.00	1.00	100	0	All
	∞	1.00	0.00	0.00	All	0
50x50	0.00	1.00	1.00	2500	0	All
	∞	1.00	0.00	0.00	All	0
100x100	0.00	1.00	1.00	10000	0	All
	∞	1.00	0.00	0.00	All	0

Table E.1: The average magnetization per lattice site at temperatures, T=0J/k$_B$ and T=∞, for a 10x10, 50x50 and 100x100 lattice size. S corresponds to the average spin moment and is given by the sum of S over all lattice sites, divided by the output count.

These preliminary results agree with theoretical limits and therefore calculations for the macroscopic variables in question proceeded.

Appendix F

Permissions

Below are copies of documents giving permission to reproduce third party content in this thesis; for Figs. 2.2, 3.2, 3.3, 6.1, 7.1 and 7.2 respectively.

Re: IOP Publishing ? Permissions request form: Response Received
Lucy Evans [Lucy.Evans@iop.org] on behalf of Permissions [permissions@iop.org]

Sent: 06 October 2014 09:08
To: Korotana, Romi Kaur

Dear Romi Korotana,

Thank you for your request to reproduce IOP Publishing material.

Figure 10 - J. Phys. D: Appl. Phys. 45 (2012) 033001 to be reused in your thesis.

Please note that figure 10 from J. Phys. D: Appl. Phys. 45 (2012) 033001 contains copy right [81] therefore you may need to seek permission from them also.

Figure 1 - New Journal of Physics 6 (2004) 155, also contains copyright [4] .

We are happy to grant permission for the use you request on the terms set out below.

If you have any questions, please feel free to contact our Permissions team at permissions@iop.org.

I should be grateful if you would acknowledge receipt of this email.

Kind regards,

Lucy Evans

Publishing Assistant

IOP Publishing

Conditions

Non-exclusive, non-transferrable, revocable, worldwide, permission to use the material in print and electronic form will be granted **subject to the following conditions:**

· Permission will be cancelled without notice if you fail to fulfil any of the conditions of this letter.

· You will make reasonable efforts to contact the author(s) to seek consent for your intended use. Contacting one author acting expressly as authorised agent for their co-authors is acceptable.

· You will reproduce the following prominently alongside the material:

o the source of the material, including author, article title, title of journal, volume number, issue number (if relevant), page range (o first page if this is the only information available) and date of first publication. This information can be contained in a footnote or reference note; or

o a link back to the article (via DOI); and

o if practical and IN ALL CASES for works published under any of the Creative Commons licences the words "© IOP Publishing. Reproduced by permission of IOP Publishing. All rights reserved"

When referencing the NJP figure please use the words "© IOP Publishing & Deutsche Physikalische Gesellschaft. CC BY-NC-SA"

· The material will not, without the express permission of the author(s), be used in any way which, in the opinion of IOP Publishing, coulc distort or alter the author(s)' original intention(s) and meaning, be prejudicial to the honour or reputation of the author(s) and/or imply endorsement by the author(s) and/or IOP Publishing.

· Payment of £0 is received in full by IOP Publishing prior to use.

Please note: We do not usually provide signed permission forms as a separate attachment. Please print this email and provide it to your publisher as proof of permission.

RE: Figure reuse permission

Opel Matthias [Matthias.Opel@wmi.badw-muenchen.de]

Sent: 11 November 2014 14:37
To: Korotana, Romi Kaur

Dear Romi Korotana,

Thank you for your message. I grant you permission to reproduce Fig.10 of my article "Spintronic oxides grown by laser-MBE", published in J. Phys. D: Appl. Phys. 45, 033001 (2012).

With best regards,
Matthias Opel

--
Dr. Matthias Opel
Walther-Meissner-Institut
Bayerische Akademie der Wissenschaften
Walther-Meissner-Str. 8
85748 Garching, GERMANY
Phone: +49 89 289-53037, -14237
Fax: +49 89 289 14206
http://opel.userweb.mwn.de

> -----Original Message-----
> From: Korotana, Romi Kaur [mailto:romi.korotana09@imperial.ac.uk]
> Sent: Friday, November 7, 2014 1:52 PM
> To: Opel Matthias
> Cc: romikorotana@gmail.com
> Subject: Figure reuse permission
>
> Dear Dr. Matthias Opel,
>
> I would like to obtain permission for the use of the following figure in my PhD
> thesis:
>
> Figure 10 - J. Phys. D: Appl. Phys. 45 (2012) 033001
>
> IOP have already granted me permission, please see the attached document.
> However, they have stated that I must also obtain permission from at least
> one of the authors.
>
> Could you please grant me with permission at your earliest convenience.
> I look forward to hearing from you.
>
> Best regards,
>
> Romi
>

Re: Figure reuse permission

Valery Kiryukhin [vkir@physics.rutgers.edu]

Sent: 07 November 2014 16:13
To: Korotana, Romi Kaur
Cc: romikorotana@gmail.com

Dear Romi,

Thank you for your letter, you have my permission to use this figure.

Regards,
Valery

On Fri, 7 Nov 2014, Korotana, Romi Kaur wrote:

> Dear Valery Kiryukhin,
>
> I would like to obtain permission for the use of the following figure in my
> PhD thesis:
>
> Figure 1 - New Journal of Physics 6 (2004) 155
>
> IOP have already granted me permission, please see the attached
> document. However, they have stated
> that I must also obtain permission from at least one of the authors.
>
> Could you please grant me with permission at your earliest convenience.
> I look forward to hearing from you.
>
> Best regards,
>
> Romi

RE: Figure reuse permission
Sang-Wook Cheong [sangc@physics.rutgers.edu]

Sent: 09 November 2014 02:54
To: Korotana, Romi Kaur

Yes you can use them for your thesis as far as I am concerned.

Thx,

SW

-----Original Message-----
From: Korotana, Romi Kaur [mailto:romi.korotana09@imperial.ac.uk]
Sent: Monday, November 03, 2014 11:11 AM
To: sangc@physics.rutgers.edu; schiffer2625@yahoo.com; apr@bell-labs.com
Subject: FW: Figure reuse permission

Dear all,

I would like to obtain permission for the use of the following figure in my PhD thesis:

Fig. 1, Phys. Rev. Lett. 75, 4488 - Published 11 December 1995

APS have already granted me permission, please see the attached document. However, they have stated that I must also obtain permission from at least one of the authors.

If possible, could you please grant me with permission at your earliest convenience. If not, I'd be grateful to you if you could perhaps direct me towards the appropriate source.
I also contacted contacted Professor Radaelli but I have not received a response.
I look forward to hearing from you.

Best regards,

Romi

ELSEVIER LICENSE
TERMS AND CONDITIONS

Oct 03, 2014

This is a License Agreement between Romi Korotana ("You") and Elsevier ("Elsevier") provided by Copyright Clearance Center ("CCC"). The license consists of your order details, the terms and conditions provided by Elsevier, and the payment terms and conditions.

All payments must be made in full to CCC. For payment instructions, please see information listed at the bottom of this form.

Supplier	Elsevier Limited The Boulevard,Langford Lane Kidlington,Oxford,OX5 1GB,UK
Registered Company Number	1982084
Customer name	Romi Korotana
Customer address	Department of Materials London, Greater London SW7 2BP
License number	3481310686966
License date	Oct 03, 2014
Licensed content publisher	Elsevier
Licensed content publication	Journal of Magnetism and Magnetic Materials
Licensed content title	Itinerant electron metamagnetism and magnetocaloric effect in RCo2-based Laves phase compounds
Licensed content author	Niraj K. Singh,K.G. Suresh,A.K. Nigam,S.K. Malik,A.A. Coelho,S. Gama
Licensed content date	October 2007
Licensed content volume number	317
Licensed content issue number	1-2
Number of pages	12
Start Page	68
End Page	79
Type of Use	reuse in a thesis/dissertation
Portion	figures/tables/illustrations
Number of figures/tables/illustrations	1
Format	both print and electronic
Are you the author of this Elsevier article?	No
Will you be translating?	No
Title of your thesis/dissertation	A Combined Density Functional Theory and Monte Carlo Study of Manganites for Magnetic Refrigeration
Expected completion date	Oct 2014

10/3/2014 Rightslink® by Copyright Clearance Center

Copyright Clearance Center RightsLink

Home Account Info Help Live Chat

ANNUAL REVIEWS

Title: The Magnetocaloric Effect and Magnetic Refrigeration Near Room Temperature: Materials and Models

Author: V. Franco, J.S. Blázquez, B. Ingale, et al

Publication: Annual Review of Materials Research

Publisher: Annual Reviews

Date: Aug 4, 2012

Copyright © 2012, Annual Reviews

Logged in as:
Romi Korotana

LOGOUT

Permission Not Required

Material may be republished in a thesis / dissertation without obtaining additional permission from Annual Reviews, providing that the author and the original source of publication are fully acknowledged.

BACK CLOSE WINDOW

Copyright © 2014 Copyright Clearance Center, Inc. All Rights Reserved. Privacy statement.
Comments? We would like to hear from you. E-mail us at customercare@copyright.com

AMERICAN PHYSICAL SOCIETY
One Physics Ellipse, College Park, MD 20740 · http://www.aps.org

October 10, 2014

Romi Korotana
romi.korotana09@imperial.ac.uk

Ref # 28398

Thank you for your permission request dated Oct. 3, 2014. We are pleased to grant you a non-exclusive, non-transferable permission, English rights, limited to **print and electronic format**, provided you meet the criteria outlined below. Permission is for a one-time use and does not include permission for future editions, updates, databases, translations, or any other matters. Permission must be sought for each additional use. This permission does not include the right to modify APS material.

Please print the required copyright credit line on the first page that the material appears: "Reprinted (abstract/excerpt/figure) with permission from [FULL REFERENCE CITATION] as follows: authors names, journal title, volume number, page number and year of publication. Copyright (YEAR) by the American Physical Society.

The following language must appear somewhere on the website: "Readers may view, browse, and/or download material for temporary copying purposes only, provided these uses are for noncommercial personal purposes. Except as provided by law, this material may not be further reproduced, distributed, transmitted, modified, adapted, performed, displayed, published, or sold in whole or part, without prior written permission from the American Physical Society."

Provide a hyperlink from the reprinted APS material (the hyperlink may be embedded in the copyright credit line). APS's link manager technology makes it convenient and easy to provide links to individual articles in APS journals. For information, see: http://link.aps.org/.

You must also obtain permission from at least one of the authors for each separate work, if you haven't done so already. The author's name and address can be found on the first page of the published Article.

Use of the APS material must not imply any endorsement by the American Physical Society.

Permission is granted for use of the following APS material only:

- Fig. 1, Phys. Rev. Lett. 75, 4488 – Published 11 December 1995

Permission is limited to the single title specified of the publication as follows:
A thesis entitled "A Combined Density Functional Theory and Monte Carlo Study of Manganites for Magnetic Refrigeration" to be published by Spiral: Imperial College Digital Repository.

If you have any questions, please refer to the Copyright FAQ at: http://publish.aps.org/copyrightFAQ.html or send an email to assocpub@aps.org.

Sincerely,

Jamie L. Casey
Circulation and Fulfillment Assistant

RE: Figure reuse permission

Corinna Dahnke [Corinna.Dahnke@physics.ox.ac.uk] on behalf of Paolo Radaelli [p.g.radaelli@physics.ox.ac.uk]

Sent: 04 November 2014 17:19
To: Korotana, Romi Kaur
Cc: Paolo Radaelli [p.g.radaelli@physics.ox.ac.uk]

Dear Romi,

Professor Radaelli gladly gives his permission for the use of the following figure in your PhD thesis:
Fig. 1, Phys. Rev. Lett. 75, 4488 - Published 11 December 1995.
He wishes you the best of success with your thesis.

Kind regards,
Corinna

Corinna Dahnke
Administration Officer/PA to Head of Condensed Matter Physics
University of Oxford

Phone: +44 (0)1865 272225
Email: corinna.dahnke@physics.ox.ac.uk

-----Original Message-----
From: Korotana, Romi Kaur [mailto:romi.korotana09@imperial.ac.uk]
Sent: 31 October 2014 14:40
To: Paolo Radaelli
Subject: Figure reuse permission

Dear Professor P. Radaelli,

I would like to obtain permission for the use of the following figure in my PhD thesis:

Fig. 1, Phys. Rev. Lett. 75, 4488 - Published 11 December 1995

APS have already granted me permission, please see the attached document. However, they have stated that I must also obtain permission from at least one of the authors.

Could you please grant me with permission at your earliest convenience.
I look forward to hearing from you.

Best regards,

Romi

RE: Thesis figure permission

From Turcaud, Jeremy
To Cohen, Lesley; Korotana, Romi
Cc
Subject RE: Thesis figure permission

Yes of course, go ahead.
I confirm that you can use the figure.

Thanks,
Jeremy

From: Cohen, Lesley
Sent: 28 July 2014 14:45
To: Korotana, Romi
Cc: Turcaud, Jeremy
Subject: RE: Thesis figure permission

From my perspective it is fine for you to use Jeremy's experimental Seebeck coefficient vs. T in your thesis which of course you will attribute to him.
Best wishes
Lesley

-----Original Message-----
From: Korotana, Romi
Sent: 28 July 2014 14:37
To: Cohen, Lesley
Cc: Turcaud, Jeremy
Subject: Thesis figure permission

Dear Lesley and Jeremy,

I would like to use your figure for the Seebeck coefficient vs. T in my thesis, to show that a peak occurs at Tc.
Therefore, could you please kindly provide permission by email?
I will take a snapshot of your response and put it in the appendix if you are happy for me to use the figure.
I also understand that I'd have to request an embargo for my thesis since this work is unpublished.

Best wishes,

Romi

List of Figures

2.1 The orientation of the magnetic moments in a: a) ferromagnetic (FM), b) antiferromagnetic (AFM), c) ferrimagnetic and d) paramagnetic (PM) solid, in the absence of a magnetic field. The direction and length of the arrows indicate the direction and magnitude of the moments, respectively. 24

2.2 Schematic illustration of the Goodenough-Kanamori-Anderson (GKA) rules and the indirect superexchange interaction in $LaMnO_3$. The $3d_{x^2-y^2}$ orbital of Mn^{3+} is shaded in grey. The core spin S=3/2 of three t_{2g} orbitals of the Mn^{3+} is represented by the three arrows. The resulting interaction, which is dependent on the orbital occupation, could either be AFM (a) or FM (b) or (c). Taken from Ref. [29]. © IOP Publishing. Reproduced by permission of IOP Publishing. All rights reserved 26

3.1 A magnetic material is converted reversibly between different magnetic states ((1)-(4)) due to the application and removal of an external magnetic field, and changes temperature as result. 35

3.2 Total entropy versus temperature diagram for two values of the applied magnetic field, $H_1>0$. The horizontal and vertical arrows show the adiabatic temperature change (ΔT_{ad}) and the isothermal magnetic entropy change (ΔS_M), respectively. This figure is taken from ref. [41] with permission. 36

3.3 The maximum entropy change ΔS_{MAX} for $\Delta H = 5$T versus the peak temperature for different classes of magnetocaloric material. This figure has been taken from Reference [44] with permission. 38

3.4 The ABO_3 cubic perovskite structure packed with BO_6 octahedra, which are connected at the vertices. 41

3.5 The crystal-field splitting of the five-fold degenerate atomic $3d$ levels into lower energy (triply degenerate) t_{2g} and higher energy (doubly degenerate) e_g levels. The JT distortion of MnO_6 octahedron further lifts each degeneracy. (This figure is modified from Ref. [62].) 42

4.1 Two-dimensional 5x4 lattice (trial configuration). 60
4.2 Flow chart showing the main components of the 3D Ising model Monte Carlo code. The input parameters correspond to the lattice size, number of Monte Carlo steps, number of equilibration steps, the initial and final temperature, and the temperature interval. 62

5.1 Crystallographic cell of *Pnma* $LaMnO_3$ for the optimized B3LYP geometry (left), where **b** is the longest lattice vector. The tilted and rotated MnO_6 octahedra (right). Large (grey), medium (red) and small (black) spheres correspond to the La, O and Mn atoms, respectively. Reproduced from Reference [161]. 65
5.2 The A-, C-, F- and G- type collinear spin configurations considered, where the arrows indicate the ordering of Mn spin moments. Reproduced from Reference [161]. 66
5.3 The apical (a)) and equatorial optimised bond lengths (b) and c)), as a function of compressive and tensile uniaxial strain (**a**, **b** and **c**). 69
5.4 Total density of states for $LaMnO_3$ with projections on the La, Mn and O atoms; the Fermi level is at 0eV. Reproduced from Reference [161]. . 71
5.5 Isovalue surfaces of the calculated spin density for A-AFM $LaMnO_3$ where, the spin isosurface values are as follows: green is 0.005 (spin up) and blue is -0.005 (spin down) in units of $|e|/bohr^3$. Reproduced from Reference [161]. 73
5.6 Crystallographic cell of *Pnma* $CaMnO_3$ for the optimised B3LYP geometry, where **b** is the longest lattice vector (left). Large (red), medium (yellow) and small (black) spheres correspond to the O, Ca and Mn atoms, respectively. Reproduced from Reference [161]. 74
5.7 Total density of states for $CaMnO_3$ with projections on the Ca, Mn and O atoms; the Fermi level is at 0eV. Reproduced from Reference [161]. . 76
5.8 Isovalue surfaces of the calculated spin density for G-AFM $CaMnO_3$ where, the spin isosurface values are as follows: green is 0.005 (spin up) and blue is -0.005 (spin down); in units of $|e|/bohr^3$. Reproduced from Reference [161]. 77

6.1 The $La_{1-x}Ca_xMnO_3$ phase diagram, where CAF=canted antiferromagnet, CO=charge ordered insulator, FI=ferromagnetic insulator, FM=ferromagnetic metal, AF=antiferromagnet, O*=paramagnetic insulating phase with no long-range JT order, from Ref. [186] with permission. © IOP Publishing & Deutsche Physikalische Gesellschaft. CC BY-NC-SA 80

6.2 Crystallographic cell for the ordered lattice approximation to the substitutionally disordered $La_{3/4}Ca_{1/4}MnO_3$, where La-grey, O-red, Mn-black Ca-yellow and **b** is the longest lattice vector. 82

6.3 The stable states for $La_{0.75}Ca_{0.25}MnO_3$, where a) represents the localisation of the hole on a particular Mn and b) shows the delocalisation of the hole over two Mn in the unit cell. 84

6.4 Total density of states with projections on the Ca, La, Mn and O atoms; the Fermi level is at 0eV. 85

6.5 Isovalue surfaces of the calculated spin density for FM $La_{0.75}Ca_{0.25}MnO_3$ where, the spin isosurface values are as follows: green is 0.005 (spin up) and blue is -0.005 (spin down); in units of |e|/bohr^3. 87

6.6 Energy difference (ΔE) per formula unit (FU) with respect to the ground state (FM with hole localised at Ca site 2) as a function of doping site for both the localised and delocalised hole solutions in the optimized ground state geometry. In the case of the delocalised hole solution, site 1 is equivalent to 4, and 2 to 3 by symmetry. 88

6.7 Energy difference (ΔE) per formula unit (FU) with respect to the ground state (FM with hole localised at Ca site 2) as a function of the spin configurations (types: F, A, C, G) for both the localised and delocalised hole solutions at the optimised ground state geometry. 90

7.1 Lattice parameters and cell volume of orthorhombic $La_{0.75}Ca_{0.25}MnO_3$ as a function of temperature. Data obtained from high-resolution synchrotron X-ray powder diffraction data. The error bars are smaller than the symbols. Reprinted figure with permission from Ref. [81]. Copyright 1995 by the American Physical Society, see http://journals.aps.org/prl/abstract/10.1103/PhysRevLett.75.4488 . . . 95

7.2 Seebeck coefficient Q obtained by Turcaud *et al* (with permission and this work is to be published) for $La_{1-x}Ca_xMnO_3$ at x=0.2, 0.25 and 0.3. 97

7.3 The average (a) Energy and (b) Magnetization per spin as a function of temperature calculated by Monte Carlo simulation for various lattice sizes. The vertical line at T_R=2.269 corresponds to Onsager's analytical value for the transition temperature T_{C}. 101
7.4 (a) Specific heat and (b) Magnetic susceptibility per spin as a function of temperature calculated by Monte Carlo simulation for various lattice sizes. The vertical line at T_R=2.269 corresponds to Onsager's analytical value for the transition temperature T_{C}. 102
7.5 Configuration snapshots of a 50x50 square lattice at a finite temperature T (where J and k_B are equal to 1). The FM-PM magnetic phase transition is shown, where blue=spin up and red=spin down. 103
7.6 (a) energy and (b) specific heat capacity per spin calculated by the MC simulation for J_{ave} in a 10×10×10 lattice. 106
7.7 The magnetic entropy in zero field and the change in magnetic entropy -ΔS_{mag} due to an applied field ΔH of 2T and 4T, as a function of temperature calculated for J_{ave} in a 10×10×10 lattice. 107

List of Tables

3.1 The Curie temperature T_C and magnetocaloric potential ΔS_{iso} for compositions of the $La_{1-x}Ca_xMnO_3$ manganite series [19]. 44

5.1 Experimental lattice parameters for $LaMnO_3$ (Dyakonov *et al.* and Hauback *et al.* geometries). The calculated energy difference with respect to the ground state for each geometry, ΔE is reported in meV per formula unit. 65

5.2 Optimized and experimental lattice parameters for $LaMnO_3$ for various magnetic structures (MS). In the fourth column, the arrows refer to the spin configuration (SC) of the four Mn atoms shown in Fig 5.1a). The percentage difference between the ground state magnetic structure and the corresponding low temperature experimental one (AFM (A) for $LaMnO_3$) is given in italics. The energy difference with respect to the ground state, ΔE is also reported in meV per formula unit. 67

5.3 Optimized and experimental Mn-O bond lengths for the $LaMnO_3$, where N is the number of neighbours. The experimental bond lengths have been calculated based on unit cell dimensions and atomic coordinates determined from powder neutron diffraction studies at 9K [163,171]. The lattice vectors corresponding to the low temperature structure considered here are given in Table 5.2. 68

5.4 The net atomic charges $q=Z(n_\alpha+n_\beta)$ in units of electrons and spin moments $\mu=(n_\alpha+n_\beta)$ in units of μ_B/FU obtained from the Mulliken population analysis for the optimised $LaMnO_3$ structure. 70

5.5 Optimized and experimental lattice parameters for $CaMnO_3$ for various magnetic structures (MS). In the fourth column, the arrows refer to the spin configuration (SC) of the four Mn atoms shown in Fig 5.6a). The percentage difference between the ground state magnetic structure and the corresponding low temperature experimental one (AFM (G) for $CaMnO_3$) is given in italics. The energy difference with respect to the ground state, ΔE is also reported in meV per formula unit. 75

5.6 Optimized and experimental Mn-O bond lengths for $CaMnO_3$, where N is the number of neighbors. The experimental bond lengths have been calculated based on unit cell dimensions and atomic coordinates determined from powder neutron diffraction studies at 9K [163,171]. The lattice vectors corresponding to the low temperature structure considered here are given in Table 5.5. 75

6.1 Refined structural parameters from neutron powder-diffraction data for $La_{0.75}Ca_{0.25}MnO_3$ at 20K [187]. The space group symmetry is *Pnma* (No. 62) and the numbers in parenthesis are statistical errors of the last significant digit. 83

6.2 Optimized and experimental [187] lattice parameters for the $La_{0.75}Ca_{0.25}MnO_3$ delocalised (L) and localised (D) hole solutions. The relative energy of the metastable state (delocalised hole) with respect to the ground state (localised hole) is also given. The percentage difference between the calculated ground state lattice vectors and the corresponding experimental ones is given in italics. 84

6.3 Optimized Mn-O bond lengths for the $La_{0.75}Ca_{0.25}MnO_3$ unit cell in the FM-I and FM-M states. The Mn-O bond lengths corresponding to the Mn^{4+} are highlighted in bold. 86

6.4 The energetics for Ca doping sites 1-4 in $La_{0.75}Ca_{0.25}MnO_3$, relative to the ground state (Ca site (2)). The calculated Ca-Mn bond distances are also shown, where the hole is localised on a Mn ion. The band gaps for the majority ($\uparrow$) and minority ($\downarrow$) spin states are given. 89

6.5 Optimized and experimental [187] lattice parameters for the *Pnma* orthorhombic $La_{0.75}Ca_{0.25}MnO_3$ delocalised (L) and localised (D) hole solutions. The relative energy of these states is calculated with respect to the ground state given in Table 6.2. 89

6.6 Relative energies of various spin configurations per formula unit (FU) with respect to the ground state in the delocalised (D) and localised (L) hole optimised geometries. The expected total spin and calculated Mn spin moments are also shown. 91
6.7 Calculated J_{eq} and J_{ap} in meV for the delocalised and localised hole solutions. 91
6.8 Summary of the energetics determined (in meV) for competing interactions in $La_{0.75}Ca_{0.25}MnO_3$. 92

7.1 The electronic entropy contribution ΔS_{elec} to ΔS for the FM-M (LCMO at x=1/4) at 10K, 100K and 224K (T_C=224K), where S_{elec} for the FM-I is considered to be zero. 96
7.2 The vibrational specific heat and entropy for LCMO at x=1/4, in the FM-M and FM-I states for the primitive cell and supercell, for which the matrix elements are defined in the second column. The ΔS_{vib} is given in italics in units of $Jmol^{-1}K^{-1}$. 98
7.3 Calculated J_{ap}, J_{eq} and J_{ave} in meV for the FM-M (delocalised hole) $La_{0.75}Ca_{0.25}MnO_3$ from hybrid-exchange DFT calculations, where J_{ave} is an input parameter for the MC simulations. 104
7.4 The calculated electronic, lattice and magnetic entropy contributions to ΔS for $La_{0.75}Ca_{0.25}MnO_3$. 105

E.1 The average magnetization per lattice site at temperatures, T=0J/k_B and T=∞, for a 10x10, 50x50 and 100x100 lattice size. S corresponds to the average spin moment and is given by the sum of S over all lattice sites, divided by the output count. 128

Bibliography

[1] E. Warburg. *Ann. Phys.*, 13:141, 1881. 19

[2] W. F. Giauque. *J. Am. Chem. Soc.*, 49:1864, 1927. 19

[3] P. Debye. *Ann. Phys.*, 81:1154, 1926. 19

[4] W. F. Giauque and D. P. MacDougall. *Phys. Rev.*, 43:768, 1933. 19

[5] G. V. Brown. *J. Appl. Phys.*, 47:3673, 1976. 19

[6] V. K. Pecharsky and K. A. Gschneidner. *Phys. Rev. Lett*, 78:4494), 1997. 19, 38, 39

[7] K. Sandeman. Gas-free refrigeration. *Magnetics Technology International 2011*, 228:30–32, 2011. 20

[8] B. F. Yu, M. Liu, and P. W. Egolf. *Int. J. Refrig.*, 33:10291060, 2010. 20, 38

[9] A. Rowe. *Int. J. Refrig.*, 34:168–177, 2011. 20

[10] K. K. Neilsen, J. Tusek, K. Engelbrecht, S. Schopfer, and A. Schopfer. *Int. J. Refrig.*, 34:603–616, 2011. 20

[11] C. N. R. Rao and B. Raveau. *Collosal Magnetoresistance, Charge Ordering and Related Properties of Managese Oxides*. World Scientific, Singapore, 1998. 20, 79

[12] E. Dagotto, T. Hotta, and A. Moreo. *Phys. Rep.*, 344:1–153, 2001. 20, 43, 44, 79

[13] Y. Tokura. *Collosal Magnetoresistance Oxides*. Gordon and Breach, London, 1999. 20, 79

[14] G. H. Jonker and J. H. Santen. *Physica*, 16:337, 1950. 20

[15] A. J. Morelli, A. M. Mance, J. V. Mantese, and A. L. Micheli. *J. Appl. Phys*, 79:373–375, 1996. 20, 43, 44, 93

[16] M. B. Salamon and M. Jaime. *Rev. Mod. Phys.*, 73:583–628, 2001. 20, 43

[17] P. Schiffer, A. P. Ramirez, W. Bao, and S-W. Cheong. *Phys. Rev. Lett.*, 75:3336, 1995. 21

[18] Z. B. Guo, J. R. Zhang, H. Huang, W. P. Ding, and Y. W. Du. *Appl. Phys. Lett.*, 70:904, 1997. 21, 43, 44, 93, 94, 98, 105

[19] M. Phan and S. Yu. *J. Magn. Magn. Mater.*, 308:325), 2007. 21, 37, 40, 43, 44, 93, 143

[20] A. D. Becke. *Phys. Rev. B*, 38:3098, 1988. 22

[21] C. Lee, W. Yang, and R. G. Parr. *Phys. Rev. B*, 37:785–789, 1988. 22, 53

[22] A. D. Becke. *J. Chem. Phys.*, 98:5648, 1993. 22, 53

[23] R. L. Martin and F. Illas. *Phys. Rev. Lett.*, 79:1539–1542, 1997. 22, 54

[24] T. Bredow and A. R. Gerson. *Phys. Rev. B*, 61:5194–5201, 2000. 22, 54

[25] I. de P. R. Moreira and F. Illas R. L. Martin. *Phys. Rev. B*, 65:155102, 2002. 22, 54

[26] J. K. Perry, J. Tahir-Kheli, and W. A. Goddard. *Phys. Rev. B*, 63:144510, 2001. 22, 54

[27] X. Feng and N. M. Harrison. *Phys. Rev. B*, 69:035114, 2004. 22, 54

[28] S. Blundell. *Magnetism in Condensed Matter*. Oxford University Press, 2001. 25, 28

[29] M. Opel. *J. Phys. D: Appl. Phys.*, 45:033001, 2012. 26, 139

[30] J. B. Goodenough. *Phys. Rev.*, 100:564–573, 1955. 27

[31] J. B. Goodenough. *J. Phys. Chem. Solids*, 6:287–297, 1958. 27

[32] J. Kanamori. *J. Phys. Chem. Solids*, 10:8798, 1959. 27

[33] C. Zener. *Phys. Rev.*, 82:403, 1951. 27, 79

[34] C. Zener. *Phys. Rev.*, 81:440, 1951. 27, 79

[35] N. Boccara. *Symétries Brisées*. Hermann, Paris, 1976. 29

[36] V. S. Amaral, J. P. Arauújo, Yu. G. Pogorelov, J. M. B. Lopes dos Santos, P. B. Tavares, A. A. C. S. Lourenço, J. B. Sousa, and J. M. Vieira. *J. Magn. Magn. Mater.*, 226-230:837–839, 2001. 29

[37] C. P. Bean and D. S. Rodbell. *Phys. Rev.*, 126:104, 1962. 29, 45

[38] R. D. de Blois and D. S. Rodbell. *Phys. Rev.*, 130:1347, 1963. 29

[39] N. A. Oliveira and P. J. von Ranke. *Phys. Rep.*, 489:89, 2010. 30, 35

[40] V. K. Pecharsky and K. A. Gschneidner. *J. Appl. Phys.*, 86:565–575, 1999. 36

[41] N. K. Singh, K. G. Suresh, A. K. Nigam, S. K. Malik, A. A. Coelho, and S. Gama. *J. Magn. Magn. Mater.*, 317:68–79, 2007. 36, 37, 38, 139

[42] E. Bruck. *J.Phys. D: Appl.Phys.*, 38:R381, 2005. 37

[43] J. Romero Gómez, R. Ferreiro Garcia, A. De Miguel Catoira, and M. Romero Gómez. *Renew. Sust. Energ. Rev.*, 17:74–82, 2013. 37

[44] V. Franco, J.S. Blázquez, B. Ingale, and A. Conde. *Annu. Rev. Mater. Res.*, 42:305–342, 2012. 37, 38, 39, 46, 139

[45] E. P. Wohlfarth. *Philos. Mag.*, 7:1817–1824, 1962. 37

[46] K. G. Sandeman. *Scripta Mater.*, 67:566–571, 2012. 38

[47] K. A. Gschneidner and V. K. Pecharsky. *Annu. Rev. Mater. Sci.*, 30:387, 2000. 38

[48] B. G. Shen, J. R. Sun, F. X. Hu, H. W. Zhang, and Z. H. Cheng. *Adv. Mater.*, 21:4545–4564, 2009. 39

[49] O. Gutfleish, A. Yan, and K. Muller. *J. Appl. Phys.*, 97:10M305, 2005. 39

[50] K. Mandal, O. Gutfleish, A.Yan, A. Handstein, and K. H. Muller. *J. Magn. Mater.*, 673:290, 2005. 39

[51] M. D. Kuzmin and M. Richter. *Phys. Rev. B.*, 76:092401–1, 2007. 39

[52] A. Fujita, S. Fujieda, K. Fukamichi, H. Mitamura, and T. Goto. *Phys. Rev. B*, 65:014410, 2001. 39

[53] L. Jia, G. J. Liu, J. R. Sun, H. W. Zhang, F. X. Hu, C. Dong, G. H. Rao, and B. G. Shen. *J. App. Phys.*, 100:1239041, 2006. 39, 93, 98

[54] S. Gama, A. A. Coelho, A. de Campos, A. M. G. Carvalho, F. C. G. Gandra, P. J. von Ranke, and N. A. de Oliveira. *Phys. Rev. Lett.*, 23:237202–1–237202–4, 2004. 39

[55] H. Wada and Y. Tanabe. *Appl. Phys. Lett.)*, 79:3302), 2001. 39

[56] K. Taniguchi T. Shibata Y. Yamada H. Wada, T. Morikawa and Y. Akishige. *Physica B*, 328:114, 2003. 39

[57] M. Guillot R. Zach and R. Fruchart. *J. Magn. Magn. Mater.*, 89:221, 1990. 39

[58] N. H. Dung, Z. Q. Ou, L. Caron, L. Zhang, D. T. C. Thanh, G. A. de Wijs, R. A. de Groot, K. H. J. Buschow, and E. Brck. *Adv. Energy Mater.*, 1:1215, 2011. 40

[59] V. D. Buchelnikov. *Int. J. Appl. Electromagn. Mech.*, 23:65, 2006. 40, 46

[60] Feng-xia Hu, Bao-gen Shen, Ji-rong Sun, and Guang-heng Wu. *Phys. Rev. B*, 64:132412, 2001. 40

[61] B. Ingale, R. Gopalan, M. M. Raja, V. Chandrasekaran, and S. Ram. *J. Appl. Phys.*, 102:013906, 2007. 40

[62] Y. Tokura and Y. Tomioka. *J. Magn. Magn. Mater.*, 200:1–23, 1999. 42, 140

[63] K. Dörr. *J. Phys. D: Appl. Phys.*, 39:R125–R150, 2006. 42

[64] J. G. Bednerz and K. A. Müller. *Z. Phys. B*, 64:189, 1986. 43

[65] M. K. Wu, J. R. Ashburn, C. J. Torng, P. H. Hor, R. L. Meng, L. Gao, Z. J. Huang, Y. Q. Wang, and C. W. Chu. Superconductivity at 93 k in a new mixed-phase y-ba-cu-o compound system at ambient pressure. *Phys. Rev. Lett.*, 58:908–910, Mar 1987. 43

[66] R. von Helmolt, J. Wecker, B. Holzapfel, L. Schultz, and K. Samwer. *Phys. Rev. Lett.*, 71:2331, 1993. 43

[67] S. Jin, T. H. Tiefel, M. McCormack, R. A. Fastnacht, R. Ramesh, and L. H. Chen. *Science*, 264:413–5, 1994. 43, 79

[68] D. A. Keen R. McGreevy R. M. Kusters, J. Singleton and Y. W. Hages. *Physica B*, 362:155, 1989. 43

[69] K. A. Gschneidner, V. K. Pecharsky, and A. O. Tsokol. *Rep. Prog. Phys.*, 68:1479–1539, 2005. 43

[70] K. A. Gschneidner and V. K. Pecharsky. *Annu. Rev. Mater. Sci.*, 30:387–429, 2000. 43

[71] A. Moreo, M. Mayr, A. Feiguin, S. Yunoki, and E. Dagotto. *Phys. Rev. Lett.*, 84:5568, 2000. 43, 44

[72] L. M. Rodriguez-Martinez and J. P. Attfield. *Phys. Rev. B*, 54:622, 1996. 43, 44

[73] C. Hao, B. Zhao, Y. Huang, G. Kuang, and Y. Sun. *J. Alloys Compd.*, 509:5877–5881, 2011. 43

[74] Q. Ji, B. Lv, P. F. Wang, H. L. Cai, and X. S. Su. *J. Appl. Phys.*, 105:07D713, 2009. 43

[75] J. Amaral, P. Tavares, M .Reis, J. Araujo, and T. Mendonca. *J. Non-Cryst. Solids*, 354:53015303, 2008. 43

[76] H. Huang W. P. Ding Y. W. Du Z. B. Guo, J. R. Zhang. *Appl. Phys. Lett.*, 70:904, 1996. 43, 44, 93, 105

[77] Y. Sun, X. Xu, and Y. H. Zhang. *J. Magn. Magn. Mater.*, 219:183, 2000. 43, 44, 93

[78] L. E. Hueso F. Rivadulla J. Mira, J. Rivas and M. A. Lopez Quintela. *J. Appl. Phys.*, 91:8903, 2002. 43

[79] Q. Wei G. C. Lin and J. X. Zhang. *J. Magn. Magn. Mater.*, 300:392, 2006. 43

[80] L. E. Hueso, P. Sande, D. R. Miguens, J. Rivas, F. Rivadulla, and M. A. Lopez-Quintela. *J. Appl. Phys.*, 91:9943, 2002. 43, 93

[81] P. G. Radaelli, D. E. Cox, M. Marezio, S-W. Cheong, P. E. Schiffer, and A. P. Ramirez. *Phys. Rev. Lett.*, 75:4488–4490, 1995. 43, 94, 95, 98, 141

[82] M. H. Phan, V. T. Pham, S.C. Yu, and J. R. Rhee. *J. Magn. Magn. Mater.*, 272-276:2337, 2004. 44, 93

[83] M. H. Phan, S.C. Yu, N. H. Hur, and Y. H. Yeong. *J. Appl. Phys.*, 96:1154, 2004. 44, 93

[84] M. H. Phan, S. B. Tian, S.C. Yu, and N. H. Hur. *Physica B*, 327:211, 2003. 44, 93

[85] X. X. Zhang, J. Tejada, Y. Xin, G. F. Sun, K. W. Wong, and X. Bohigas. *Appl. Phys. Lett.*, 69:3596, 1996. 44, 93

[86] X. Bohigas, J. Tejada, M. L. Marinez-Sarrion, S. Tripp, and R. Black. *J. Magn. Magn. Mater.*, 208:85, 2000. 44, 93

[87] M. Fath, S. Freisem, A. A. Menovsky, Y. Tomioka, J. Aarts, and J. A. Mydosh. *Science*, 285:1540–1542, 1999. 44

[88] J. M. de Teresa, M. R. Ibarra, P. A Algarabel, C. Ritter, C. Marquina, J. Blasco, A. del Moral, and Z. Arnold. *Nature (London)*, 386:256, 1997. 44, 79

[89] J. W. Lynn, R. W. Erwin, J. A. Borchers, Q. Huang, and A. Santoro, 1996. 44

[90] G. Alejandro, M. Otero Leal, M. Granada, D. Laura Ccahuana, M. Tovar, E. Winkler, and M. T. Causa. *J. Phys. Condens. Matter*, 22, 2010. 44

[91] N. Mathur and P. Littlewood. *Physics Today*, 56:25–30, 2003. 44

[92] E. A. Dagotto. *Science*, 309:257, 2005. 44

[93] A. L. Lima Sharma, P. A. Sharma, S. K. McCall, S.-B. Kim, and S.-W. Cheong. *Appl. Phys. Lett.*, 95:092506, 2009. 44

[94] M. H. Phan, M. B. Morales, N. S. Bingham, and H. Srikanth. *Phys. Rev. B*, 81:094413, 2010. 44

[95] T. Z Ward, J. D. Budai, Z. Gai, J. Z. Tischier, L Yin, and J. Shen. Elastically driven anisotropic percolation in electronic phase-separated manganites. *Nature*, 5:885, Oct 2009. 44

[96] B. N. Harmon and V. N. Antonov. *J. Appl. Phys.*, 91:9815–9820, 2002. 45

[97] M. Mihalik, J. Vejpravova, J. Rusz, M. Divis, P. Svoboda, and V. Sechovsky. *Phys. Rev. B*, 70:134405, 2004. 45

[98] D. Paudyal, V. K. Pecharsky, K. A. Jr. Gschneidner, and B. N. Harmon. *Phys. Rev. B*, 73:144406, 2006. 45

[99] V. D. Buchelnikov, V. V. Sokolovskiy, H. C. Herper, H. Ebert, and M. E. Gruner. *Phys. Rev. B*, 81:094411, 2010. 45, 46

[100] R. Korotana, G. Mallia, Z. Gercsi, and N. M. Harrison. *J. Appl. Phys.*, 113:17A910, 2013. 45

[101] E. K. Delczeg-Czirjak, L. Bergqvist, O. Eriksson, Z. Gercsi, P. Nordblad, L. Szunyogh, B. Johansson, and L. Vitos. *Phys. Rev. B*, 86:045126, 2012. 45

[102] E. K. Delczeg-Czirjak, Z. Gercsi, L. Bergqvist, O. Eriksson, L. Szunyogh, P. Nordblad, B. Johansson, and L. Vitos. *Phys. Rev. B*, 85:224435, 2012. 45

[103] A. Barcza, Z. Gercsi, K. S. Knight, and K. G. Sandeman. *Phys. Rev. Lett.*, 104:247202, 2010. 45

[104] A. Barcza, Z. Gercsi, H. Michor, K. Suzuki, W. Kockelmann, K. S. Knight, and K. G. Sandeman. *Phys. Rev. B*, 87:064410, 2012. 45

[105] J. B. Staunton, M. dos Santos Dias, J. Peace, Z. Gercsi, and K. G. Sandeman. *Phys. Rev. B*, 87:060404, 2013. 45, 46

[106] E. K. Delczeg-Czirjak, L. Delczeg, M. P. J. Punkkinen, B. Johansson, O. Eriksson, and L. Vitos. *Phys. Rev. B*, 82:085103, 2010. 45

[107] Z. Gercsi, E. K. Delczeg-Czirjak, L. Vitos, A. S. Wills, A. Daoud-Aladine, and K. G. Sandeman. *Phys. Rev. B*, 88:024417, 2013. 45

[108] S. Kaprzyk R. Zach E. K. Hill B. Wiendlocha, J. Tobola and D. Fruchart. *J. Phys. D. Appl. Phys.*, 41:1, 2008. 45

[109] P. J. von Ranke E. P. Nobrega, N. A. de Oliveira and A. Troper. *J. Phy.: Condens. Matter*, 18:1275, 2006. 46

[110] F. Y. Wu. *Rev. Mod. Phys.*, 54:235, 1982. 46

[111] M. Blume, V. J. Emery, and R. B. Griffiths. *Phys. Rev. A*, 4:1071, 1971. 46

[112] E. Restrepo-Parra, C. M. Bedoya-Hincapié, J. F. Jurado, J. C. Riano-Rojas, and J. Restrepo. *J. Magn. Magn. Mater.*, 322:3514–3518, 2010. 46

[113] E. Restrepo-Parra, C. D. Salazar-Enríquez, J. Londoño-Navarro, J. F. Jurado, and J. Restrepo. *J. Magn. Magn. Mater.*, 323:1477–1483, 2010. 46

[114] V. Basso, G. Bertotti, M. LoBue, and C.P. Sasso. *J. Magn. Magn. Mater.*, 290291:654–657, 2005. 46

[115] Y. I. Spichkin and A. M. Tishin. *J. Magn. Magn. Mater.*, 290291:700–702, 2005. 46

[116] H. Oesterreicher and F. T. Parker. *J. Appl. Phys.*, 55:4334–4338, 1984. 46

[117] A. Y. Romanov and V. P. Silin. *Fiz. Met. Metalloved.*, 83:5–11, 1997. 46

[118] V. Franco, A. Conde, and L. F. Kiss. *J. Appl. Phys.*, 104:033903, 2008. 46

[119] A. Szabo and N. S. Ostlund. *Modern Quantum Chemistry: Introduction to Advanced Electronic Structure Theory*. Dover Publications, New York, 1996. 48, 49

[120] F. Jensen. *Introduction to Computational Chemistry*. Wiley, Chichester, 2002. 48, 50, 53

[121] C. J. Cramer. *Essentials of Computational Chemistry: Theories and Models*. Wiley, Chichester, 2004. 48

[122] D. Hartree. *Math. Proc.*, 24:111, 1928. 49

[123] V. Fock. *Z. Physik*, 61:126, 1930. 49

[124] F. Illas, I. de P. R. Moreira, J. M. Bofill, and M. Filatov. *Phys. Rev. B*, 70:132414, 2004. 49

[125] P. Hohenberg and W. Kohn. *Phys. Rev.*, 136:B864–B871, 1964. 50

[126] Mel Levy. Universal variational functionals of electron densities, first-order density matrices, and natural spin-orbitals and solution of the v-representability problem. *Proceedings of the National Academy of Sciences of the United States of America*, 76(12):pp. 6062–6065, 1979. 50

[127] W. Kohn and L. J. Sham. *Phys. Rev.*, 140:A1133–A1138, 1965. 52

[128] V. N. Staroverov, G. E. Scuseria, J. Tao, and J. P. Perdew. *Phys. Rev. B*, 69:075102, 2004. 52

[129] G. I. Csonka, J. P. Perdew, A. Ruzsinszky, P. H. T. Philipsen, S. Lebègue, J. Paier, O. A. Vydrov, and J. G. Ángyán. *Phys. Rev. B*, 79:155107, 2009. 52

[130] J. Harl, L. Schimka, and G. Kresse. *Phys. Rev. B*, 81:115126, 2010. 52

[131] N. M. Harrison. *An Introduction to Density Functional Theory*. IOS Press, Amsterdam, 2003. 52, 53

[132] D. R. Hamann. *Phys. Rev. B*, 55:R10157–R10160, 1997. 53

[133] K. Laasonen, F. Csajka, and M. Parrinello. *Chem. Phys. Lett.*, 194:172, 1992. 53

[134] C. Adamo, M. Ernzerhof, and G. E. Scuseria. *J. Chem. Phys.*, 112:2643–2649, 2000. 53

[135] S. Kurth, J. P. Perdew, and P. Blaha. *Int. J. Quantum Chem.*, 75:889–909, 1999. 53

[136] A. D. Becke. *In The challenge of d and f Electrons: Theory and Computation*. American Chemical Society, Washington, 1989. 53

[137] S. H. Vosko, L. Wilk, and M. Nusair. *Can. J. Phys.*, 58:1200, 1980. 53

[138] P. J. Stephens, F. J. Devlin, and C. F. Chabalowski. *J. Phys. Chem.*, 98:11623, 1994. 53

[139] J. Muscat and N. M. Harrison. *Chem. Phys. Lett.*, 342:2016–2018, 2001. 53, 54

[140] S. F. Boys. *Proc. R. Soc. (London) A*, 200:542, 1950. 55

[141] E. Ruiz, A. Rodriguez-Fortea, J. Tercero, T. Cauchy, and C. Massobrio. *J. Chem. Phys.*, 123:074102, 2005. 56

[142] F. Bloch. *Z. Physik*, 52:555, 1928. 57

[143] R. Dovesi, V. R. Saunders, C. Roetti, R. Orlando, C. M. Zicovich-Wilson, F. Pascale, B. Civalleri, K. Doll, N. M. Harrison, I. J. Bush, P. Dco, and M. Llunell. *CRYSTAL09 User's Manual*. University of Torino, Torino, 2009. 57

[144] D. Mu noz, N. M. Harrison, and F. Illas. *Phys. Rev. B*, 69:085115, 2004. 58, 63, 69

[145] H. B. Schelegel. *Adv. Chem. Phys.*, 687:249, 1987. 58

[146] H. B. Schelegel. *Geometry Optimization: 1, in: Encyclopedia of Computational Chemistry*. Wiley, New York, 1998. 58

[147] H. W. Press, S. A. Teukolsky, W. T. Vetterling, and P. B. Flannery. *Numerical Recipes*. Cambridge University Press, Cambridge, 1992. 59

[148] S. Chapman. *Fortran 95/2003 for Scientists and Engineers*. McGraw-Hill, New York, 2008. 61

[149] R. D. Shannon. *Acta Cryst. A*. 63, 85

[150] H. Chevreau, I. de P. R. Moreira, B. Silvi, and F. Illas. *J. Phys. Chem.*, 105:3570, 2001. 63

[151] W. E. Pickett and D. J. Singh. *Phys. Rev. B*, 53:1146–1159, 1996. 63

[152] H. Sawada, Y. Morikawa, K. Terakura, and N. Hamada. *Phys. Rev. B*, 56(19):12154–12160, 1997. 63

[153] E. A. Kotomin, R. A. Evarestov, and Y. A. Mastrikov. *Phys. Chem. Chem. Phys.*, 7:2346, 2005. 63, 67

[154] T. Hashimoto, S. Ishibashi, and K. Terakura. *Phys. Rev. B*, 82:045124, 2010. 63

[155] Y.-S. Su, T. A. Kaplan, S. D. Mahanti, and J. F. Harrison. *Phys. Rev. B*, 61(2):1324–1329, 2000. 63

[156] M. Nicastro and C. H. Patterson. *Phys. Rev. B*, 65:205111, 2002. 63, 67, 68

[157] S. Satpathy, Z. S. Popović, and F. R. Vukajlović. *J. Appl. Phys.*, 79:4555, 1996. 64

[158] G. Trimarchi and N. Binggeli. *Phys. Rev. B*, 71(035101), 2005. 64

[159] V. I. Anisomov, J. Zaanen, and O. K. Andersen. *Phys. Rev. B*, 44(3):943–954, 1991. 64

[160] V. I. Anisimov, I. V. Solovyev, M. A. Korotin, M. T. Czyzyk, and G. A. Sawatzky. *Phys. Rev. B*, 48(23):16929–16934, 1993. 64

[161] R. Korotana, G. Mallia, Z. Gercsi, L. Liborio, and N. M. Harrison. *Phys. Rev. B*, 89:205110, 2014. 65, 66, 71, 73, 74, 76, 77, 140

[162] V. Dyakonov, F. N. Bukhanko, V. I. Kamenev, E. E. Zubov, M. Arciszewska, W. Dobrowolski, W. Dobrowolski, R. Puźniak, A. Wiśniewski, K. Piotrowski, V. Varyukhin, H. Szymczak, A. Szytuła, R. Duraj, N. Stüsser, A. Arulraj, S. Baran, B. Penc, and T. Jaworska-Gołąb. *Phys. Rev. B*, 77:214428, 2008. 64, 65, 67, 70

[163] B. C. Hauback, H. Fjellvg, and N. Sakai. *J. Solid State Chem.*, 124:43, 1996. 64, 65, 66, 67, 68, 70, 74, 75, 143, 144

[164] J. H. Lee, K. T. Delaney, E. Bousquet, N. A. Spaldin, and K. M. Rabe. *Phys. Rev. B*, 88:174426, 2013. 65

[165] http://cds.dl.ac.uk/icsd/. 66

[166] J. A. M. van Roosmalen, E. H. P. Cordfunke, R. B. Helmholdt, and H. W. Zandbergen. *J. Solid State Chem.*, 110:100, 1994. 66, 69

[167] B. C. Tofield and W. R. Scott. *J. Solid State Chem.*, 10:183–194, 1974. 66, 69

[168] J. A. M. van Roosmalen, P. van Vlaanderen, E. H. P. Cordfunke, W. L. IJdo, and D. J. W. IJdo. *J. Solid State Chem.*, 114:516, 1995. 66, 69

[169] P. Norby, I. G. Krogh Andersen, and E. Krogh Andersen. *J. Solid State Chem.*, 119:191, 1995. 67, 70

[170] C. H. Booth, F. Bridges, G. H. Kwei, J. M. Lawrence, A. L. Cornelius, and J. J. Neumeier. *Phys. Rev. B*, 57:10440, 1998. 67

[171] K. R. Poeppelmeier, M. E. Leonowicz, J. C. Scanlon, and J. M. Longo. *J. Solid State Chem.*, 45:71, 1982. 68, 75, 143, 144

[172] T. Arima, Y. Tokura, and J. B. Torrance. *Phys. Rev. B*, 48:17006, 1993. 68

[173] J. H. Jung, K. H. Kim, D. J. Eom, T. W. Noh, E. J. Choi, Jaejun Yu, Y. S. Kwon, and Y. Chung. Determination of electronic band structures of $camno_3$ and $lamno_3$ using optical-conductivity analyses. *Phys. Rev. B*, 55:15489–15493, Jun 1997. 68, 75

[174] R. Mahendiran, A. K. Raychaudhuri, A. Chainani, D. D. Sarma, and S. B. Roy. *Appl. Phys. Lett.*, 66(2):233, 1995. 68

[175] J. M. Ricart, R. Dovesi, C. Roetti, , and V. R. Saunders. *Phys. Rev. B*, 52(4):2381–2389, 1995. 70

[176] Ibério de P. R. Moreira and Francesc Illas. Ab initio theoretical comparative study of magnetic coupling in $knif_3$sand k_2 nif_4s. *Phys. Rev. B*, 55:4129–4137, Feb 1997. 70

[177] F. Moussa, M. Hennion, J. Rodriguez-Carvajal, H. Moudden, L. Pinsard, and A. Revcolevschi. *Phys. Rev. B*, 54:15149–15155, 1996. 72

[178] E.S. Božin, A. Sartbaeva, H. Zheng, S.A. Wells, J.F. Mitchell, Th. Proffen, M. F. Thorpe, and S. J. L. Billinge. *J. Phys. Chem. Solids*, 69:2146, 2008. 75

[179] E. O. Wollan and W. C. Koehler. *Phys. Rev*, 100:545, 1955. 77, 90, 92

[180] A. J. Millis, P. B. Littlewood, and B. I. Shraiman. *Phys. Rev. Lett*, 74:5144, 1995. 79

[181] A. J. Millis, R. Mueller, and B. I. Shraiman. *Phys. Rev. B*, 58:5405–5417, 1996. 79

[182] T. A. Tyson, J. Mustre de Leon, S. D. Conradson, A. R. Bishop, J. J. Neumeier, H. roder, and J. Zang. *Phys. Rev. B*, 53:13985–13988, 1996. 79

[183] S. J. L. Billinge, R. G. DiFrancesco, H. H. Kwei, J. J. Neumeier, and J. D. Thompson. *Phys. Rev. Lett*, 77:715–718, 1996. 79

[184] C. H. Booth, F. Bridges, G. H. Kwei, J. M. Lawrence, A. L. Cornelius, and J. J. Neumeier. Direct relationship between magnetism and mno_6 distortions in $la_{1-x}ca_xmno_3$. *Phys. Rev. Lett.*, 80:853–856, Jan 1998. 79

[185] A. Lanzara, N. L. Saini, M. Brunelli, F. Natali, and A. Bianconi. *Phys. Rev. Lett*, 81:878–881, 1998. 79

[186] V. Kiryukhin. *New J. Phys.*, 6:155, 2004. 80, 141

[187] P. G. Radaelli, G. Iannone, M. Marezio, H. Y. Hwang, S-W. Cheong, J. D. Jorgensen, and D. N. Argyriou. *Phys. Rev. B*, 56:8265–8275, 1997. 81, 83, 84, 89, 144

[188] E. S. Bozin, M. Schmidt, A. J. DeConinck, G. Paglia, J. F. Mitchell, T. Chatterji, P. G. Radaielli, Th. Proffen, and S. J. L. Billinge. *Phys. Rev. Lett.*, 98:137203, 2007. 85

[189] M. Opel. *Phys. Rev. B*, 75:144408, 2007. 91

[190] J. Y. T. Wei, N. C. Yeh, R. P. Vasquez, and A. Gupta. *J. Appl. Phys.*, 83:7366–7368, 1998. 92

[191] Q. Y. Xu, K. M. Gu, X. L. Liang, G. Ni, Z. M. Wang, H. Sang, and Y. W. Du. *J. Appl. Phys.*, 90:524, 2001. 93

[192] K. H. Kim, J. Y. Gu, H. S. Choi, G. W. Park, and T. W. Noh. *Phys. Rev. Lett.*, 77:1877, 1996. 94

[193] A. M. Tishin and I. Spichkin. *The Magnetocaloric Effect and its Applications*. Institute of Physics Publishing, Bristol, 2003. 94

[194] N. D. Mermin. *Phys. Rev.*, 137:1441, 1965. 95

[195] D. Emin. *Thermoelectrics handbook: macro to nano*. Taylor and Francis, Boca Raton, 2006. 96

[196] F. Pascale, C. M. Zicovich-Wilson, F. L. Gejo, B. Civalleri, R. Orlando, and R. Dovesi. *J. Comput. Chem.*, 25:888, 2004. 97

[197] C. Zhu, R. Zheng, J. Su, and J. He. *Appl. Phys. Lett.*, 74:3504, 1999. 98

[198] M. E. J. Newman and G. T. Barkema. *Monte Carlo Methods in Statistical Physics*. Clarendon Press, Oxford, 1999. 100

[199] D. P. Landau and K. Binder. *A guide to Monte Carlo Simulations in Statistical Physics*. Cambridge University Press, 2000. 100

[200] D. Chandler. *Introduction to Modern Statistical Mechanics*. Oxford University Press, Oxford, 1987. 100

[201] M. Dolg, H. Stoll, A. Savin, and H. Preuss. *Theoretica chimica acta*, 75:173–194, 1989. 117

[202] J. Yang and M. Dolg. *Theoretical Chemistry Accounts*, 113:212–224, 2005. 117